Interplay of queer symmetries and topology in laser written waveguide lattices

KUMULATIVE DISSERTATION

zur Erlangung des akademischen Grades
doctor rerum naturalium (Dr. rer. nat.)

vorgelegt dem Rat der Mathematisch-Naturwissenschaftlichen Fakultät
der Universität Rostock

von Mark Kremer, M. Sc. Physik
geboren am 15.05.1992 in Mülheim an der Ruhr

https://doi.org/10.18453/rosdok_id00003002

Dieses Werk ist lizenziert unter einer
Creative Commons Namensnennung - Nicht kommerziell - Keine Bearbeitungen 4.0 International Lizenz.

1. Gutachter: Prof. Dr. Alexander Szameit, Universität Rostock, Institut für Physik
2. Gutachter: Prof. Dr. Robert R. Thomson, Heriot-Watt University, Institute of Photonics and Quantum Sciences
3. Gutachter: Prof. Dr. Iacopo Carusotto, INO-CNR BEC Center and Università di Trento, Dipartimento di Fisica
Einreichung: Oktober 2020
Tag der Disputation: 22.02.2021

Zusammenfassung

In dieser Arbeit wird das Zusammenspiel von topologischen Systemen mit Symmetrien sowohl theoretisch als auch experimentell untersucht. Die theoretischen Modelle wurden in Wellenleiterstrukturen, die mit einem Femtosekundenlaser geschriebenen wurden, experimentell realisiert und bestätigt.

Eingebettet in das Feld der nicht-Hermiteschen Physik wird zunächst das Zusammenspiel eines topologischen Phasenübergangs mit einer Symmetriebrechung näher betrachtet und beide Übergänge gemessen. Weiterhin wird untersucht und gemessen, wie Supersymmetrie-Transformationen genutzt werden können um topologische Randzustände zu erhalten, zu manipulieren oder sogar zu zerstören. Im Anschluss wird das neuartige Konzept der topologischen Quadratwurzel-Isolatoren eingeführt, in welchem quantisierte topologische Indizes auftreten, wenn der Hamiltonoperator quadriert wird. Die resultierenden topologischen Randzustände konnten experimentell nachgewiesen werden. Abschließend wird die Entstehung von nicht-abelschen geometrischen Phasen in einer dreibeinartigen Wellenleiteranordnung untersucht und vermessen, welche mithilfe des neuartigen Konzeptes der Quantenmetrik für eine adiabatische Evolution optimiert ist.

Abstract

In this thesis the interplay of topological systems with symmetries is investigated both, theoretically and experimentally. The theoretical models are experimentally implemented and confirmed by means of femtosecond laser written waveguide structures.

Embedded into the field of non-Hermitian physics, first the interplay of a topological phase transition with the symmetry breaking transition is investigated and both transitions are measured. Furthermore, it is studied and measured how supersymmetry transformations can be used to preserve, manipulate, or even destroy topological edge states. This is followed by introducing the novel concept of square root topological insulators, in which quantised topological indices emerge if the Hamiltonian is squared. The resulting topological edge states are experimentally confirmed. The thesis is concluded by investigating and measuring the emergence of non-Abelian geometric phases in a tripod waveguide structure, which is optimised for an adiabatic evolution by using the novel concept of a quantum metric.

Contents

1 Introduction 1

2 Fundamentals 3

2.1 Coupled mode equations 3
2.2 Mathematical formalism 4
2.3 Topology 5
2.4 Experimental methods 7
  2.4.1 Fabrication 7
  2.4.2 Characterisation 8
  2.4.3 Limitations 9

3 PT Symmetry in two dimensions and its influence on topology 11

3.1 PT symmetry 11
  3.1.1 General mathematical framework 11
  3.1.2 Winding numbers 12
  3.1.3 PT symmetry in optics 12
3.2 Results 12
  3.2.1 Mathematical description 13
  3.2.2 Non-Hermitian photonic graphene 13
  3.2.3 PT phase transition 13
  3.2.4 Topological phase transition 14
  3.2.5 Experimental method 16
  3.2.6 Relation to current research and outlook 16

4 Topological lattices under the influence of supersymmetric transformations 17

4.1 Supersymmetry 17
  4.1.1 General mathematical framework 17
  4.1.2 Supersymmetry in photonics 18
4.2 Results 18
  4.2.1 QR factorisation 19
  4.2.2 SUSY partners 19
  4.2.3 SUSY waveguide structures 21
  4.2.4 Relation to current research and outlook 22

5 Square root topological insulators 23

5.1 Square roots in physics 23
5.2 Non-quantised topological indices 23
5.3 Results 24
  5.3.1 Aharonov–Bohm cages 24
  5.3.2 Squaring operation 25
  5.3.3 Robustness 25
  5.3.4 Experimental realisation 26
  5.3.5 Relation to current research and outlook 27

6 Non-Abelian geometric phases 29

6.1 Non-Abelian fields 29
  6.1.1 Parallel transport 30

6.1.2 Non-Abelian geometric phases 30
6.2 Quantum metric 31
6.3 Results 31
6.3.1 Tripod structure 31
6.3.2 Non-Abelian gauge field 32
6.3.3 Experimental design 33
6.3.4 Quantum metric 33
6.3.5 Experimental results 34
6.3.6 Relation to current research and outlook 34

7 Conclusion 37

8 Publications for this thesis 39
8.1 Demonstration of a two-dimensional PT-symmetric crystal 39
8.2 Topological state engineering via supersymmetric transformations 47
8.3 A square-root topological insulator with non-quantized indices 67
8.4 Optimal design strategy for non-Abelian geometric phases 87

List of all publications 97

Bibliography 99

1 Introduction

Already in ancient times, symmetries have played a fundamental role in understanding the laws of art and music, but especially those of nature itself[1–3]. The most prominent are probably rotational and translational symmetries, which are ubiquitous in our every day lives, ranging from the pattern of kitchen tiles to the moon. The treatment of these symmetries was formalised by the advent of group theory[4], which paved the road to their embedding into the mathematical framework of physics. The highly influential work of Einstein in 1905[5], as well as that of Lorentz[6] and Poincare[7], provided an insight into how physical laws and symmetries, in this case those of the Lorentz group, mutually depend on each other.

Another insight to buttress the impact of symmetries upon physics was found in 1918 by Emmy Noether[8], who showed that every continuous symmetry results in a conservation law. It could be shown that e.g. the invariance under time translations results in the conservation of energy. While it was first applied to Maxwell's equations[9], it is nowadays a core aspect of every fundamental theory. The notion of symmetry also threads through the development of quantum mechanics[10], like the rotations and permutations, which describe the electron configurations, or the use of quantum numbers, which describe the conserved quantities based on symmetries. In the current understanding of physics, all fundamental theories are based on symmetries in the sense that they are all based on Lie algebras. For the description of the fundamental forces, a prominent role is taken by non-Abelian groups, in which individual elements do not commute[3,11].

However, besides serving as the foundation of fundamental theories, symmetries have also been most helpful to find analytical solutions to highly complicated problems, as has been the case for solutions of the Einstein field equations[12]. In this vein, symmetries have also had a fundamental impact on the topic of topological physics[13,14], which has attracted greater attention in recent years. The idea at its heart is that observables are related to topological invariants. Likely the most famous example for this observation is that the Hall conductivity is proportional to a topological invariant, as stated by the TKNN (after D. J. Thouless, M. Kohmoto, M. P. Nightingale, and M. den Nijs) formula[15]. The fact that this insight is universal to a wide range of models was underlined by the prototypical model from Haldane[16], where the topological properties emerge from the intrinsic properties of a rather simple lattice model that does not rely on external magnetic fields. One of the most intriguing features of those materials is the fact that they possess a conducting edge channel, while having an insulating bulk at the same time[13]. Furthermore, the edge states are scatter free and robust against impurities, since they are solely determined by the topological invariant[13]. These materials, dubbed as topological insulators have found numerous applications ranging from the original electronic systems[17], over photonic platforms[18–20] to even mechanical systems[21]. Since the properties of topological insulators are mainly determined by their underlying symmetries, like chiral and time reversal symmetry, a periodic table has been established that groups them according to their symmetries[22].
However, new kinds of symmetry are always being discovered which do not fit into the existing categories. A prominent example is the concept of supersymmetry, which emerged in the second half of the 20th century[23]. It extended the established symmetry relations by creating the possibility to transform bosons and fermions into each other. This finding had far-reaching theoretical consequences and might resolve long-standing problems in particle physics[23].

The aim of this thesis is to investigate the interplay of topological systems with symmetries, which are often not captured by the existing classifications or not expected in this instance. The choice of referring to those symmetries as *queer* has multiple reasons. In recent history the term was used as an insult for social groups that were considered different, compared to the majority. However, in the struggle for acceptance it was adopted and by proudly using it, its meaning was overturned into something positive. The use of this term is not intended to lower the achievements of the fight for equality in any way, but the opposite, to emphasise how enriching diversity is. This term is therefore not used as a mathematical or physical classification of the used symmetry, but an attribute to emphasise that the symmetries are not necessarily part of a common classification or not expected at this instance, but nevertheless offer intriguing new insights.

In order to validate the various theoretical findings of this thesis experimentally, femtosecond laser written waveguide arrangements in fused silica glass are used[24]. This system is chosen since it is a versatile platform to implement physical effects from the fields of topology[19], non-Hermiticity[25], and supersymmetry[26]. One major benefit is the wide range of parameters that allow for a thorough implementation and validation of different models. It furthermore offers the opportunity to focus on the core aspects of a theory, by using prototypical models.

In a first step, the theoretical foundations for the description of weakly coupled waveguide arrays are provided, since they are a core aspect of all works. Furthermore, a mathematical framework is introduced that covers essential properties needed throughout the thesis, like the calculation of the topological invariant. The more specific mathematical details, such as those concerning parity time symmetry, supersymmetric transformations, or non Abelian gauge fields, are provided at the beginning of the corresponding chapter.

In the next chapter, the interplay of the discrete parity time (PT) symmetry with a topological edge state, embedded in the framework of dissipative systems, is investigated. It is hence studied how the topological properties change, when leaving the realm of Hermitian physics. This combination allows for an intriguing coexistence of two intertwined phase transitions, which are both experimentally confirmed.

This is followed by a chapter about the impact of supersymmetric transformations upon topologically non trivial systems and how this can be used as a novel method to engineering topological edge states. In this vein, the interplay between internal symmetries and supersymmetry is investigated.

In the following chapter, the notion of square root topological insulators is introduced, which establishes a novel topological classification of non-inversion symmetric topological systems. The topological states are measured by introducing a static non-vanishing flux into a lattice.

The last topic that is discussed, deals with gauge symmetries and how non-Abelian geometric phases can be realised in an optical system. Intriguingly, an intrinsically Abelian theory is harnessed to study a non-Abelian theory. Furthermore, the experimental parameters are found by using the concept of the quantum metric, yielding a successful measurement of different Wilson loops.

2 Fundamentals

In this chapter the theoretical and experimental foundation for the forthcoming chapters is presented. In a first step, the mathematical description of weakly coupled waveguide arrays is outlined, followed by key aspects of the mathematical framework. It is concluded by an explanation of the experimental setting, which consists of fabrication and characterisation of the investigated waveguide structures.

2.1 Coupled mode equations

All findings of this dissertation are based on light evolution in laser written waveguide arrays[24], which relies on the evanescent coupling between electromagnetic waves in neighbouring structures[27–33]. The waveguide arrays consist of an isotropic, non-magnetic, charge-free, bulk material with refractive index n_0, in which N regions of higher refractive index $n_0 + \Delta n_j(\vec{r})$, depending on the position $\vec{r}$, are embedded. All $\Delta n_j(\vec{r})$ are assumed to make a small angle to the z-axis and are assumed to be clearly separated from each other. The transverse shape in the x-y-plane of the individual $\Delta n_j(\vec{r})$ can be assumed to be localised around the position (x_j, y_j). A one-dimensional illustration of a transverse refractive index distribution is displayed in Fig. 2.1. The light dynamics in those arrays is captured by Maxwell's equations. However, it can be assumed that the index change is weak ($\Delta n_j(\vec{r}) \ll n_0$). This yields, together with the slowly varying envelope approximation, the previously mentioned assumptions, and a monochromatic electric field, that the dynamics follow the paraxial Helmholtz equation[24]

$$\left(\mathrm{i}\lambda\!\!\!^{-} \frac{\partial}{\partial z} + \frac{\lambda\!\!\!^{-2}}{2n_0}\Delta_\perp + \sum_{j=1}^{N} \Delta n_j(\vec{r}) \right) \vec{\mathcal{E}}(\vec{r}) = 0, \tag{2.1}$$

with the reduced wavelength $\lambda\!\!\!^{-} = \frac{\lambda}{2\pi}$, the transverse Laplace operator $\Delta_\perp = \frac{\partial^2}{\partial x^2} + \frac{\partial^2}{\partial y^2}$, and the electric field $\vec{\mathcal{E}}(\vec{r})$. Since the birefringence of the material can be neglected[34], it is sufficient to work with a scalar approach. For the further considerations the electric field is therefore treated as a scalar $\mathcal{E}(\vec{r})$.

In addition, the approximation of weakly coupled sites is used, since the $\Delta n_j(\vec{r})$ are clearly separated. This means that the electric field $\mathcal{E}(\vec{r})$ is expressed as a linear superposition of transverse modes $F_j(x, y)$ with amplitude $a_j(z)$, and propagation constant β_j. The modes are localised at the sites j (see Fig. 2.1) and individually obey the paraxial Helmholtz equation Eq. (2.1).

$$\mathcal{E}(\vec{r}) = \sum_{j=1}^{N} a_j(z) F_j(x, y) \mathrm{e}^{\mathrm{i}\beta_j z} \tag{2.2}$$

This ansatz, together with the assumption that the modes are orthogonal, leads to the coupled mode equations[24,35].

$$\mathrm{i}\frac{\partial a_m(z)}{\partial z} + \sum_{\langle l \rangle} c_{m,l}(z) a_l(z) + \sigma_m(z) a_m(z) = 0, \tag{2.3}$$

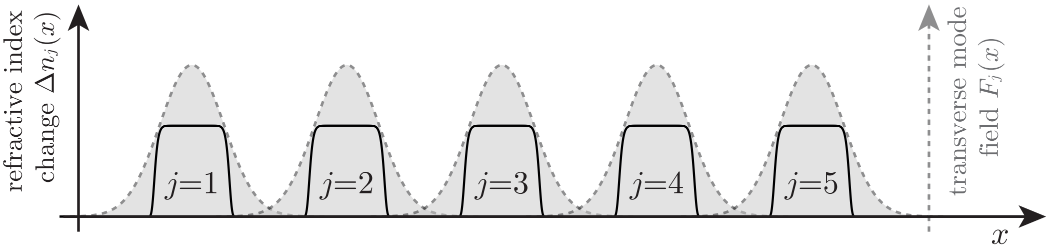

Figure 2.1 Refractive index distribution and mode profile: The one-dimensional illustration of a transverse refractive index distribution $\Delta n_j(x)$ is displayed (left axis), together with its fundamental transverse mode profiles $F_j(x)$ (right axis).

where $\langle l \rangle$ denotes the sum over the neighbouring sites in the whole x-y-plane. The couplings $c_{m,l}$ and the detunings $\sigma_m(z)$ are defined as

$$c_{m,l} = \frac{1}{\lambda\!\!\bar{}} \int_{-\infty}^{\infty} \int_{-\infty}^{\infty} \sum_{j \neq m} \Delta n_j(x,y) F_m(x,y) F_l^*(x,y) \, \mathrm{d}x \, \mathrm{d}y \tag{2.4}$$

and

$$\sigma_m = \beta_m + \frac{1}{\lambda\!\!\bar{}} \int_{-\infty}^{\infty} \int_{-\infty}^{\infty} \sum_{j \neq m} \Delta n_j(x,y) F_m(x,y) F_m^*(x,y) \, \mathrm{d}x \, \mathrm{d}y, \tag{2.5}$$

where $*$ denotes the complex conjugation. Note that if σ_m is equal for all waveguides m it can be eliminated by the transformation $a_m = \tilde{a}_m \exp(-\mathrm{i}\sigma_m z)$, therefore only differences in the detunings are contributing to the light dynamics. In all experiments the waveguides are designed to only guide the fundamental mode. This is achieved by creating a suitable refractive index distribution.

2.2 Mathematical formalism

The mathematical description of coupled waveguide arrays according to Eq. (2.3) can be summarised as

$$\mathrm{i}\frac{\partial}{\partial z}\vec{a} = H\vec{a}, \tag{2.6}$$

where all couplings $c_{m,l}$ and detunings σ_m are now contained in the matrix H. The resulting equation resembles a spatially discrete Schrödinger equation[36], where time t is replaced by the propagation distance z.[1] This means that all findings are applicable not only to waveguide arrays, but to any system that is described by such an equation. It also means in reverse that the theoretical consideration from other fields can be adapted to waveguide arrays. This refers especially to methods from quantum mechanics and solid state physics. Two aspects are especially of importance for the upcoming chapters.

---

[1] Within this formalism the coupling c is sometimes replaced by $c \mapsto -c$, which leads to the same results, since it merely induces a global phase shift. The difference between positive and negative coupling is only measurable if both appear within the same sample.

First, the real space evolution of a state from $z = z_\mathrm{i}$ to $z = z_\mathrm{f}$ is equivalent to applying[37]

$$U(z_\mathrm{f}, z_\mathrm{i}) = \hat{\mathcal{T}} \exp\left(-\mathrm{i}\int\limits_{z_\mathrm{i}}^{z_\mathrm{f}} H(z)\,\mathrm{d}z\right), \tag{2.7}$$

to an initial state $\vec{a}(z_\mathrm{i})$, where $\hat{\mathcal{T}}$ is the time-ordering operator, when treating z as t in Eq. 2.6. Note that operators O are denoted by $\hat{O}$, which is omitted for finite-dimensional matrices. It follows that

$$\vec{a}(z_f) = U(z_\mathrm{f}, z_\mathrm{i})\vec{a}(z_\mathrm{i}), \tag{2.8}$$

which is used to obtain a theoretical prediction of the performed experiments. The ordering is crucial if the couplings or detunings are changed along z, which is an essential ingredient of the work presented in chapter 6.

The second important method is the analysis of the band structure, if the waveguides are arranged in a periodic structure[33]. This can be obtained by applying a Fourier transform

$$a^j_{n,m}(z) = \int\limits_{-\pi}^{\pi}\int\limits_{-\pi}^{\pi} \mathrm{d}k_n\mathrm{d}k_m\, \tilde{a}^j(k_n, k_m, z)\mathrm{e}^{-\mathrm{i}k_n n - \mathrm{i}k_m m}, \tag{2.9}$$

where the $a^1_{n,m} \dots a^L_{n,m}$ are the elements of the unit cell, k_n and k_m are the components of the wave vector, and the labels (n, m) refer to the spatial indices of the waveguides in the x-y-plane. Note that the changed labelling compared to Eq. (2.3) is just a reordering to account for the two spatial dimensions. If the waveguide array is translational invariant along the z-direction, one can use the additional ansatz $\vec{\tilde{a}}(k_n, k_m, z) = \vec{\tilde{a}}_\nu(k_n, k_m)\mathrm{e}^{-\mathrm{i}E_\nu z}$ to obtain the band structure. The vector $\vec{\tilde{a}}(k_n, k_m, z)$ is comprised of the elements of the unit cell $\tilde{a}^1(k_n, k_m, z) \dots \tilde{a}^L(k_n, k_m, z)$. The resulting eigenvalue equation of Eq. (2.6) after the Fourier transform reads

$$H(k_n, k_m)\vec{\tilde{a}}_\nu(k_n, k_m) = E_\nu(k_n, k_m)\vec{\tilde{a}}_\nu(k_n, k_m), \tag{2.10}$$

where $\vec{\tilde{a}}_\nu(k_n, k_m)$ is the eigenstate of the band ν, with energy E_ν.

2.3 Topology

The previously mentioned band structure already characterises periodic structures in much detail, however it seemingly only allows predictions about the behaviour in an infinite lattice. This perception changed with the advent of topological physics[15,16,38,39], which allows predictions about edge properties, like localisation, from bulk properties. The key feature of this link is the so-called topological invariant, which indicates the topological features in a single invariant. In other words, physical observables are related to topological invariants. However, since this invariant needs to reflect the characteristic features of the system, there is a plethora of different invariants e.g. for Floquet modulations or non-reciprocal models[15,40–44]. For the works presented in the chapters 3–5, adaptions of one specific invariant is used. This is the so-called Zak phase[41], which characterises periodic one-dimensional systems and is defined as

$$\mathcal{Z}_\nu = \mathrm{i}\int\limits_{-\pi}^{\pi} \mathrm{d}k\, \vec{\tilde{a}}^\dagger_\nu(k)\frac{\partial}{\partial k}\vec{\tilde{a}}_\nu(k) = \mathcal{W}_\nu \pi, \tag{2.11}$$

where the $\vec{a}_\nu(k)$ are corresponding to the non-degenerate eigenstates of the ν-th band, defined by Eq. (2.10) in one dimension and where the † symbol corresponds to the joint operations of transposition and complex conjugation. Note that the periodic gauge is applied[45,46], demanding that $\vec{a}_\nu(k) = \vec{a}_\nu(k + 2\pi)$. The invariant is often normalised to π in order to reflect that it is a winding number $\mathcal{W}$. If Eq. (2.11) does not vanish one can conclude that the system possesses topological edge states, based on the bulk edge correspondence[13]. Furthermore, one can conclude that at the interface between two subsystems with different Zak phases an interface state emerges[13]. These findings and their connection to the underlying symmetries are investigated within the chapters 3–5 and the corresponding publications.

An archetypal example in one-dimensional systems is the so called Su-Schrieffer-Heeger (SSH) model[47], which is a chain of nearest neighbour coupled sites with two alternating couplings c_1 and c_2. Since this model serves as foundation for numerous findings within this work, some core aspects are discussed. The lattice is sketched in Fig. 2.2 for two possible choices of the unit cell. The Fourier transformed Hamiltonian of the infinitely extended lattice takes the form

$$H_{\mathrm{SSH}}(k) = \begin{pmatrix} 0 & c_1 + c_2 \mathrm{e}^{\mathrm{i}k} \\ c_1 + c_2 \mathrm{e}^{-\mathrm{i}k} & 0 \end{pmatrix}. \tag{2.12}$$

Evaluating the Zak phase (Eq. (2.11)) with the corresponding eigenvectors leads to[13]

$$\mathcal{Z}_\mp = \mathcal{W}_\mp \pi = \begin{cases} 0, & \text{if } c_2 < c_1 \\ \pm\pi, & \text{if } c_1 < c_2 \end{cases} \tag{2.13}$$

and is hence dependent on the ratio $\frac{c_1}{c_2}$. The index ± refers to the two bands of Eq. 2.12. In other words, the Zak phase depends on the choice of the unit cell, since the two choices are characterised by an interchanged coupling. As a consequence the lattice has edge states, depending on the termination, as displayed in Fig. 2.2.

Another method to evaluate the topology of the lattice is the Q-matrix formalism[48], which uses the fact that the topological properties in most of the cases are determined by the eigenvectors and not by the shape of the energy bands[2]. Therefore the Q-matrix is constructed from the projectors $\mathcal{P}$ and then shifted, in order to posses eigenvalues ±1

$$Q_\nu = \mathbb{1} - 2\mathcal{P}(k) = \mathbb{1} - 2\vec{a}_\nu(k)\vec{a}_\nu^\dagger(k). \tag{2.14}$$

For the chiral symmetry classes, as it is the case for the SSH model[48], this matrix can always be brought into a block off-diagonal form

$$Q_\nu = \begin{pmatrix} 0 & q_\nu \\ q_\nu^\dagger & 0 \end{pmatrix}.$$

The previously defined winding number can then be expressed with these components

$$\mathcal{W}_\nu = \frac{\mathrm{i}}{2\pi} \int_{-\pi}^{\pi} \mathrm{d}k \, q_\nu(k)^{-1} \frac{\partial}{\partial k} q_\nu(k). \tag{2.15}$$

This form is especially helpful when turning to non-Hermitian physics[44], which will be part of chapter 3.

---

[2] An exception from this rule is e.g. the skin effect, which has recently been experimentally realised with coupled fibre loops[M9].

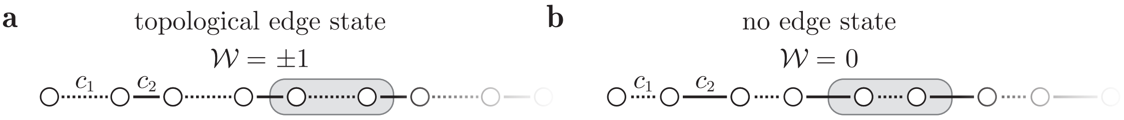

Figure 2.2 SSH chain: Illustration of the SSH chain with next neighbor couplings c_1 (dashed line) and c_2 (straight line) and two possible terminations (**a** and **b**), which correspond to a different unit cell (grey box), and to a different winding number $\mathcal{W}$. The termination in **a** leads to a topological edge state, while the configuration in **b** does not.

One important assumption to derive Eq. (2.11) is the non-degeneracy of the involved eigenstates. However, this cannot be assured for all possible one-dimensional Hamiltonians, as illustrated in chapters 5 and 6. In order to account for the degeneracy of two bands ν and μ, the expression is generalised to the Wilzcek–Zee phase[49,50]

$$\mathcal{Z}_{\nu,\mu} = \mathrm{i} \int_{-\pi}^{\pi} \mathrm{d}k \, \mathrm{tr}(\mathcal{A}(k)), \tag{2.16}$$

with $\mathcal{A}(k)$ being a matrix with components $\mathcal{A}(k)_{\nu\mu} = \vec{a}_{\nu}^{\dagger}(k) \frac{\partial}{\partial k} \vec{a}_{\mu}(k)$ and where $\mathrm{tr}(\cdot)$ denotes the trace. The two eigenstates are therefore intertwined and evaluated with an expression that is invariant against a change of basis, due to the trace.

2.4 Experimental methods

2.4.1 Fabrication

The essential feature for the derivation of the coupled mode equations in the previous section is the local increase of the refractive index. The method used for all works presented in this thesis is the femtosecond laser writing method[24] in fused silica glass (Corning 7980), with a refractive index of about $n \approx 1.457$. The two laser systems used for this process are both Titanium:Sapphire amplifiers. One is a Coherent RegA 9000 seeded with a Coherent Mira 900 and one is a Coherent RegA 9000 seeded with a Coherent Vitara S. In both cases a Coherent Verdi pump laser is used. The pulses have a center wavelength at 800 nm, a repetition rate of 100 kHz, a length of about 140 fs, and an energy in the range of 200 nJ to 450 nJ for the waveguide fabrication.

If this laser beam is focused into fused silica, the molecular structure is changed[51,52]. Fused silica is an amorphous material, where SiO_2 molecules are arranged in rings of different sizes, with the oxygen atoms as bridging elements[53]. Locally every Si atom is surrounded by four oxygen atoms in a tetrahedral arrangement, where the number of Si atoms per ring before treating it with a laser beam is around five to seven[53]. However, when focusing femtosecond laser pulses into the material, the number of rings with just three Si atoms is significantly increased[51,52]. This local change of density and hence a local change of the refractive index can be specifically tailored, since multiphoton absorption is needed for the material changes, which only occurs in the small focal region[54].

Waveguides are fabricated by moving the position of the focal point within a fused silica sample (see Fig. 2.3a). This is technically achieved by moving the sample with an Aerotech ALS130/ALS180 translation stage in all spatial directions (positioning accuracy: < 350 nm). The stage velocities are between 40 and 220 $\mathrm{mm\,min^{-1}}$. With this

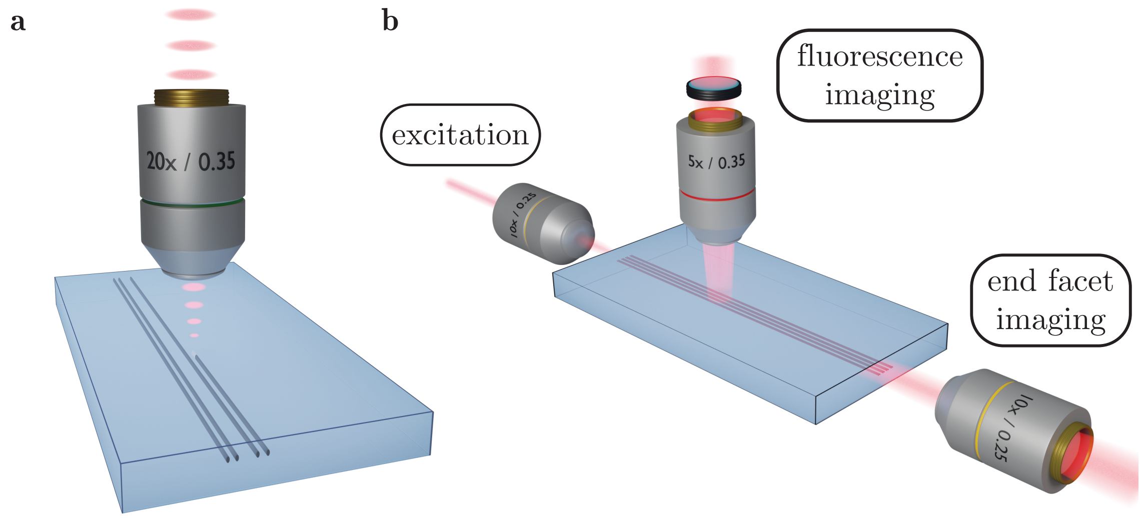

Figure 2.3 Fabrication and characterisation: a Illustration of the waveguides fabrication process by focusing femtosecond laser pulses into fused silica. By translating the sample, waveguides are inscribed into the fused silica sample. Note that the objects are not to scale. **b** The waveguide arrays are characterised by exiting a single waveguide with a laser (left) and monitoring the intensity at the end facet (right). Furthermore, the intensity distribution along the propagation can be imaged via fluorescence imaging, using a spectral edge filter (top).

method waveguides with an refractive index change of about 7×10^{-4} are fabricated[24]. The resulting waveguides are of elliptical shape, have a mode field diameter of about $8.0\,\mu\text{m} \times 10.4\,\mu\text{m}$ at 633 nm and the propagation losses and birefringence for straight waveguides are estimated to be about $0.2\,\text{dB}\,\text{cm}^{-1}$ and about 10^{-6}, respectively[24,34].

2.4.2 Characterisation

In order to characterise the fabricated structures a single waveguide of the complex structures is excited with a laser beam, using a microscope objective (10×, NA = 0.25). Depending on the invested quantities, different wavelengths are employed. Besides a Helium-Neon-Laser (Melles Griot 25 LHP 928) operating at 633 nm, a white light source (NKT SuperK EXTREME) combined with a narrow wavelength filter (Photon ETC LLTF-SR-VIS-HP8) is used. Both sources individually are applied to monitor the intensity at the end facet of the sample, by imaging the intensity distribution with an additional microscope objective (10×, NA = 0.25) upon a charged-coupled-device (CCD) camera (Basler Aviator/acA1920). In this way the intensity distribution within the waveguide structure at the end facet of the sample can be observed after having propagated through the sample (see Fig. 2.3b).

When using the the Helium-Neon-Laser, not only the intensity distribution at the end of the sample can be monitored, but also the intensity distribution at every point along the sample within the same focal plane. This is accessible by means of fluorescence microscopy[24], which is possible since non-bridging oxygen hole centres form during the fabrication process. These centres exhibit a fluorescence around 650 nm and are created insight the waveguide, leading to a high contrast[24]. By imaging the emitted fluorescence light upon a CCD camera after filtering it with a spectral edge filter, it is possible to retrieve the intensity distribution orthogonal to the excitation plane (see Fig. 2.3b). Since all waveguides need

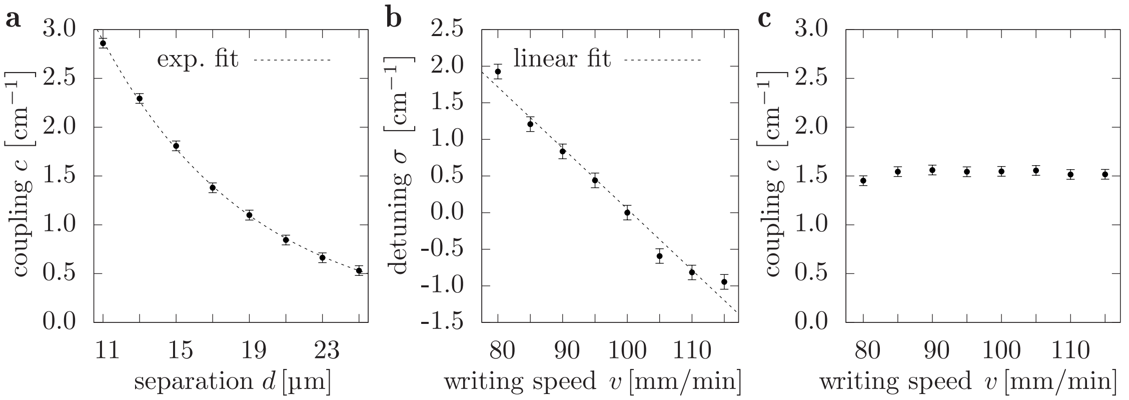

Figure 2.4 Coupling and detuning dependencies: **a** The coupling c is displayed, depending on the waveguide separation. It is exponentially decreasing with the waveguide separation, as shown by the exponential fit. **b** The dependency of the relative detuning, compared to a reference waveguide written with $v = 100\,\mathrm{mm/min}$, on the writing speed is shown. For the choosen set of parameters it can be estimated to follow a linear trend. **c** The coupling constant c, depending on the writing speed is shown. (Adapted from [M7])

to be within the same focal plane, this method is only suitable for planar structures, but not for two-dimensional arrays with numerous layers.

The two sets of quantities that characterise each array are the couplings, defined in Eq. (2.4), and the detunings, defined in Eq. (2.5). They are experimentally tuned by changing the distance and the writing speed during fabrication, respectively. Prior to fabricating a complex array, the dependencies of both quantities are determined using the fluorescence imaging outlined above, resulting in a reference curve. The dependencies are displayed in Fig. 2.4 (based on data from the publication in section 8.2). Those are retrieved from two-waveguide systems, by comparing the measured intensity distribution to the oscillation period and intensity contrast of their analytical solution. It is important to note that detuning and coupling can be chosen independently for a wide range of parameters, which is illustrated for a fixed coupling in Fig. 2.4c.

2.4.3 Limitations

In order to assure that the fabricated waveguide arrays are governed by the previously derived equations, respecting all assumptions, one needs to assure that certain requirements are fulfilled. The three main aspects are first, the supression of higher-order modes[24], second the supression of second-order coupling[55], and third the orthogonality of the neighboring modes[56]. These all significantly change the way the coupling needs to be considered in the mathematical model and are especially problematic for tightly spaced lattices, which limits the experimentally feasible coupling. In order to assure that these issues do not have a significant influence, preliminary measurements with a few waveguides are performed to find the optimal geometry and waveguide distances.

3 PT Symmetry in two dimensions and its influence on topology

In this chapter the, within this thesis, first interplay of a symmetry, in this case Parity Time (PT) symmetry, with topology is investigated. The whole analysis is embedded in the framework of dissipative systems, where PT symmetry plays an essential role to assure a real eigenvalue spectrum. After giving an introduction about the field of PT symmetry, together with a summary of the current research, a short summary of the publication at section 8.1 is provided.

3.1 PT symmetry

3.1.1 General mathematical framework

The importance of studying discrete symmetries, is distinctly demonstrated with the prediction[57] and experimental verification[58] of parity violation by the weak interaction. Furthermore, in 1998 C. M. Bender and S. Boettcher[59] found that the discrete PT symmetry has a significant impact upon non-Hermitian Hamiltonians, hence systems, where energy is no longer a preserved quantity. They showed that even non-Hermitian Hamiltonians may possess real eigenvalue spectra if they are invariant under PT symmetry. It can therefore be understood as a generalisation or extension of Hermitian quantum mechanics.

The $\hat{P}$ operator denotes spatial reflections, hence maps the spatial coordinate $\vec{r} \mapsto -\vec{r}$ and momentum $\vec{p} \mapsto -\vec{p}$, while the $\hat{T}$ operator denotes time reversal, hence maps $\vec{r} \mapsto \vec{r}$, $\vec{p} \mapsto -\vec{p}$ and the imaginary unit $\mathrm{i} \mapsto -\mathrm{i}$. If those operators are applied to a Schrödinger type equation, the necessary condition to satisfy PT symmetry is that the potential obeys the relation[60]

$$V(-\vec{r}) = V^*(\vec{r}). \tag{3.1}$$

In this case, the commutation relation $\left[\hat{H}, \hat{P}\hat{T}\right] = 0$ is fulfilled. However, this is not a sufficient condition to assure real eigenvalues. This demand holds true only in case of unbroken/exact PT symmetry, when all eigenstates of the Hamiltonian are also eigenstates of the $\hat{P}\hat{T}$ operator[60].

An important characteristic of non-Hermitian systems is that $\hat{H}$ and $\hat{H}^\dagger$ do not share the same set of eigenstates anymore.

$$\hat{H}\psi_\nu^{\mathrm{R}} = E_\nu \psi_\nu^{\mathrm{R}} \tag{3.2}$$

$$\hat{H}^\dagger \psi_\nu^{\mathrm{L}} = E_\nu^* \psi_\nu^{\mathrm{L}} \tag{3.3}$$

Moreover, they are referred to as right- and left-eigenstates ψ_ν^{R} and ψ_ν^{L} of band ν, respectively. In all further investigations it is assumed that those states form a complete biorthonormal eigenbasis. In a finite-dimensional discrete system this takes the form

$$\left(\vec{\psi}_\nu^{\mathrm{L}}\right)^\dagger \vec{\psi}_\mu^{\mathrm{R}} = \delta_{\nu,\mu} \tag{3.4}$$

$$\sum_\nu \vec{\psi}_\nu^{\mathrm{L}} \left(\vec{\psi}_\nu^{\mathrm{R}}\right)^\dagger = \sum_\nu \vec{\psi}_\nu^{\mathrm{R}} \left(\vec{\psi}_\nu^{\mathrm{L}}\right)^\dagger = \mathbb{1} \tag{3.5}$$

Based upon biorthogonal systems, the framework of PT symmetric Hamiltonians could be extended to the more general field of pseudo-Hermiticity, where the Hamiltonian and its hermitian conjugate can be connected by a general time-independent operator $\hat{O}$

$$\hat{O}\hat{H}\hat{O}^{-1} = \hat{H}^{\dagger}, \tag{3.6}$$

assuring a unitary time evolution[60,61]. It was found that every PT symmetric Hamilton with a complete biorthonormal eigenbasis, and a discrete spectrum is pseudo-hermitian[60]. If the potential fulfils Eq. (3.1), then the operator $\hat{O}$ is given by the parity operator $\hat{P}$[60].

3.1.2 Winding numbers

With the mathematical framework provided in the previous section it is possible to adapt the topological analysis of the Hermitian regime to the non-Hermitian one. The analysis will only be focused on one-dimensional and especially SSH-type Hamiltonians considered in section 2.3. To this aim, the previously defined Q-matrix of Eq. (2.14) is generalised to the framework of a biorthogonal basis, taking the form[44]

$$Q_\nu = \mathbb{1} - \mathcal{P}_1(k) - \mathcal{P}_2(k) = \mathbb{1} - \vec{\psi}_\nu^{\mathrm{L}} \left(\vec{\psi}_\nu^{\mathrm{R}}\right)^{\dagger} - \vec{\psi}_\nu^{\mathrm{R}} \left(\vec{\psi}_\nu^{\mathrm{L}}\right)^{\dagger}. \tag{3.7}$$

This can be used to define a one-dimensional winding number, which has the same form as in the Hermitian case (Eq. (2.15)), as long as Q is off-diagonal.

3.1.3 PT symmetry in optics

The main idea behind using optical platforms to study the features of PT symmetric systems is based on the finding that optical gain and loss can be used to tailor complex refractive index profiles that are mathematically the same as a complex potential in the Schrödinger equation[62–66]. The symmetry constraint of the potential, see Eq. (3.1), is therefore translated to the real and imaginary part of the refractive index distribution.

This approach is not limited to experiments with waveguide structures[25,62,65–68][M1], but is also applied to microring resonators[69,70], coupled silica microtoroids[71,72], photonic crystal slabs[73], and multiplexed mesh lattices[74,75]. With this plethora of platforms[66,76,77] it was possible to realise e.g. unidirectional invisibility[74,75], exceptional-point enhanced sensing[78], or mode selective laser cavities[69,79].

Since it is difficult to realise optical gain especially in waveguide structures, several of these applications use the principle of passive PT symmetry, which will also be used in the work presented below. In this approach a system with gain and loss is transformed into a system that has a global loss compensating for the original gain, such that only loss and *no-loss* is used[80]. These systems can nevertheless be considered (passive) PT symmetric since the additional loss is temporally and spatially constant.

3.2 Results

As described in the previous section, numerous experiments are performed to broaden the understanding of PT symmetry in general and especially in the field of optics. However, most of the approaches are limited to one spatial dimension[25,67,68][M1], are reduced to a one-dimensional effect[81], or only describe a broken PT symmetric regime[73]. The publication[M3] in section 8.1 presents how two-dimensional PT symmetric waveguide structures can be fabricated and how the topological properties are influenced by the non-Hermiticity. The main findings are summarised below.

3.2.1 Mathematical description

The non-Hermiticity used for this work is assumed to take the form of a complex onsite potential, therefore the coupled mode equations (Eq. (2.3)), derived for the lossless case, need be modified to

$$\mathrm{i}\frac{\partial a_m}{\partial z} + \sum_{\langle l\rangle} c_{m,l} a_l + \sigma_m a_m + \mathrm{i}\gamma_m a_m = 0, \tag{3.8}$$

where γ_m corresponds to the loss in waveguide m, due to scattering centres (see section 3.2.5). In case of a single waveguide the intensity is exponentially decaying, described by $a(z) = a_0 \exp(-\gamma z)$, which is used for the characterisation of the loss strength.

3.2.2 Non-Hermitian photonic graphene

The lattice structure that is investigated is a modified version of *photonic graphene* [19,82,83], which refers to the arrangement of waveguides in a honeycomb structure. The unit cell of this structure consists of two elements, which are modified differently in order to create a PT symmetric structure[84]. One element is experiencing gain, while the other one experiences loss (see Fig 3.1). The resulting coupled mode equations are

$$\mathrm{i}\frac{\partial a_{m,n}}{\partial z} - \mathrm{i}\gamma a_{m,n} + c\left(\tau b_{m-1,n} + b_{m,n+1} + b_{m,n-1}\right) = 0 \tag{3.9}$$

$$\mathrm{i}\frac{\partial b_{m,n}}{\partial z} + \mathrm{i}\gamma b_{m,n} + c\left(\tau a_{m+1,n} + a_{m,n-1} + a_{m,n+1}\right) = 0, \tag{3.10}$$

where (m, n) are the indices of the waveguides in the (x, y) plane, c is the coupling to the neighboring sites, τ is a strain applied in the x-direction of the lattice and γ is the gain/loss at the different sites. Note that $\tau = 1$ describes the case without strain. By applying a Fourier transform according to Eq. (2.9) one finds the Hamiltonian

$$H(k_m, k_n) = \begin{pmatrix} -\mathrm{i}\gamma & c\tau + 2c\,\mathrm{e}^{\mathrm{i}k_m}\cos(k_n) \\ c\tau + 2c\,\mathrm{e}^{-\mathrm{i}k_m}\cos(k_n) & \mathrm{i}\gamma \end{pmatrix} \tag{3.11}$$

with the dispersion relation[84]

$$E(k_m, k_n) = \pm\sqrt{c^2\tau^2 - \gamma^2 + 4c^2\cos^2(k_n) + 4c^2\tau\cos(k_m)\cos(k_n)}. \tag{3.12}$$

Note that the k_m was rescaled by a factor of $1/\sqrt{3}$ which resulted from the lattice structure. The characteristics of this band structure can be separated into three regimes. If $\gamma = 0$ then $E \in \mathbb{R}$, because the system is Hermitian. However, this situation changes if $\gamma \neq 0$ and no strain at all, or a weak strain of $\tau < 2 + \frac{|\gamma|}{c}$ is applied, then $E \in \mathbb{C}$ for certain k_i values. The third regime is reached if $\gamma \neq 0$ and $\tau \geq 2 + \frac{|\gamma|}{c}$, because in this case $E \in \mathbb{R}$ for any value of k_i.

3.2.3 PT phase transition

The previously discussed lattice structure (see Fig. 3.1) is clearly PT symmetric, since it is invariant under spatially inverting the lattice, while exchanging gain and loss. However, for certain parameters, the spectrum can still be complex if the Hamiltonian and the $\hat{P}\hat{T}$ operator do not share all eigenstates. It is thus experiencing broken and unbroken PT

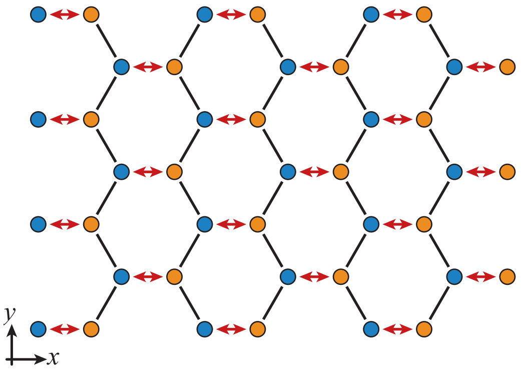

Figure 3.1 Lattice structure: Illustration of a non-Hermitian, PT symmetric honeycomb lattice. The orange lattice sites have gain $(+\gamma)$, while the blue lattice sites have loss $(-\gamma)$. The coupling along the red arrows is changed by applying a strain τ, indicated by the reduced waveguide separation.

symmetry. This transition is governed by the strain τ[84]. While the spectrum is complex for $\tau < 2 + \frac{|\gamma|}{c}$ it becomes real above this threshold. This transition can be measured by a method established in a previous work[M1]. It utilises the fact that in the broken PT symmetric phase the eigenvalue spectrum exhibits numerous different complex eigenvalues. Therefore, the power, that remains in the lattice after a certain propagation distance, is highly dependent on the injection site, since the excited eigenstates with the corresponding eigenvalues vary. The situation changes if the spectrum becomes completely real, since in that case the power is preserved on average. This transition is measured by fabricating 6 lattices with 42 sites, a coupling of $c = 0.475\,\mathrm{cm}^{-1}$, a gain/loss factor of $\gamma = 0.15\,\mathrm{cm}^{-1}$ (corresponding to a required loss factor of $\gamma = 0.30\,\mathrm{cm}^{-1}$ in the passive PT symmetric system) and strain values ranging from $1 \leq \tau \leq 2.9$. In every lattice, six different lattice sites (3 unit cells) are exited and the remaining output power after 10 cm is measured. The standard deviation of the output power is plotted in Fig 3.2a, showing a rapid decrease, when increasing the strain. The fact that the power is still oscillating is due to the fact that it is only preserved on average and not a conserved quantity anymore[63].

3.2.4 Topological phase transition

The previously discussed PT phase transition is inextricably related to a topological phase transition. The starting point to see this transition is the observation that the honeycomb lattice can be interpreted to consist of (SSH) chains perpendicular to the edges. This becomes clear if one compares Eq. (3.11) and Eq. (2.12) and treats $k_\perp = 2k_n$, which is related to the direction perpendicular to the bearded edge, as a parameter. The corresponding one-dimensional winding number (see Eq. (2.15)) predicts the edge states depending on the $k_\perp$. In case of vanishing γ this yields $|\cos(k_\perp)| > \tau/2$[85,86]. In case of a non-vanishing γ the calculation needs to be adapted to account for the non-Hermiticity of the Hamiltonian, which is achieved by using left and right eigenvectors[44] (see Eq. 3.7). Taking into account the gap closings one finds that the topological edge states exist for $0 \leq \tau < 2 - \frac{\gamma}{c}$ for $k_\perp$ that satisfy $|\cos(k_\perp)| > \tau/2$ and $(2c|\cos(k_\perp)| - c\tau)^2 > \gamma^2$. For any $\gamma \neq 0$ the edge states posses purely imaginary eingenvalues of values $\pm\gamma$, since it resides exclusively on one sublattice and is hence experiencing exclusively gain or exclusively loss. Therefore, the edge states would always break PT symmetry in a finite sample. However, the edge state of the bearded phase only exists in the broken PT symmetric phase of the bulk,

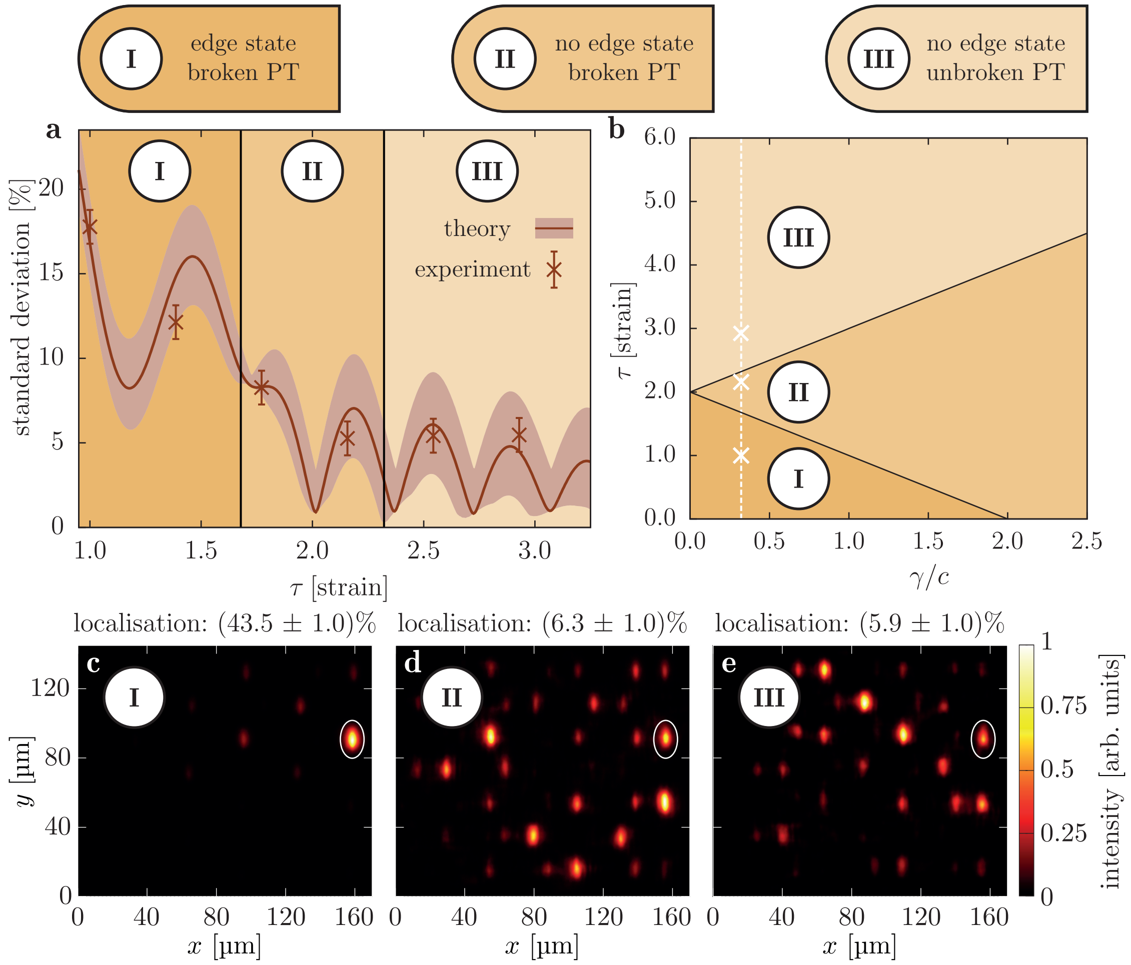

Figure 3.2 Phase transitions: **a** The standard deviation of the output power from the six inner waveguides are shown after 10 cm, depending on the strain τ. The shaded area around the theory curve takes into account deviations from unequal in-coupling. **b** The different topological and PT breaking phases are displayed, depending on the loss-to-coupling ratio γ/c. The experiments are performed for the parameteres along the white dashed line. The crosses correspond to the edge exitations shown in **c-e**, according to the labeling with the roman numerals. **c-e** Intensity distribution at the endfacet after 10 cm propagation. The initially excited waveguide is encircled. The remaining intensity within this waveguide, compared to the intensity within all waveguides is given above the panels. (Adapted from [M3])

allowing for a complete PT unbroken phase of the finite lattice. The full phase diagram is displayed in Fig. 3.2b, showing the interplay of the topological and PT symmetric phase transition. The topological phase transition is experimentally accessed, by launching single site excitation at the bearded edge of the gain sublattice (indicated by the white circle) and measuring the output distribution, as displayed in Fig. 3.2c–e. While in in Fig. 3.2c the signal stays localised (about $(43.5 \pm 1.0)\%$) within the initially excited waveguide, it spreads in in Fig. 3.2d–e, where only $(6.3 \pm 1.0)\%$ and $(5.9 \pm 1.0)\%$ remain in the waveguide. This outcome is in agreement with the prediction that the edge state vanishes for $\tau \geq 2 - \frac{\gamma}{c}$, when the bandgap is closing and remains absent when the bandgap opens again for $\tau > 2 + \frac{\gamma}{c}$ (see Fig. 3.2b).

3.2.5 Experimental method

The core ingredient to fabricate a two-dimensional passive PT symmetric structure is the implementation of a tunable and isotropic loss mechanism. For one-dimensional waveguide arrays, a method was established that provides tunable losses by applying a sinusoidal modulation of the vertical waveguide position along the propagation direction[25,67]. However, since the sinusoidal modulation is introducing a preferential directing it is not isotropic and hence only suitable for one-dimensional structures, where the modulation can always be set orthogonal to the lattice. It is not suitable for two-dimensional structures, since the second spatial dimension is needed. Therefore, a novel method is established to fulfill the demand of isotropic scattering. Instead of a sinusoidal modulation, scattering centers are introduced within the waveguide along the propagation direction. This is technically achieved by a short dwelling of the glass sample during the writing process, resulting in a local structural change of the waveguide. Using the fluorescence scanning technique, outlined in section 2.4 the resulting losses were determined, by measuring the exponential decay of the intensity of a single waveguide and comparing it with a waveguide without scattering points. The reproducibility of the obtained data could be confirmed by repeating the experiments. The two degrees of freedom of this method are the dwelling time, as well as the distance between the scattering points. However, the dwelling time should be sufficiently small to prevent damage of the sample and the distance between scattering points should be small compared to the other length scales of the structure, like the coupling. The latter limitation is important to assure that the loss mechanism can be treated as a continuous exponential decay. Two exemplary curves of these parameter dependencies are displayed in Fig 3.3, illustrating the wide range of possible loss values.

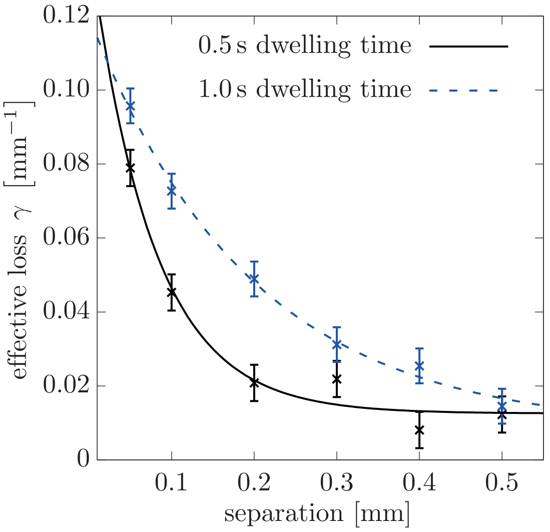

Figure 3.3 Loss mechanism: Exemplary curves for the loss dependency on the scatter point separation for two different dwelling times. The lines are exponential fits to interpolate the values. The error is estimated from the deviations when repeating the experiment. The inherent loss without scattering points is already subtracted. (Adapted from [M3])

3.2.6 Relation to current research and outlook

A two-dimensional PT symmetric lattice is meanwhile also realised in coupled fibre loops, creating an artificial mesh lattice[87]. The non-hermiticity is introduced by using erbium-doped fiber amplifiers and acousto-optic modulators. The presented experimental loss method is also applied in further works[M4]. Another approach to achieve isotropic losses, by inserting breaks into the waveguides, is used to demonstrate a Weyl exceptional ring[88], in a lattice with broken PT symmetry. While, this method also leads to the desired losses, it also introduces an additional detuning. The investigation of unidirectional, yet PT symmetric edge states remains an open question for future works.

4 Topological lattices under the influence of supersymmetric transformations

In this chapter the impact of supersymmetric transformations on topologically non-trivial systems is investigated. It is shown under which circumstances the topological properties are preserved, altered or even destroyed. After giving a short introduction into the mathematical framework of supersymmetry and its application to photonics, a short summary of the corresponding publication at section 8.2 is provided.

4.1 Supersymmetry

4.1.1 General mathematical framework

Supersymmery (SUSY) originally emerged in the context of string theory and quantum field theory. It gained much attention, since it offered a loophole to the Coleman-Mandula theorem, which constrains how space-time and internal symmetries can be combined, by introducing symmetry transformations between bosons and fermions, satisfying anticommutation relations[23]. The notion of SUSY quantum mechanics (SUSY QM) started in 1981 as a toy-model to study the core properties of SUSY[89,90], however, it also had substantial impact on solvable quantum mechanical models, since it can be related to factorisation methods[91,92]. In the following, some fundamental properties of unbroken SUSY QM are presented, which are mainly based on[90]. The starting point of SUSY QM is a one-dimensional Schrödinger equation with a potential $V_1(x)$ of which the Hamiltonian reads

$$\hat{H}_1 = -\frac{\hbar^2}{2m}\frac{\mathrm{d}^2}{\mathrm{d}x^2} + V_1(x). \tag{4.1}$$

If the wavefunction of the ground state $\phi_0(x)$ has the energy $E_0 = 0$, is nodeless, and vanishing for $x \to \pm\infty$, then the potential can be written as

$$V_1(x) = \frac{\hbar^2}{2m}\frac{\frac{\mathrm{d}^2}{\mathrm{d}x^2}\phi_0(x)}{\phi_0(x)}. \tag{4.2}$$

The Hamiltonian in Eq. (4.1) can be factorised to the form

$$\hat{H}_1 = \hat{A}^\dagger \hat{A}, \tag{4.3}$$

where

$$\hat{A} = \frac{\hbar}{\sqrt{2m}}\frac{\mathrm{d}}{\mathrm{d}x} + W(x), \qquad \hat{A}^\dagger = \frac{-\hbar}{\sqrt{2m}}\frac{\mathrm{d}}{\mathrm{d}x} + W(x), \tag{4.4}$$

with the superpotential $W(x)$. By comparing Eq. (4.3) and Eq. (4.4) with Eq. (4.1), one finds

$$V_1(x) = W^2(x) - \frac{\hbar^2}{\sqrt{2m}}\frac{\mathrm{d}}{\mathrm{d}x}W(x). \tag{4.5}$$

Combining this with Eq. (4.2), one finds upon solving the corresponding Riccati equation the explicit form

$$W(x) = -\frac{\hbar}{\sqrt{2m}} \frac{\frac{\mathrm{d}}{\mathrm{d}x}\phi_0(x)}{\phi_0(x)}. \tag{4.6}$$

Using the previous definitions it is possible to construct the SUSY partner Hamiltonian $\hat{H}_2$, with the SUSY partner potential $V_2(x)$

$$\hat{H}_2 = \hat{A}\hat{A}^\dagger = -\frac{\hbar^2}{2m}\frac{\mathrm{d}^2}{\mathrm{d}x^2} + V_2(x), \qquad V_2(x) = W^2(x) + \frac{\hbar^2}{\sqrt{2m}}\frac{\mathrm{d}}{\mathrm{d}x}W(x). \tag{4.7}$$

The two Hamiltonians are intertwined by $\hat{A}$ and $\hat{A}^\dagger$ in the form

$$\hat{H}_1\hat{A}^\dagger = A^\dagger\hat{H}_2, \qquad \hat{H}_2\hat{A} = \hat{A}\hat{H}_1. \tag{4.8}$$

This intertwining is translated to the eigenvalues $E_0^{(1)} = 0$, $E_\nu^{(2)} = E_{\nu+1}^{(1)}$ and eigenfunctions

$$\phi_\nu^{(2)} = \frac{1}{\sqrt{E_{\nu+1}^{(1)}}}\hat{A}\phi_{\nu+1}^{(1)}, \qquad \phi_{\nu+1}^{(1)} = \frac{1}{\sqrt{E_\nu^{(2)}}}\hat{A}^\dagger\phi_\nu^{(2)}, \tag{4.9}$$

where ν denotes the energy level. From those relations one can deduce that the two Hamiltonians ($\hat{H}_1$ and $\hat{H}_2$) share the same set of eigenvalues, except for the ground state energy $E_0^{(1)} = 0$ of $\hat{H}_1$, which does not exist in the spectrum of $\hat{H}_2$. The intertwining operators of Eq. (4.4) transform the eigenstates into each other, except again for the ground state of $\hat{H}_1$. In order to close the gap with the original theory, which was based upon the anticommutation relations to relate fermions and bosons, one can define the SUSY Hamiltonian $\hat{H}$, together with the operators

$$\hat{H} = \begin{pmatrix} \hat{H}_1 & 0 \\ 0 & \hat{H}_2 \end{pmatrix}, \qquad \hat{Q} = \begin{pmatrix} 0 & 0 \\ \hat{A} & 0 \end{pmatrix}, \qquad \hat{Q}^\dagger = \begin{pmatrix} 0 & \hat{A}^\dagger \\ 0 & 0 \end{pmatrix}, \tag{4.10}$$

which span the closed superalgebra, defined by the commutators and anticommutators:

$$[\hat{H}, \hat{Q}] = [\hat{H}, \hat{Q}^\dagger] = 0, \qquad \{\hat{Q}, \hat{Q}^\dagger\} = \hat{H}, \qquad \{\hat{Q}, \hat{Q}\} = \{\hat{Q}^\dagger, \hat{Q}^\dagger\} = 0. \tag{4.11}$$

4.1.2 Supersymmetry in photonics

The emergence of photonic SUSY structures is based on correspondence between the Schrödinger equation and the Helmholtz equation[93,94], which also serves as foundation for the waveguide arrays, as outlined in chapter 2. The interplay of the different degenerate modes of superpartners is used to tackle a plethora of challenges, like mode shaping[26,95–99], scattering characteristics[100–102], or the design of SUSY laser arrays[103–105]. Besides investigating and harvesting the properties of SUSY itself in photonics, also its interplay with other fields is studied, like PT symmetry[99,106,107], disorderd systems[108], or topology[109], where topological midgap states are created from trivial configurations.

4.2 Results

As pointed out above, the two SUSY Hamiltonians are closely related and intertwined, yet different in various aspects. The publication[M7] in section 8.2 presents how the properties of a topologically non-trivial Hamiltonian are translated to its SUSY partner. In particular it is shown how topological phase transitions can be systematically triggered by SUSY transformations and how this is translated to the symmetries of the system and its transformation. The main findings are summarised below.

4.2.1 QR factorisation

The factorisation of Eq. (4.3) is based on a continuous Hamiltonian. For finite systems, like waveguide arrays, this approach is adapted to discrete SUSY (DSUSY) transformations. For this purpose two possible methods are usually applied[26,94,100,103], the Cholesky algorithm[110] and the QR factorisation[110]. While the Cholesky algorithm is only valid for the removal of the fundamental mode[100], it is possible to address arbitrary states with the QR factorisation.

For this method a real matrix is decomposed into a real orthogonal matrix Q and a real upper triangular matrix R. If one starts with a Hamiltonian H, where the eigenvalue λ_ν shall be removed one finds that

$$H_{1,\nu} = H - \lambda_\nu = QR, \qquad H_{2,\nu} = RQ. \tag{4.12}$$

The Hamiltonians $H_{1,\nu}$ and $H_{2,\nu}$ share the same spectrum, however, the eigenmode of $H_{2,\nu}$ that corresponds to the eigenvalue λ_ν is completely decoupled and hence does not contribute to the propagation dynamics. In other words it is removed from the spectrum of the lattice described by $H_{2,\nu}$.

4.2.2 SUSY partners

The starting point to study the effects of SUSY transformations upon a topologically non-trivial lattice is the truncated SSH lattice, as described in section 2.3, which possesses a topological edge state at each edge. The spectrum of the finite structure hence takes the form as displayed in the right part of Fig. 4.1a, with two eigenvalues at zero energy.

This setting allows for two options, when applying a SUSY transformation; either removing the eigenvalue corresponding to a topological edge mode, or removing the eigenvalue corresponding to a bulk mode, where the bulk mode with the highest energy is chosen for consistency. The outcomes of both approaches differ strongly, with respect to the topological properties. If the eigenvalue corresponding to the bulk mode with the highest energy is removed, then the topological properties are partially destroyed. While one midgap state remains topologically non-trivial, the other one loses its topological protection. Nevertheless, both remain at zero energy. In terms of lattice parameters, this means that the non-topological state originates from a specifically tailored coupling and detuning distribution at the left edge, while the lattice at the right edge, where the topological edge state resides, possesses no detuning and only the alternating coupling structure from the SSH model. The corresponding spectrum is displayed in the right part of Fig. 4.1b. It may be noted that the removal of one lattice site necessarily needs to trigger the removal of a topological state, since it is not possible to create an SSH lattice with the same termination from an odd number of lattice sites. If the coupling would be interchanged within the lattice to enable an equal termination, one would create a topological interface state, which would also reside in the band gap, rendering this possibility invalid.

If on the other hand the eigenvalue corresponding to a topological edge mode is removed, then the topological properties are preserved and the resulting lattice possesses one topological state, which is either an edge state, or a topological interface state, due to the non-unicity of the factorisation. In terms of lattice parameters, this means that the Hamiltonian possesses no detuning and that the alternating coupling (c_1 and c_2) is either the same for the whole lattice (topological edge state) or undergoes a transition where its two values are interchanged (topological interface state). The corresponding spectrum is displayed in the right part of Fig. 4.1c.

The origin of this distinct behaviour can be explained by the underlying symmetry of the lattice, which is also the origin of the topological protection. The SSH Hamiltonian possesses a chiral symmetry

$$\hat{\Gamma} H \hat{\Gamma}^\dagger = -H, \tag{4.13}$$

where $\hat{\Gamma}$ is a unitary operator. In order to assure topological protection, the SUSY partner H_2 needs to inherit this chiral symmetry. This demand is fulfilled if $V = Q^{-1}$ possesses this symmetry since from the intertwining one can conclude that

$$V H_{1,\nu} V^{-1} = H_{2,\nu}. \tag{4.14}$$

Indeed when removing the eigenvalue corresponding to a topological edge mode (ν_topo) one finds that V possesses chiral symmetry, which, in turn, is translated to a chiral symmetry of H_{2,ν_topo}. However, the removal of an eigenvalue that corresponds to a bulk mode (ν_bulk) constitutes a more complex situation, since H_{2,ν_bulk} possesses not only a topologically trivial, but also a topologically non-trivial state. This seemingly paradoxical situation can be resolved by splitting H_{2,ν_bulk} into a left and a right part, corresponding to the left

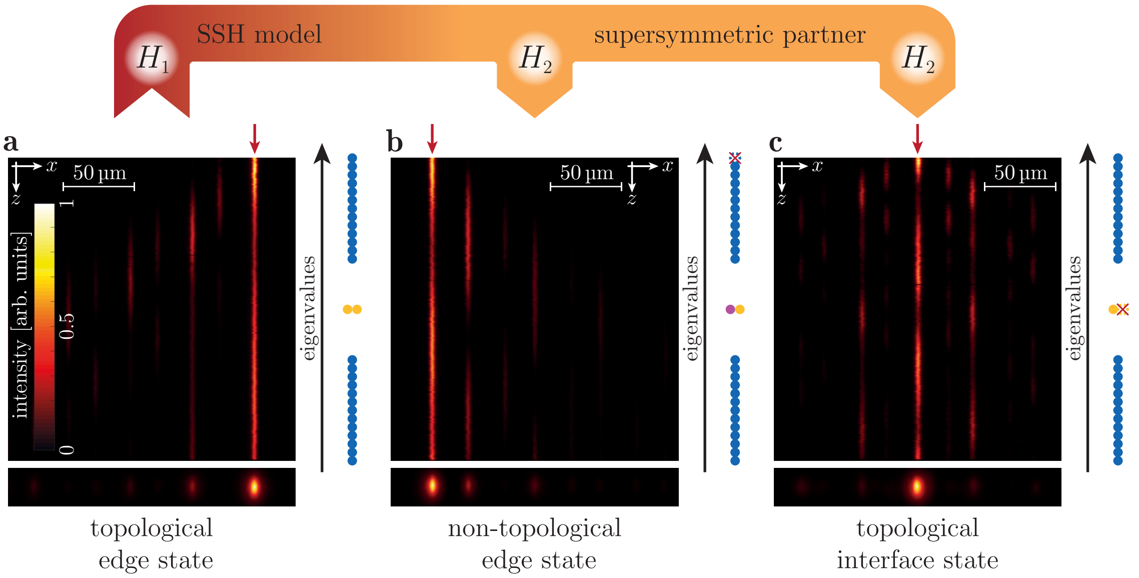

Figure 4.1 SSH model and superpartner: a The experimental measured propagation dynamics of the initial SSH model, described by H (and $H_{1,\nu}$) is displayed, when exciting the outermost waveguide, indicated by the red arrow. The sample length is 10 cm. The intensity distribution at the end facet of the sample is shown below the propagation. The corresponding eigenvalue spectrum is sketched to the right of the propagation plot, where the bulk modes are represented by blue circles and the topological edge states with yellow circles. **b** The propagation dynamics of a superpartner of the SSH model with a removed bulk mode (H_{2,ν_bulk}), is displayed. It is excited at the outermost waveguide. The eigenvalue of the non-topological edge state is represented by a violet circle, and the one of the removed mode is crossed out in the eigenvalue spectrum. **c** The propagation dynamics of a superpartner of the SSH model with a removed topological edge mode (H_{2,ν_topo}), is displayed. It is excited at the topological interface. The eigenvalue of the removed mode is crossed out in the eigenvalue spectrum. (Adapted from [M7])

and right sections of the lattice. It is found that the right part, which contains the edge where the topologically non-trivial state resides, inherits chiral symmetry, while the left part, which contains the edge where the topologically trivial state resides, has lost chiral symmetry. The symmetry at the left part is broken by the appearance of non-zero and non-uniform diagonal elements of $H_{2,\nu_{\text{bulk}}}$, which vanish, when turning to the right edge. Furthermore, if another SUSY transformation is applied that restores chiral symmetry, the topological protection of the state at the left edge can be restored. It may be noted that if the removed bulk state is energetically close to the topological states, both states lose their topological protection.

4.2.3 SUSY waveguide structures

The previously calculated and analysed lattice structures are implemented with waveguide arrays, fabricated as described in section 2.4. The two main aspects that are experimentally probed are on one hand the individual edge and interface states and its characteristics, and on the other hand the demonstration that the midgap states of $H_{2,\nu}$ share the same energy, even though one is of topological origin and the other one is not.

The SSH lattice described by H (and $H_{1,\nu}$) is fabricated in a sample with 50 waveguides having a length of 10 cm, and coupling ratios $c_1 = 0.5\,\text{cm}^{-1}$ and $c_2 = 1.0\,\text{cm}^{-1}$. The propagation obtained from the fluorescence microscopy, together with the intensity at the output facet is displayed in Fig. 4.1a, when launching the light into one of the edges. The staggered intensity profile, with intensity only in every second waveguide matches the theoretical prediction of the mode shape and is typical for an SSH-type edge mode[13].

The propagation dynamics of the SSH SUSY partner, described by $H_{2,\nu_{\text{bulk}}}$, that results when the left edge is excited is displayed in Fig. 4.1b. The exact coupling and detuning values may be found in the supplementary material of the publication presented in section 8.2. It can be seen that the intensity remains at the edge, while its distribution is not staggered and hence distinct from the topological case. The reason for this lies in the fact that this state is still a midgap state with the same energy as the former topological state, however, the mode results from a specifically tailored detuning and coupling distribution at the edge and is not topologically induced.

The propagation dynamics of the SSH SUSY partner, described by $H_{2,\nu_{\text{topo}}}$, which does not posses any edge states but instead an interface state, is displayed in Fig. 4.1c, when exciting this topological interface. The exact coupling and detuning values may be found in the supplementary material of the publication presented in section 8.2. It can be seen that the intensity remains localised at the interface and takes a staggered form, owing to its topological origin, similar to the previously discussed edge modes. Note that the couplings are calculated based on a SSH model with $c_1 = 0.5\,\text{cm}^{-1}$ and $c_2 = 1.8\,\text{cm}^{-1}$ in order to enhance the effect for better visibility. However, since the mode is of topological origin, it does not change the physical properties. The differences between the trivial mode of $H_{2,\nu_{\text{bulk}}}$ and the topological mode of H (and $H_{1,\nu}$), also manifest themselves when probing the response to different wavelengths. When the wavelength is changed, both modes remain localised at the corresponding edge, however since the topological edge mode only depends on the difference $|c_1 - c_2|$, it retains its staggered shape. In contrast, the shape of the trivial mode changes significantly with wavelength, since it relies on the exact distribution of coupling and detuning, which have different wavelength dependencies.

In a next step it is demonstrated that the two different edge states share the same energy as assumed by the previously described theoretical considerations. In order to probe this aspect, the two edge states are weakly coupled with a coupling of $c_{\text{states}} = 0.3\,\text{cm}^{-1}$. If both

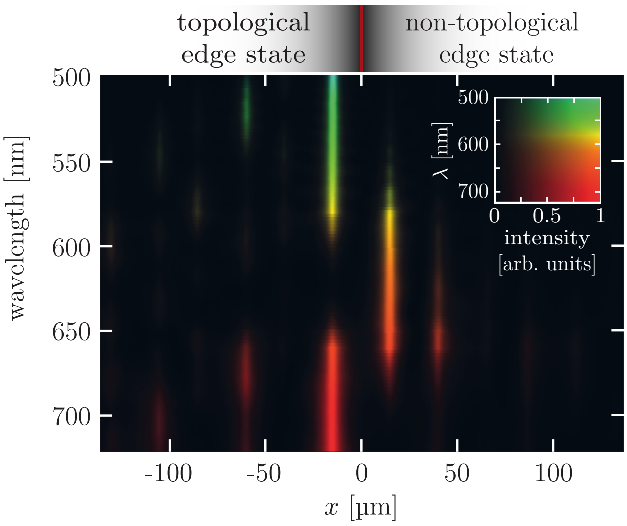

Figure 4.2 Coupling of edge modes: The intensity distribution at the end facet of two coupled waveguide arrays, for different wavelength is shown. For each measurement, i.e. each wavelength, it is integrated over the direction orthogonal to the lattice. The lattice with the topological edge state is located left of the interface, while the lattice with the non-topological edge state is located right of the interface. The sample has a length of 10 cm and is excited at the topological interface state. (Adapted from [M7])

share the same energy one would expect a full energy exchange between the states if one is initially excited. By measuring the intensity distribution using fluorescence microscopy, it was found that the light completely vanishes from the initially excited waveguide, while 70 % is transferred to he other edge state. This is in good agreement with the theoretical predictions. The full exchange of energy is also confirmed by launching different wavelengths into one of the edge states and monitoring the output intensity, as displayed in Fig. 4.2. Since a change of wavelength can effectively be understood as a rescaling of the propagation distance (see Eq. (2.1)), the energy exchange of the weakly coupled sites becomes clearly visible, confirming the equal energies as expected from SUSY partners.

4.2.4 Relation to current research and outlook

The previously discussed results provide insights about how topological properties relate to their SUSY partners. This is in contrast to previous works[109], where two SUSY partner Hamiltonians are combined to form a topological midgap state, starting from trivial configurations. However, in both approaches the way in which the two partner Hamiltonians are intertwined has significant influence on the topological properties. This can be used to specifically tailor topological properties. Next, the extension to higher dimension and further topological classes needs to be explored on a way to a generalised model of topology and SUSY.

5 Square root topological insulators

In this chapter a new kind of topological insulator is introduced, which possesses non-quantised indices, despite having robust edge states. To explain this phenomena, a procedure is introduced, where the quantised topological indices emerge from the square of the Hamiltonian, giving it the notion of a square root topological insulator. After giving a short introduction about non-trivial square roots in physics, a short summary of the corresponding publication in section 8.3 is provided.

5.1 Square roots in physics

Probably the most famous square root in physics dates back to P. A. M. Dirac, who sought a relativistic quantum theory that is invariant under Lorentz transformation[111]. By demanding that the time derivative is of first order and that the squared Hamiltonian resembles the previous findings of Klein, Gordon, and Schrödinger he found the Dirac equation, which is named after him. An essential step within this derivation was the insight that the wavefunction is not a scalar, but a vector of four complex numbers, and that, in turn, the Hamiltonian needs to be spanned by the Gamma matrices.

Subsequently, it was found that this squaring operation can be extended to numerous other fields, or is in fact intrinsically incorporated. It is e.g. connected to supersymmetric transformations[112,113], where the supersymmetric partner Hamiltonians $\hat{H}_1, \hat{H}_2$ (see Eq. (4.8)) possess the squared energy spectrum. Meanwhile, the Dirac Hamiltonian itself is linearly constructed from the operators $\hat{A}, \hat{A}^\dagger$ (see Eq. (4.4)).

It is furthermore useful for the evaluation of topological properties of mechanical systems[114], since the time derivative is of second order. By reducing the Hamiltonian to its square root it is possible to evaluate the topological properties. It may be noted that the supersymmetric considerations are especially useful for those evaluations.

In line with the previous findings, the square root procedure can also be used to alter or explore the topological features in general[109,115]. By constructing the Hamiltonian from the operators $\hat{A}, \hat{A}^\dagger$ or $\hat{Q}, \hat{Q}^\dagger$ (see Eq. (4.10)), it is possible to define a square root that intertwines two previously decoupled lattices, using the framework of SUSY[109]. Similarly this can also be approached independently from SUSY, by defining the square root operations directly on the Hamiltonian and not with the help of SUSY operators[115,116].

5.2 Non-quantised topological indices

In section 2.3 it was pointed out that a topological index ought to be quantised in order to assure topological protection.[1] In the case of the Zak phase, which is the topological invariant used for this work, this is assured if inversion symmetry is present[41]. However, even in the presence of an inversion symmetry, but with an inversion symmetry axis that is not located at the center of the unit cell, this quantisation vanishes[118]. Nevertheless, these systems may possess robust edge states. In order to properly characterise systems with a non-quantised index, the underlying mechanism needs to be identified and taken into account. If the topology is inherited from a higher dimension, it is necessary to use the invariant of this dimension, e.g. a Chern number as in the case of the Aubry-André-Harper (AAH) model[119–123]. Another proposal for coupled systems separates those into topologically non-trivial and topologically trivial subspaces[124]. A different general approach normalises the Zak phase to remove non-quantised contributions[118]. In the following section a new mechanism presents how non-quantised indices can emerge, and in turn, be characterised, by using a square root procedure.

---

[1] An exception is the fractional quantum Hall effect, which relies on electron-electron interaction[117].

5.3 Results

Within the publication[M6] in section 8.3 it is presented how non-quantised topological indices emerge in a one-dimensional system, despite having robust edge states that are experimentally confirmed. To explain this phenomena, a framework for a square root procedure is introduced, leading to quantised topological indices. The main findings are summarised below.

5.3.1 Aharonov–Bohm cages

The model, used to demonstrate the findings, consists of a rhombic chain threaded by a flux of ϕ, as depicted in Fig. 5.1a. The lattice sites are weakly coupled with a coupling strength c along the lines, the unit cell is indicated by the dashed box, and its elements are labelled a_n, b_n, c_n respectively. The corresponding Hamiltonian, after applying a Fourier transform, takes the form

$$H(k) = c \begin{pmatrix} 0 & 1+\mathrm{e}^{-\mathrm{i}k} & \mathrm{e}^{-\mathrm{i}\phi}+\mathrm{e}^{-\mathrm{i}k} \\ 1+\mathrm{e}^{\mathrm{i}k} & 0 & 0 \\ \mathrm{e}^{\mathrm{i}\phi}+\mathrm{e}^{\mathrm{i}k} & 0 & 0 \end{pmatrix}. \tag{5.1}$$

The resulting band structure for $\phi = 0$ and $\phi = \pi$ is depicted in Fig. 5.1b and c, respectively, showing that for a flux of $\phi = \pm\pi$ all bands become flat, which corresponds to the Aharonov–Bohm caging effect[125,126]. In this regime, all wave spreading comes to a halt, due to destructive interference. The following analysis will be focused on this specific parameter, since it is realised in the experiments, however, numerous theoretical considerations can be extended to arbitrary flux (see Supplementary Information in section 8.3).

Evaluating the Zak phase (see Eq. (2.11)) for $\phi = \pi$ leads to values of $\mathcal{Z}_\nu = \left\{\frac{\pi}{2}, \pi, \frac{\pi}{2}\right\}$, for the upper ($\nu = 1$), central ($\nu = 2$) and lower ($\nu = 3$) band, correspondingly, which are not quantised in units of π. Nevertheless, the values are restricted by nonsymmorphic symmetries of the form

$$\chi = \begin{pmatrix} 1 & 0 & 0 \\ 0 & -\mathrm{e}^{-\mathrm{i}k} & 0 \\ 0 & 0 & -\mathrm{e}^{-\mathrm{i}\phi}\mathrm{e}^{-\mathrm{i}k} \end{pmatrix} \qquad \Pi = \begin{pmatrix} 1 & 0 & 0 \\ 0 & \mathrm{e}^{-\mathrm{i}k} & 0 \\ 0 & 0 & \mathrm{e}^{-\mathrm{i}\phi}\mathrm{e}^{-\mathrm{i}k} \end{pmatrix}, \tag{5.2}$$

which transform the Hamiltonian $H(k)$ (see Eq. (5.1))

$$\Pi H(k) \Pi^{-1} = H^*(k) \qquad \chi H(k) \chi^{-1} = -H^*(k). \tag{5.3}$$

This translates to the Zak phase by restricting $\mathcal{Z}_1 + \mathcal{Z}_3 \in \{0, \pi\}$ and $\mathcal{Z}_2 \in \{0, \pi\}$, due to the Π symmetry, and $\mathcal{Z}_1 = \mathcal{Z}_3 \in \{0, \pm\pi/2\}$ and $\mathcal{Z}_2 \in \{0, \pi\}$, due to the χ symmetry. However, despite the non-quantised Zak phase, the system exhibits robust boundary states (for the disorder analysis see section 5.3.3 below), which have the eigenenergies $\sqrt{2}c$.

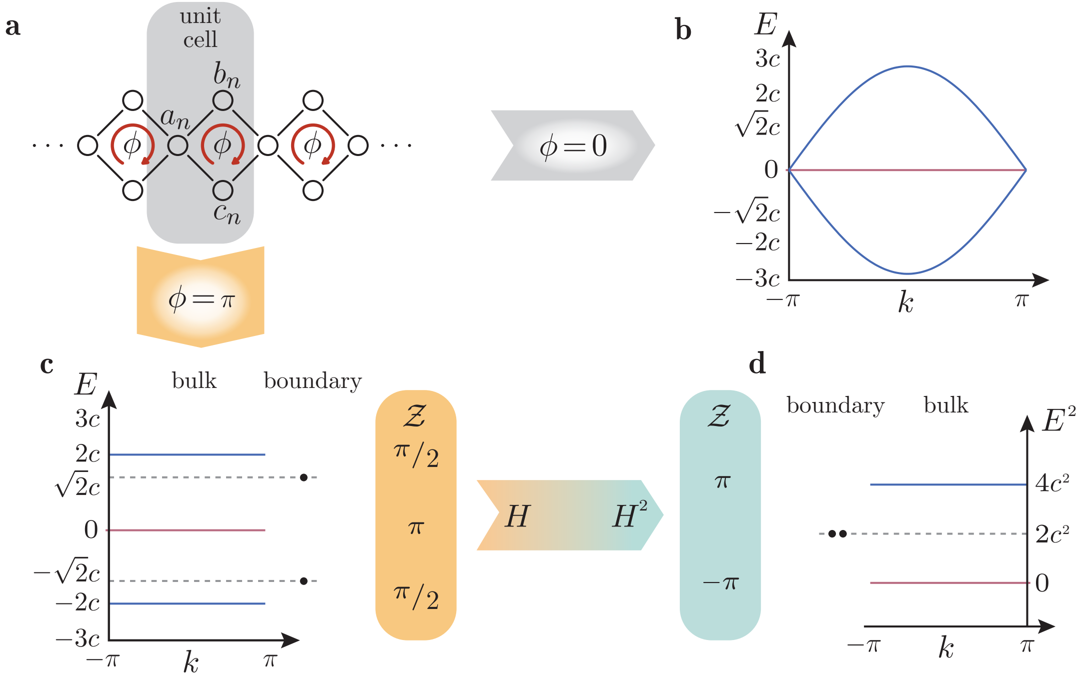

Figure 5.1 Lattice structure and band structures: a The lattice structure, together with its unit cell is displayed. The lattice sites are coupled along the black lines. **b, c** The band structures for the cases $\phi = 0$ and $\phi = \pi$ are displayed respectively. For the latter case, the energies of the boundary states and the Zak phases of the bands are included. **d** The band structure of the squared Hamiltonian, together with the Zak phases and the energy of the boundary states is displayed. (Adapted from [M6])

5.3.2 Squaring operation

The seemingly contradictory findings from the previous section are resolved by applying a squaring procedure, as depicted in Fig. 5.1d, where the squared energy of H is shown, together with the eigenvalues of the boundary states. It may be noted that the boundary states are now midgap states, positioned in the center of the gap between the two bands, similar to the SSH model, as discussed in section 2.3. If one evaluates the topological invariant of the squared system one finds that the topological invariants are quantised. Since two bands are degenerate, due to the squaring operation, it is necessary to use the Wilzcek–Zee phase (see Eq. (2.16)) which serves as a generalised Zak's phase. The resulting quantisation of the topological index is a result of the underlying symmetries since the squaring operation preserves the symmetries, resulting in $\mathcal{Z}_{1,3} \in \{0, \pi\}$ and $\mathcal{Z}_2 \in \{0, \pi\}$, due to both Π and χ symmetry individually.

It was therefore possible to identify the underlying topological structure of $H(k)$ (see Eq. (5.1)) by squaring it. In other words, $H(k)$ can be seen as a square root topological insulator, emerging from $H^2(k)$. In order to properly define the square root operation, the Hamiltonian is expanded into Gell-Mann matrices and the properties of the underlying algebra is used (see Supplementary Information in section 8.3 for the details).

5.3.3 Robustness

The previously claimed robustness of the topological boundary mode is investigated by studying the average energy offset as well as the average second moment under the influ-

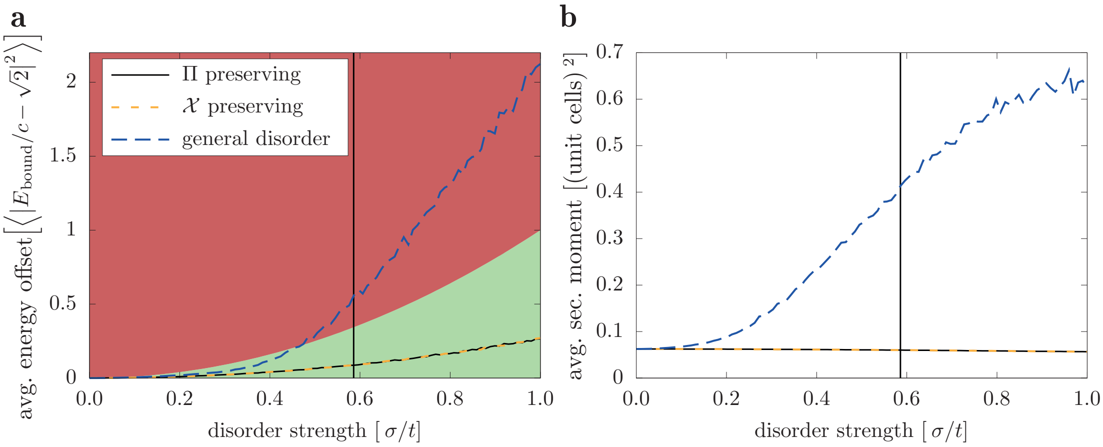

Figure 5.2 Energy deviations and localisation: a The averaged mean squared energy difference $\langle|E_{\mathrm{bound}}/c-\sqrt{2}|^2\rangle$ of the boundary state E_{bound} in the presence of disorder compared to the undisturbed system $E=\sqrt{2}c$, is plotted against the disorder strength σ. The different disorder types either preserve one of the symmetries (χ or Π) or break both. The disorder distribution has a vanishing mean and the gap between the boundary state and the nearest bulk band is displayed by the vertical line. The coloured areas represent an energy offset bigger (red) or smaller (green) than $(\sigma/c)^2$, defining the energy scale of the disorder. For the simulations a lattice with 99 sites was used. Every disorder strength σ was realised 10000 times. **b** Using the same parameters as in a, the averaged second moment of the boundary mode is shown, representing its localisation. (Adapted from [M6])

ence of disorder (Fig. 5.2). Since the topological properties originate from the underlying symmetries, as described in the previous section, the disorder is designed to specifically protect or break a certain symmetry. Based on the previous findings, it is sufficient if either Π or χ symmetry is present, since both individually lead to a quantisation of the Zak phase. In this vein, three disorder types are probed, Π preserving and χ breaking disorder, χ preserving and Π breaking disorder, and a disorder that breaks both, Π and χ symmetry. As displayed in Fig. 5.2 the energy, as well as localisation of the boundary mode is protected if at least one symmetry is present. This is in agreement with the characteristic robustness expected for topological boundary modes.

5.3.4 Experimental realisation

In order to realise the previously described structure with the femtosecond laser writing technique (see section 2.4), it is not sufficient to just fabricate the waveguides in a rhombic arrangement, since a flux of $\phi=\pi$ needs to be present. The positive refractive index change leads to positive coupling constant, which, in turn, results in a vanishing flux. This problem is resolved by using an auxiliary waveguide, with a specifically tailored detuning, in between two evanescently coupled waveguides[127]. This arrangement results in a negative coupling between the outer waveguides, while the auxiliary waveguide is energetically decoupled from the others (see Fig. 5.3a). By using either one (or three) auxiliary waveguides per plaquette, a flux of $\phi=\pi$ is achieved.

In order to confirm the presence of flux, the bulk of a lattice with 15 waveguides, corresponding to five unit cells, and an inter site coupling of $|c| = 0.85\,\mathrm{cm}^{-1}$, is excited. According to the theoretical predictions, spreading is inhibited in this case, due to the Aharonov–Bohm caging effect based on destructive interference. This behaviour can be

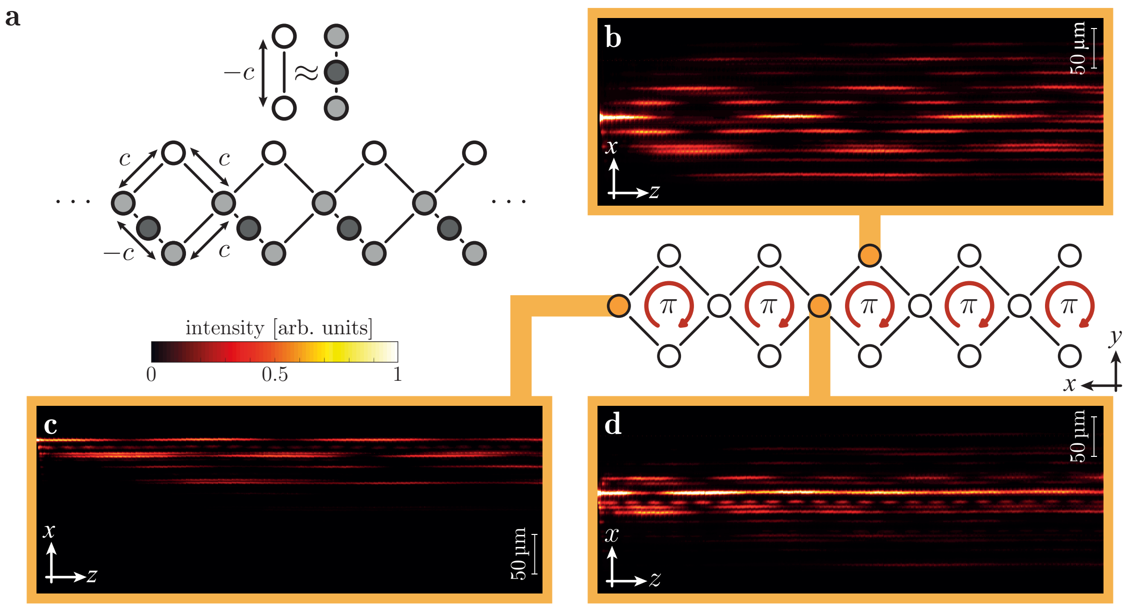

Figure 5.3 Negative coupling and fluorescence images: a The mapping to achieve negative coupling by using and auxiliary waveguide is sketched, together with the resulting lattice structure. **b-d** The fluorescence images obtained from single site excitations are displayed. The excited lattice site is indicated by the orange filling. The samples have a length of 10 cm. (Adapted from [M6])

confirmed, as displayed in Fig. 5.3b and d, which clearly show a caging effect. Due to weak excitations of neighbouring waveguides, small deviations between theory and experiment arise. The oscillation patterns occur, since several modes are excited simultaneously. While for the excitation displayed in Fig. 5.3b all modes are excited, only two modes are excited for the case shown in Fig. 5.3d. From the latter one it is, furthermore, possible to retrieve the energy difference between the modes by measuring the oscillation period, which leads to $\Delta E_{\text{bulk}} = 3.48\,\text{cm}^{-1} \pm 0.10\,\text{cm}^{-1}$.

In a second step the topological edge state is excited and measured, as displayed in Fig. 5.3c. As predicted, the boundary mode stays localised at the edge, due to its topological protection. Furthermore, it shows a distinct oscillation pattern, due to the overlap between the boundary modes, which possess the theoretical energies $E_{\text{bound}} = \pm\sqrt{2}c$. By measuring the oscillation period an energy difference of $\Delta E_{\text{bound}} = 2.44\,\text{cm}^{-1} \pm 0.07\,\text{cm}^{-1}$ can be retrieved. By comparing the energy differences of the bulk and boundary modes, it is possible to obtain the energy ratio, which yields $\Delta E^2_{\text{bulk}}/\Delta E^2_{\text{bound}} = 2.03 \pm 0.23$ from the experimental data, compared to a value of $\Delta E^2_{\text{bulk}}/\Delta E^2_{\text{bound}} = 2$ from the theoretical considerations. These considerations confirm the energy relations of the different modes in the presence of a flux of $\phi = \pi$.

5.3.5 Relation to current research and outlook

The previously outlined results offer a roadmap to take the square root of of a Hamiltonian in order to reveal its topological properties. Different approaches have been pursued to also aim for a useful notion of a square root. One strategy uses supercharges to intertwine two previously decoupled systems to form a topological non-trivial system[109]. This is in contrast to the previously discussed work since its main focus is to create a topological non trivial system and not to reveal its topological origin. Another work[115,116] differs in a similar way, where the square root operation is connected to a doubling of the underlying Hilbert space. Furthermore, it discusses Zak phases, which are quantised in both the original and the square root systems. This is in stark contrast to the previously discussed findings, which offer an explanation to non-quantised topological indices, which emerge in square root systems.

Experimentally the Aharonov–Bohm caging effect is also realised by using a different, intriguing approach[128,129], which uses temporal modulations (along the z-coordinate) of the waveguide structure. While this method offers the possibility to realise arbitrary flux, it requires a finely tuned set of parameters. This is in contrast to the previously discussed method of using a detuned auxiliary waveguide, which allows for a flux that is always fixed at a value of $\phi = \pi$.

A completely different method to achieve an Aharonov–Bohm caging effect is pursued in another recent work with different collaboration partners and a different experimental platform[M10]. In this work, modes with orbital angular momentum are used to achieve a non-vanishing flux[130,131], instead of changing the geometry of the lattice. It hence manipulates the flux solely by its input signal.

For future work it remains open, if the supersymmetric and square root operations can be united in a generalised concept. Furthermore, it could be investigated if the different approaches of treating non-quantised topological indices can be unified or categorised.

6 Non-Abelian geometric phases

In this chapter it is elucidated how non-Abelian geometric phases, which are closely related to non-Abelian fields, naturally arise in energetically degenerate structures and, in turn, how those can be realised with coupled waveguides. The design is optimised by using the concept of the quantrum metric. After giving a short introduction about those two concepts, a summary of the corresponding publication in section 8.4 is provided, where an experimental demonstration of non-Abelian geometric phases is presented.

6.1 Non-Abelian fields

The following elaborations about non-Abelian gauge fields are mainly based on [11,132]. Non-Abelian gauge fields are associated with fields that are locally symmetric under phase, or in general, unitary transformations. As an example, the action and Lagrangian density of a one-component, complex, scalar field ϕ is invariant under a transformation $\phi \mapsto \phi' = \mathrm{e}^{\mathrm{i}\alpha}\phi$, with a constant α, like it is the case for the Schrödinger equation. However, in order to assure a local invariance with an $\alpha = \alpha(x,t)$, one needs to couple the field to a gauge potential A, which adds a term that adapts the transformation of the derivatives. By using this procedure of minimal coupling, the partial derivatives (∂_μ) are replaced by covariant derivatives (D_μ) [11].

$$\partial_\mu \phi \mapsto D_\mu \phi = \partial_\mu \phi + A_\mu \tag{6.1}$$

this definition assures the transformation $D_\mu(A')\phi' = \mathrm{e}^{\mathrm{i}\alpha} D_\mu(A)\phi$, if

$$A_\mu \mapsto A'_\mu = A_\mu - \mathrm{i}\partial_\mu \alpha(x,t). \tag{6.2}$$

Note that for this chapter the greek letters are used to label spacetime indices. Hence, μ takes the values $(0,1,2,3,4)$. Furthermore, the Einstein summation convention applies. With these definitions, the action and Lagrangian density are invariant under the local phase transformations. The commutator of the covariant derivatives leads to the field strength tensor

$$[D_\mu, D_\nu] = F_{\mu\nu}, \tag{6.3}$$

which is known e.g. known from electrodynamics for an Abelian gauge field with symmetry group SU(1). The whole procedure can be adapted to multi-component fields with N components that are invariant under a local unitary transformation

$$\phi^i \mapsto \phi'^j = U_{ji}\phi^i, \tag{6.4}$$

where U is a unitary matrix, and where the superscript index labels the components. By using the minimal coupling principle as described before, one finds that the resulting gauge field $\mathcal{A}$ needs to be a matrix-valued quantity, of dimension $N \times N$ for each component. It needs to transform according to

$$\mathcal{A}_\mu \mapsto \mathcal{A}'_\mu = U\mathcal{A}_\mu U^\dagger + U\partial_\mu U^\dagger, \tag{6.5}$$

which again assures the invariance of the the action and Lagrangian density. Note that in this case the components $\mathcal{A}_\mu$ are matrix valued and in general not commuting, providing the notion of a non-Abelian gauge field. Importantly these are interacting fields, as becomes clear when looking at Eq. (6.3), since the commutator between different field components $\mathcal{A}_\mu$ does not vanish. An important example for the application of non-Abelian gauge fields is in quantum chromodynamics, which is the theory of strong interactions, which has the symmetry group SU(3).

6.1.1 Parallel transport

Besides local quantities, like the field strength tensor in Eq. (6.3), it is also possible to construct non-local quantities. These are important when dealing with gauge fields and one example are the so-called Wilson loops $\mathcal{W}_\mathcal{C}$. Those emerge when calculating the parallel transport of a (multi component) field ϕ in presence of a gauge field. Mathematically this is achieved by demanding a vanishing of the covariant derivative

$$D_\mu \phi = 0 \tag{6.6}$$

along a closed path $\mathcal{C}$. Evaluating this expression results in

$$\phi_\mathcal{C} = \hat{\mathcal{U}}(\mathcal{C}, \mathcal{A})\phi_0 \quad \text{where} \quad \hat{\mathcal{U}}(\mathcal{C}, \mathcal{A}) = \hat{\mathcal{T}}\exp\left(-\oint_\mathcal{C} \mathrm{d}x^\mu \mathcal{A}_\mu\right), \tag{6.7}$$

with the time ordering operator $\hat{\mathcal{T}}$. This leads to the gauge invariant expression

$$\mathcal{W}_\mathcal{C} = \mathrm{tr}\left(\hat{\mathcal{U}}(\mathcal{C}, \mathcal{A})\right), \tag{6.8}$$

which is not influenced by choosing a different gauge. By evaluating Wilson loops it is e.g. possible to reconstruct gauge potentials[133]. For the case of an Abelian gauge field the expression in the exponent is equivalent to the magnetic flux, and is for example used in this form when evaluating the Aharonov-Bohm effect[125].

6.1.2 Non-Abelian geometric phases

Despite being derived in the context of fundamental theories, non-Abelian gauge structures are a frequent appearance in any dynamics involving degenerate subspaces. This discovery of Frank Wilczek and Anthony Zee[49] offers a generalisation of the Berry phase[40] for degenerate eigenstates. However, it may be noted that similar mathematical structures were found already in 1929 by Van Vleck[134] but were not embedded in the mathematical context of geometric phases. Wilczek and Zee consider the evolution of a state governed by a Schrödinger-type equation confined to a degenerate subspace of the Hamiltonian H. This is achieved by adiabatically changing a set of parameters c_i. Starting with an initial state $\vec{\phi}_\text{init}$, one can calculate its propagation to a final state $\vec{\phi}_\text{fin}$ according to Eq. (2.7) when changing the parameters $c_i(z)$. However, if one is limited to a degenerate subspace and also demands that $c_i(z_\text{init}) = c_i(z_\text{fin})$, one finds for a finite-dimensional, discrete system

$$\vec{\phi}_\text{fin} = U\vec{\phi}_\text{init} \quad \text{with} \quad U = \hat{\mathcal{T}}\exp\left(-\oint_\mathcal{C} \mathrm{d}c^i \mathcal{A}_i\right) \tag{6.9}$$

where the components of the matrix $\mathcal{A}_i$ are given by

$$(\mathcal{A}_i)_{jk} = \vec{\mathcal{D}}_j^\dagger \frac{\partial}{\partial c^i} \vec{\mathcal{D}}_k, \tag{6.10}$$

with the degenerate set of eigenstates $\left\{\vec{\mathcal{D}}_i\right\}$ of the Hamiltonian H. The expression in Eq. (6.9) is identical to Eq. (6.7), which indicates the non-Abelian gauge structure. The gauge transformations translate to a change of basis, which act upon the gauge field $\mathcal{A}$, exactly as described in Eq. (6.5). The first experimental observation was achieved by using nuclear quadrupole resonances[135].

6.2 Quantum metric

The previously described parameter variation can be understood as the propagation of a state in a curved space. Therefore, it is possible to define a metric tensor g_{ij}, on this manifold[136–138]. Based on the projectors of the degenerate subspace $\mathcal{P} = \sum_i \vec{\mathcal{D}}_i \vec{\mathcal{D}}_i^\dagger$ it is possible to construct a line element and hence metric[136–139]

$$\mathrm{tr}\left(\frac{\partial}{\partial c^i}\mathcal{P}\frac{\partial}{\partial c^j}\mathcal{P}\right)\mathrm{d}c^i\mathrm{d}c^j = g_{ij}\mathrm{d}c^i\mathrm{d}c^j. \tag{6.11}$$

This expression is also known as the real part of the quantum geometric tensor. With the definition of a metric it is also possible to define a path length[136,138]

$$L = \int\limits_{z_{\mathrm{init}}}^{z_{\mathrm{fin}}} \sqrt{g_{ij}\frac{\partial c^i}{\partial z}\frac{\partial c^j}{\partial z}}\mathrm{d}z. \tag{6.12}$$

It was found that this quantity is part of the diabatic error that arises from a non-perfect adiabatic evolution[138]. This error is not based on the propagation time compared to the energy splitting, but solely relies on the geometric properties of the chosen path.

6.3 Results

In the publication[M5] presented in section 8.4, it is shown how the concept of non-Abelian gauge fields can be experimentally realised with waveguides. By using the properties of the quantum metric, an optimal design is found and several Wilson loops are measured. The main findings are summarised below.

6.3.1 Tripod structure

As a starting point an arrangement of waveguides is needed that possesses degenerate eigenstates, but is still relatively simple in order to reduce experimental inaccuracies. In this vein, a tripod structure is used, which was shown to be suitable for our purposes in a theoretical study[140]. The overal setting is similar to the stimulated Raman adiabatic passage (STIRAP) mechanism[141]. It is displayed in Fig. 6.1a and is characterised by the couplings $\{S, P, Q\}$ in-between the waveguides $\{L, R, U, C\}$. The resulting Hamiltonian reads

$$H = \begin{pmatrix} 0 & 0 & 0 & S \\ 0 & 0 & 0 & P \\ 0 & 0 & 0 & Q \\ S & P & Q & 0 \end{pmatrix}, \tag{6.13}$$

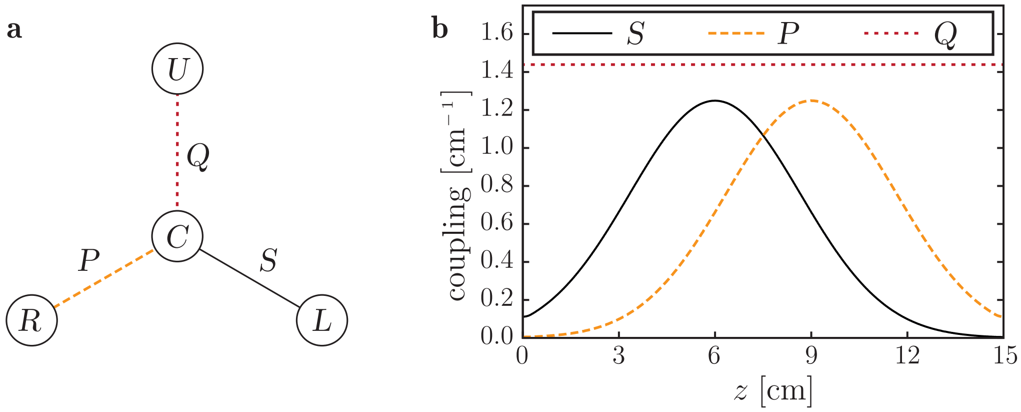

Figure 6.1 Tripod structure and coupling variation: a The waveguide arrangement, consisting of waveguides $\{L, R, U, C\}$, which are connected by the couplings $\{S, P, Q\}$ in-between the waveguides . **b** The couplings along the propagation direction is plotted. The colours and line styles are according to a. (Adapted from [M5])

when coupling the sites in the order $\{L, R, U, C\}$, hence sites $\{L, R, U\}$ are only coupled to site C. This Hamiltonian possesses two degenerate states, as needed (see 6.1.2 above), which read[140]

$$\vec{\mathcal{D}}_1 = \begin{pmatrix} \sin\theta \\ -\cos\theta \\ 0 \\ 0 \end{pmatrix} \qquad \vec{\mathcal{D}}_2 = \begin{pmatrix} \cos\theta\sin\varphi \\ \sin\theta\sin\varphi \\ -\cos\varphi \\ 0 \end{pmatrix}, \tag{6.14}$$

with $\theta = \arctan(P/S)$ and $\varphi = \arctan(Q/\sqrt{S^2+P^2})$, and both possess the eigenvalue 0. It may be noted that, first, both states have a vanishing intensity at the central site C, which is beneficial for the experimental validation, and, second it is sufficient to parametrise both states with only two parameters, despite having three couplings. The latter fact results from the normalisation of the eigenstates, which fixes one degree of freedom.

6.3.2 Non-Abelian gauge field

For the experimental implementation the situation is chosen that Q is constant while S and P are varied along the propagation direction which simplifies the experimental constraints but still allows for a suitable implementation of non-Abelian geometric phases. Following the procedure outlined in 6.1.2 and in a more detailed fashion in the appendix of the publication in section 8.4 one finds for the components of the gauge potential

$$\mathcal{A}_S = \mathrm{i}\,\frac{PQ}{(S^2+P^2)\sqrt{S^2+P^2+Q^2}}\,\sigma_y \tag{6.15}$$

$$\mathcal{A}_P = -\mathrm{i}\,\frac{SQ}{(S^2+P^2)\sqrt{S^2+P^2+Q^2}}\,\sigma_y, \tag{6.16}$$

where σ_y corresponds to the second Pauli matrix. From those expressions, the Wilson loop (Eq. (6.7) and (6.9)) can be calculated. The resulting expressions may be found in[140] or in the appendix of the publication at section 8.4.

6.3.3 Experimental design

For the implementation of different Wilson loops, the couplings S and P are varied along the propagation direction in a Gaussian shape, as depicted in Fig. 6.1b. The pattern follows the pulse sequences known from the STIRAP protocol[140,141] and takes the limits

$$\lim_{z\to z_{\mathrm{init}}} \frac{P(z)}{S(z)} = 0 \quad \text{and} \quad \lim_{z\to z_{\mathrm{fin}}} \frac{S(z)}{P(z)} = 0. \tag{6.17}$$

This simplifies the form of the dark states at the beginning and the end of the sequence, since $\vec{\mathcal{D}}_1(z_{\mathrm{init}})$ has its only non-vanishing contribution at site L, while $\vec{\mathcal{D}}_2(z_{\mathrm{init}})$ has its only non-vanishing contribution at site R. At the end facet this relation is interchanged. As a consequence, it is not only possible to selectively excite $\vec{\mathcal{D}}_1$ or $\vec{\mathcal{D}}_2$, but also to retrieve the population of those at the end of the sequence, by just measuring the intensities in the corresponding waveguides L and R. From the initial and final state populations (intensities) it is then possible to retrieve the elements of the unitary evolution (see Eq. (6.7) and (6.9)) and in turn calculate the Wilson loops. However, it is important to note that the whole line of argumentation crucially relies on the adiabaticity of the evolution which in turn is limited by the experimental constraints. The two most significant restrictions are the sample length, which is limited to 15 cm and the coupling, which should be sufficiently small in order to avoid effects that are beyond the tight binding model. Furthermore, it is crucial to avoid coupling in-between L, R and U, which arises if the waveguides are in close proximity. However, in order to achieve an adiabatic evolution it is desirable to have a big energy splitting (hence big couplings) together with a long sample length.

6.3.4 Quantum metric

Based on the concluding remarks of the previous section, the concept of the quantum metric is used to find a suitable set of parameters, for which the diabatic error is minimised, under the constraint of a limited sample length and limited coupling. This error is used, since it is not based on the propagation time compared to the energy splitting, but solely relies on the geometric properties of the chosen path. This also means that the optimisation is performed independent of the input signal, which is beneficial for designing (quantum) gates, where different inputs are used.

Using the definitions of the dark states in Eqs. (6.14) it is possible to derive the corresponding quantum metric (see Eq. (6.11)), which reads

$$g = 2\begin{pmatrix} 1 & 0 \\ 0 & \cos^2\varphi \end{pmatrix}. \tag{6.18}$$

Based on this quantity the path length of Eq. (6.12) is calculated for the parameters that define the pulse sequence, like amplitude, width and position. By minimizing this path length an optimal set of parameters is found.

In order to underline the effectiveness of the quantum metric optimisation, we also compare it with simulations of the full propagation, where we integrate over the intensity in the central waveguide C, while taking into account both possible dark-state excitations. We chose this measure, since the states $\vec{\mathcal{D}}_1$ or $\vec{\mathcal{D}}_2$ never populate the central site C. Any excitation in the central waveguide is thus a clear sign of leakage out of the subspace which does not happen in a perfectly adiabatic evolution. Both simulations show a similar trend, however, the quantum metric optimisation has two major benefits. First, the resulting curves over the parameter space are much smoother, which makes it easier to find an

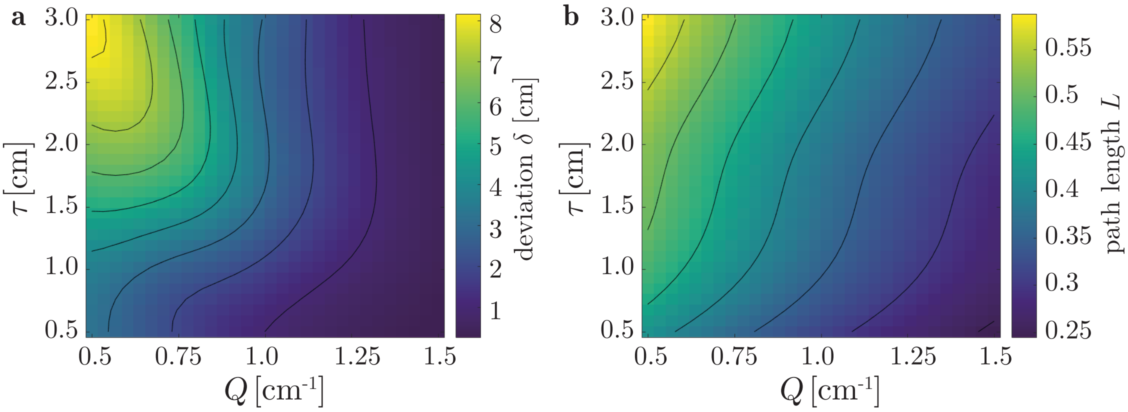

Figure 6.2 Bright state deviations and path length: a The integrated intensity of the central waveguide C along the propagation is plotted, taking into account both possible dark-state excitations. It is dependent on the coupling Q, and the shift of the Gaussian shaped couplings of S and P against each other. **b** The path length, based on the quantum metric, is plotted over the same parameter space as in a. (Adapted from [M5])

optimum. This is based on the fact that the intensity of the central waveguide is used and not a projection upon the eigenstates. Nevertheless, we chose this measure since it is easily accessible. Second, the computational effort is much lower when using the quantum metric, since it is not necessary to simulate the full propagation but instead one only has to solve a one-dimensional integral. Two exemplary plots are displayed in Fig. 6.2 for the strength of the coupling Q, and the shift τ of the peak of the Gaussian shaped couplings of S and P against each other, which clearly show the same trend. Other comparisons may be found in the appendix of the publication in section 8.4.

6.3.5 Experimental results

Based on the setting and optimisation explained above, three different Wilson loops, hence three different curves through the parameter space, are implemented and measured. As described above, the samples are exited at a single site and the intensities at the end facet are measured. An exemplary intensity distribution of the end facet is depicted in Fig. 6.3a, where it is clearly visible that the central waveguide C is almost not populated, which is a sign of the adiabatic evolution. The positions of the waveguides L and R are not symmetric, since the two Gaussian functions of the couplings are shifted against each other, which means that coupling S is already smaller than P (see Fig. 6.1b), and hence that L is further away from the central waveguide than R. From those intensities the values of the Wilson loops are calculated. The results are summarised in Fig. 6.3b and are in good agreement with the theoretical predictions. The adiabaticity of the evolution is also probed by means of fluorescence microscopy (see section 2.4), where it is confirmed that the central waveguide C is almost not populated during the whole propagation. The corresponding measurement may be found in Fig. 3 in the publication in section 8.4.

6.3.6 Relation to current research and outlook

The implementation of non-Abelian geometric phases is especially important for holonomic quantum computation, where the holonomy, associated with a loop $\mathcal{C}$ is given by the unitary evolution in Eq. (6.9)[142,143]. The presented setting is also generalised to highly degenerate

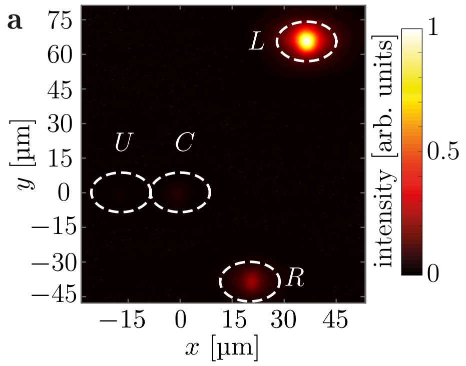

b

$\lvert W_{\mathcal{C}}^{\text{theo}}\rvert$	$\lvert W_{\mathcal{C}}^{\text{exp}}\rvert$
0.88	0.87 ± 0.04
0.97	1.00 ± 0.05
1.07	1.13 ± 0.06

Figure 6.3 Intensity distribution and experimental results: a The intensity distribution at the end facet of a 15 cm long waveguide structure is shown, from which the Wilson loops are calculated. **b** The calculated and measured Wilson loops for different paths through parameter space. The details concerning the exact couplings may be found in the publication in section 8.4. (Adapted from [M5])

structures to implement other symmetry groups[144], which is an important advantage over two level systems, which are limited to the SU(2). Other approaches to achieve non-Abelian structures are by means of braiding[145], artificial atoms in superconducting circuits[146], by using a spin-orbit coupling in cold atoms[147,148] or light[149], by coupling levels of the hyperfine ground states of rubidium-87[150], or by manipulating the polarisation e.g. by using phase modulations and the Faraday effect[151].

In a next step the experiments could be extended to the quantum regime by using single photons. Furthermore, it could be investigated if the quantum metric can be related to the concept of shortcut to adiabaticity[152], since both aim at a similar goal.

7 Conclusion

In this thesis the interplay of symmetries and topology was studied, using laser written waveguide arrays. As elaborated in the introduction, these symmetries are taking a special role, within the field of physics, since they are often not part of a common classification. Starting from the symmetries of non-Hermitian systems, the thesis also covers the role of partner Hamiltonians that have been constructed to either manipulate of reveal the topological properties. It concludes with continuously changing Hamiltonians that lead to non-Abelian geometric phases, normally known from quantum field theory.

The first object under investigation was the discrete PT symmetry, which can lead to real eigenvalues of a Hamiltonian, despite being non-Hermitian. In order to approach this topic experimentally, a novel method to introduce isotropic loss was introduced, which has also found application in different settings. With this method at hand, it was possible to create and study a two-dimensional PT symmetric lattice. This lattice was designed to possess a topological phase transition, as well as a PT phase transition. Both could be measured in the performed experiments and matched the theoretical predictions.

For the second topic, the impact discrete supersymmetric transformations have upon the topological phases of the archetypical SSH model was investigated. It was found that topological protection can be lifted and re-established from the edge states. The crucial ingredient to explain this behaviour has been the chiral symmetry of the lattice, which needs to be inherited by the supersymmetric transformations in order to preserve topological protection. These considerations were experimentally demonstrated by measuring and comparing the topological edge states as well as the non-topological edge states. Furthermore, it was shown that both states share the same eigenvalue, which is a crucial property of supersymmetric partners. An important experimental tool for those measurements was the use of a white light source in order to investigate the wavelength dependency of the waveguide structure.

The concept of partner Hamiltonians was extended in the next work, where the new class of square root topological insulators was used to reveal the topology of a Hamiltonian by using a squaring operation. Instead of creating a partner Hamiltonian with a different topology, one establishes a map to reveal the topological properties. The key to experimentally demonstrate this concept was the introduction of a negative coupling to enable the Aharonov-Bohm caging effect. After measuring the caging effect and thereby validating the negative coupling, the edge states have been measured.

For the fourth topic, the Hamiltonian is not just related to a single partner Hamiltonian, but is, moreover, continuously changed during the propagation. This procedure gave rise to non-Abelian geometric phases, which have been measured by evaluating Wilson loops. In order to fulfil the demanding experimental constraints, the quantum metric has been applied as a precise, yet computationally undemanding, tool for optimisation.

Along the way of attaining a suitable experimental implementation of the desired models, some concepts have been established that might be, or already have been, adapted for different applications. This concerns especially the novel method of creating tailored loss by dwelling. It offers the possibility to implement an isotropic loss mechanism and it neither relies on the existence of PT symmetry, nor on the existence of topological edge states. Another example is the application of the quantum metric to find the most adiabatic evolution, based solely on the underlying geometry. The optimisation is therefore independent of the input signal, which might prove useful when designing quantum gates that rely on adiabatic evolution.

While the previously outlined findings shed more light on the interplay of topology and symmetries, but they have also opened up several new questions, which might hopefully answered in the future. Can the supersymmetric and square root operations be united in a generalised concept? Can the quantum metric be related to the concept of *shortcut to adiabaticity*? Is it possible to use discrete SUSY transformations in higher dimensions to manipulate topological edge transport?

8 Publications for this thesis

This chapter contains four papers and the corresponding supplementary information, which serve as foundation for this thesis. All papers have been published in open access peer reviewed journals under a CC-BY licence (`https://creativecommons.org/licenses/by/4.0/`). The manuscripts have not been changed. The individual author contributions are giving prior to the manuscripts.

8.1 Demonstration of a two-dimensional PT-symmetric crystal

M. Kremer, T. Biesenthal, L.J. Maczewsky, Matthias Heinrich, Ronny Thomale, and Alexander Szameit *Demonstration of a two-dimensional $\mathcal{PT}$-symmetric crystal*, Nature Communications **10**, 435 (2019).
DOI: `https://doi.org/10.1038/s41467-018-08104-x`
Author Contributions:

Mark Kremer	project idea, conceptual design, calculation of band structures and topological invariants, sample design based on simulations, experimental determination of the sample parameters, sample fabrication, measurement of topological and PT symmetry phase transition, data acquisition, data evaluation, figure art, preparation of initial manuscript draft
Tobias Biesenthal	preparation of the manuscript, measurement of loss parameters
Lukas J. Maczewsky	preparation of the manuscript, support with sample design
Matthias Heinrich	preparation of the manuscript
Ronny Thomale	preparation of the manuscript, supervision
Alexander Szameit	preparation of the manuscript, supervision

nature COMMUNICATIONS

ARTICLE

https://doi.org/10.1038/s41467-018-08104-x OPEN

Demonstration of a two-dimensional $\mathcal{PT}$-symmetric crystal

Mark Kremer[1], Tobias Biesenthal[1], Lukas J. Maczewsky[1], Matthias Heinrich[1], Ronny Thomale[2] & Alexander Szameit[1]

With the discovery of $\mathcal{PT}$-symmetric quantum mechanics, it was shown that even non-Hermitian systems may exhibit entirely real eigenvalue spectra. This finding did not only change the perception of quantum mechanics itself, it also significantly influenced the field of photonics. By appropriately designing one-dimensional distributions of gain and loss, it was possible to experimentally verify some of the hallmark features of $\mathcal{PT}$-symmetry using electromagnetic waves. Nevertheless, an experimental platform to study the impact of $\mathcal{PT}$-symmetry in two spatial dimensions has so far remained elusive. We break new grounds by devising a two-dimensional $\mathcal{PT}$-symmetric system based on photonic waveguide lattices with judiciously designed refractive index landscape and alternating loss. With this system at hand, we demonstrate a non-Hermitian two-dimensional topological phase transition that is closely linked to the emergence of topological mid-gap edge states.

---

[1] Institute for Physics, University of Rostock, Albert-Einstein-Straße 23, 18059 Rostock, Germany. [2] Department of Physics and Astronomy, Julius-Maximilians-Universität Würzburg, Am Hubland, 97074 Würzburg, Germany. Correspondence and requests for materials should be addressed to A.S. (email: alexander.szameit@uni-rostock.de)

In 1998, Carl M. Bender and Stefan Boettcher challenged the conventional wisdom of quantum mechanics that the Hamiltonian operator describing any quantum mechanical system has to be Hermitian[1]. They showed that Hamiltonians that are invariant under combined parity-time ($\mathcal{PT}$) symmetry transformations likewise can exhibit entirely real eigenvalue spectra[2]. This insight had a particularly profound impact in the field of photonics, where $\mathcal{PT}$-symmetric potential landscapes can be implemented by appropriately distributing gain and loss for electromagnetic waves[3–5]. Following this approach, it became possible to observe some of the hallmark features of $\mathcal{PT}$ symmetry, such as the existence of non-orthogonal eigenmodes[6] and exceptional points[7,8], diffusive coherent transport[9], and to study their implications in settings including nonlinearity[10], $\mathcal{PT}$-symmetric lasers[11,12], and topological phase transitions[13–15]. Similarly, $\mathcal{PT}$-symmetry has enriched other research fields ranging from $\mathcal{PT}$-symmetric atomic diffusion[16], superconducting wires[17,18], and $\mathcal{PT}$-symmetric electronic circuits[19].

Nevertheless, to this date, all experimental implementations of $\mathcal{PT}$-symmetric systems have been restricted to one effective spatial dimension, which is mostly due to technological limitations involved in realizing appropriate non-Hermitian potential landscapes.

In this work, we report on the experimental realization and characterization of a two-dimensional $\mathcal{PT}$-symmetric system by means of photonic waveguide lattices with judiciously designed refractive index landscape and alternating loss. A key result of our work is the demonstration of a non-Hermitian two-dimensional topological phase transition that coincides with the emergence of mid-gap edge states. Our findings lay the foundation for future investigations exploring the full potential of $\mathcal{PT}$-symmetric photonics in higher dimensions. Moreover, our approach may even hold the key for realizing two-dimensional $\mathcal{PT}$-symmetry beyond photonics, e.g., in matter waves and electronics.

Results

Theory. $\mathcal{PT}$-symmetric systems are described by a Hamiltonian that is invariant under parity-time symmetry transformations[1]. In a more formal language, this means that if the Hamiltonian $\hat{H}$ commutes with the $\mathcal{PT}$-operator: $\left[\hat{H}, PT\right] = 0$, and the Hamiltonian shares the same set of eigenstates with the $\mathcal{PT}$-operator, then the entire set of eigenvalues of $\hat{H}$ is real. A necessary condition for this symmetry to hold is that the underlying potential obeys the relation $\hat{V}(-x) = \hat{V} * (x)$[1]. Whereas complex potentials tend to be difficult to realize in most physical systems, in 2007 it was shown that photonics provides a suitable testbed due to the complex-valued character of the refractive index[3,4]. Since then, $\mathcal{PT}$-symmetric systems have been explored in a variety of photonic platforms, ranging from waveguide arrays[6], fiber lattices[7], and coupled optical resonators[20] to plasmonics[21] and microwave cavities[22]. The implementation of $\mathcal{PT}$-symmetry in photonics is based on the observation that the Schrödinger equation of quantum mechanics for the probability amplitude $\psi(x, y, t)$,

$$i\hbar\frac{\partial}{\partial t}\psi(x,y,t) = -\frac{\hbar^2}{2m}\nabla^2\psi(x,y,t) + V(x,y,t)\psi(x,y,t), \quad (1)$$

and the paraxial Helmholtz equation of electromagnetism for the electric field amplitude $E(x, y, z)$,

$$i\frac{n_0}{2k_0}\frac{\partial}{\partial z}E(x,y,z) = -\frac{n_0}{2k_0^2}\nabla^2 E(x,y,z) - n(x,y,z)E(x,y,z), \quad (2)$$

are formally equivalent if the potential $V(x, y, t)$ in the Schrödinger equation is replaced by the refractive index profile $-n(x, y, z)$ in the Helmholtz equation[23]. $\mathcal{PT}$-symmetry then translates into the following condition for the complex refractive index:

$$n(-x,-y,z) = n^*(x,y,z) \quad (3)$$

In other words, the real part $\mathrm{Re}(n(x, y, z))$ needs to follow a symmetric distribution, while the imaginary part $\mathrm{Im}(n(x, y, z))$ has to be antisymmetric under the parity operation. In general, the latter implies that loss in one propagation direction has to be compensated by an identical gain in the opposite direction[3]. It turns out, however, that this stringent requirement can be relaxed in tight-binding systems, where an alternating loss distribution is sufficient to obtain $\mathcal{PT}$-symmetric behavior[9,24]. Indeed, such passive systems exhibit exactly the same evolution dynamics that one would expect in active structures if one accounts for a constant global loss by normalizing the field intensity, an approach we followed up on in our work.

Nevertheless, to date $\mathcal{PT}$-symmetry was only realized in one-dimensional (1D) systems, which drastically limits the spectrum of accessible physical effects. For example, the second spatial degree of freedom in two-dimensional (2D) structures allows for the study of various additional symmetries, such as rotation, and their interplay with $\mathcal{PT}$-symmetry. Moreover, one can introduce anisotropy with much more variety than in just one dimension. Furthermore, some physical effects fundamentally change their characteristics depending on the dimensionality, such as Anderson localization. This also applies to nonlinear optics, in particular solitons, which exhibit entirely different properties in 2D systems. The dimensionality is likewise of great importance for topological systems, since topological indices such as Chern number, Z2 invariant or Bott index in general necessitate at least a two-dimensional parameter space in which they can be defined. Moreover, chiral edge states can exist only along the edge of a 2D system. In our work, we break new grounds by devising a platform for the implementation of 2D $\mathcal{PT}$-symmetry that may enable future studies of this wide range of effects.

Setting. We consider so-called "photonic graphene", a regular arrangement of waveguides in a honeycomb geometry (sketched in Fig. 1a)[25]. In order to establish the necessary potential condition for $\mathcal{PT}$-symmetry Eq. (3), the two triangular sublattices of the honeycomb may exhibit different loss, symbolized by the yellow and blue filling of the individual lattice sites, respectively. We describe the light evolution in this system by the tight-binding approximation of Eq. (2), which reads as[26]:

$$i\partial_z a_{m,n} = i\gamma a_{m,n} + c\left(b_{m-1,n} + b_{m,n+1} + b_{m,n-1}\right) \quad (4a)$$

$$i\partial_z b_{m,n} = -i\gamma a_{m,n} + c\left(a_{m+1,n} + a_{m,n+1} + a_{m,n-1}\right) \quad (4b)$$

The $a_{m,n}$ and $b_{m,n}$ denote the amplitudes at the lattice sites of the two sublattices, γ describes the gain/loss, and c is the coupling constant.

Launching a light beam into the waveguides results in spatial beam dynamics (governed by Eqs. (4a) and (4b)) that, for the case of neither gain nor loss in both sublattices, resembles the evolution of a single electron in carbon-based graphene according to Eq. (1). One of the striking features of the graphene band structure is the existence of the so-called Dirac region in the vicinity of the conical intersection points ("diabolical points") between the first and the second bands, displayed in Fig. 1b. In these regions, the tight-binding Hamiltonian of our $\mathcal{PT}$-symmetric photonic graphene can be expanded into a Taylor series[26] to obtain a mathematical structure resembling the Dirac equation

$$\hat{H} = c\sqrt{3}\tilde{\nu}\sigma_1 + c\sqrt{3}\tilde{\mu}\sigma_2 + i\gamma\sigma_3 \quad (5)$$

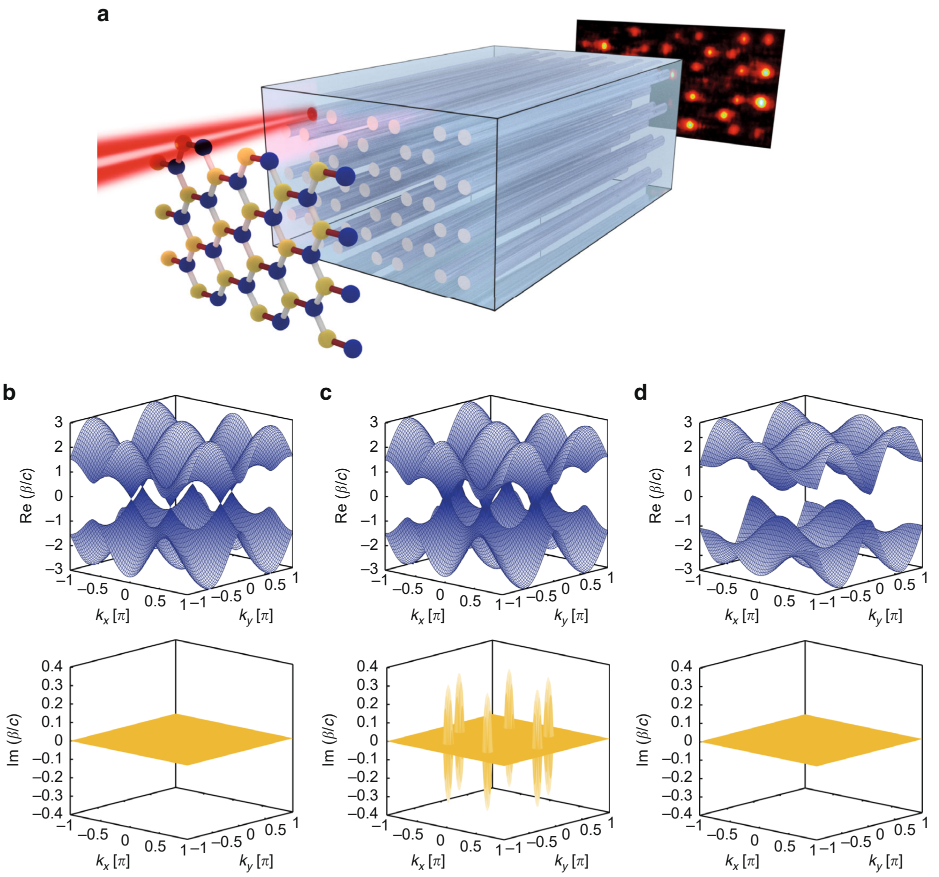

Fig. 1 The $\mathcal{PT}$-symmetric graphene lattice. **a** Due to the quantum-optical analogy between solids and waveguide lattices, the probability amplitude of a single electron in a carbon graphene lattice shares the same evolution equation as a light beam injected into a honeycomb waveguide lattice. **b** The dispersion relation of a graphene lattice with no gain/loss and no strain ($\tau = 1$), **c** with gain/loss and no strain ($\tau = 1$), and **d** with gain/loss above the critical point ($\tau > 2 + \frac{\gamma}{c}$), which corresponds to the unbroken $\mathcal{PT}$-symmetry regime

that describes relativistic quantum particles. Here, $\sigma_{1,2,3}$ are the Pauli matrices:

$$\sigma_1 = \begin{pmatrix} 0 & 1 \\ 1 & 0 \end{pmatrix}; \sigma_2 = \begin{pmatrix} 0 & -i \\ i & 0 \end{pmatrix}; \sigma_3 = \begin{pmatrix} 1 & 0 \\ 0 & -1 \end{pmatrix}; \qquad (6)$$

2γ denotes the difference in loss between the sublattices, and c is the intersite hopping. The quantities $\tilde{\mu}$ and $\tilde{\nu}$ represent the components of the transverse wave vector k_x, k_y measured from the position of the original Dirac point. For simplicity, we suppressed an additional term $-i\Gamma\sigma_0$ that arises from the passive nature of our system, where Γ is the average loss of both sublattices, and σ_0 is the unity matrix. The non-Hermitian Hamiltonian in Eq. (5) exhibits a complex dispersion relation with a non-real eigenvalue spectrum[27]. Mathematically, complex eigenvalues of the Hamiltonian appear whenever the $\mathcal{PT}$-operator and the Hamiltonian cease to share all of their eigenvectors. Such a system is said to have broken $\mathcal{PT}$-symmetry, although the $\mathcal{PT}$-operator still commutes with the Hamiltonian. This seeming paradox stems from the fact that the $\mathcal{T}$-operator is anti-linear. A graph of the real part of the graphene dispersion relation with $\frac{\gamma}{c} = 0.32$ is shown in Fig. 1c. In contrast to “conventional” (i.e., dissipation-less) graphene, the real part of the dispersion relation is now a single-sheeted hyperboloid. The lower part of Fig. 1c shows the imaginary part of the dispersion relation, highlighting the purely imaginary eigenvalues around the original vertices.

One can drive the system back into the unbroken $\mathcal{PT}$-symmetry regime by applying a linear strain τ, where $\tau = 1$ corresponds to the unstrained case. This strain is applied as indicated in Fig. 1a by the red connections between the atoms. In Hermitian lattices ($\gamma = 0$), increasing the strain pushes pairs of Dirac points towards one another until they merge at $\tau = 2$[28]. For any given loss factor γ, all eigenvalues of the system become real above a threshold strain $\tau \geq 2 + \frac{\gamma}{c}$ [26]. Therefore, in such a setting, the structure can exhibit unbroken $\mathcal{PT}$-symmetry, with the transition occurring exactly at $\tau = 2 + \frac{\gamma}{c}$. The Hamiltonian of this system reads as[26]

$$\hat{H} = \left[c(\tau - 2) - \frac{3}{2}c\tau\tilde{\mu}^2 + c\tilde{\nu}^2\right]\sigma_1 + c\tau\sqrt{3}\tilde{\mu}\sigma_2 + i\gamma\sigma_3, \qquad (7)$$

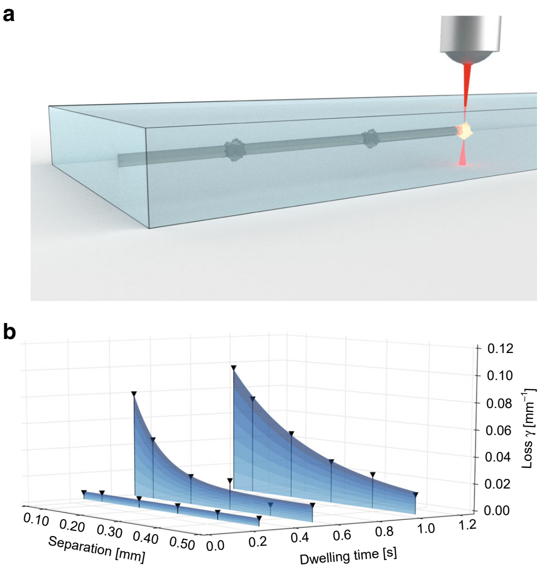

Fig. 2 Realizing artificial loss. **a** Schematic of the artificial scatterers introduced during the fabrication process by dwelling. **b** Experimentally obtainable artificial losses as a function of dwelling time and separation of the scatter centers

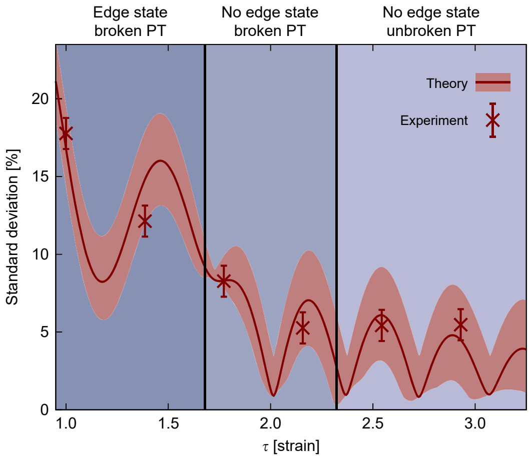

Fig. 3 Demonstration of the phase transition from broken to unbroken $\mathcal{PT}$-symmetry. The standard deviation of the output intensity pattern resulting from 6 excitations (3 unit cells). In the unbroken $\mathcal{PT}$-symmetric phase, this quantity approaches zero. The simulations are performed by using the Schrödinger equation in the tight binding limit Eqs. (4a) and (4b). The red shaded area represents the calculated uncertainty arising from possible unequal incoupling in the experiment, whereas the error bars account for fluctuations of the measured data. The blue shaded regions show the three distinct phases associated with the strain and loss parameters of our structure (see Fig. 4a)

with $\Delta = c(\tau - 2)$ denoting the gap in the spectrum[26]. In Fig. 1d, we show the real and imaginary parts of the dispersion relation for photonic graphene with the same loss factor as in Fig. 1c in the presence of a strain given by $\tau = 2 + \frac{\gamma}{c} + 0.61$. Evidently, all eigenvalues are real, and a gap has opened in accordance with Eq. (7).

Experimental methods. In order to implement the $\mathcal{PT}$-symmetric photonic graphene lattice, we employ the direct laser-writing technology[29]. The desired loss in the system is realized by introducing a certain concentration of microscopic scattering points along the waveguides by dwelling, as sketched in Fig. 2a. As both the dwelling time and the separation between the individual scattering points can be freely tuned, this approach allows for a wide range of artificial losses to be chosen without compromising the real part of the refractive index or introducing directionality into the system. Figure 2b shows our calibration measurements of the realized loss, as a function of dwelling time and scattering point separation. The general trends are clearly visible: the cumulative loss experienced by light propagating through the waveguides systematically increases the smaller the separations and the longer the dwelling times. The strain is realized by reducing the distance between the waveguides with the red connection bond, shown in Fig. 1a, while the distances between the waveguides with the gray connection bonds are kept constant.

$\mathcal{PT}$-phase transition. With these tools at hand, we can now proceed to experimentally demonstrate the $\mathcal{PT}$-symmetry transition in our 2D photonic graphene lattice. When no strain is present, $\mathcal{PT}$-symmetry is broken and, hence, the spectrum is complex. After a certain propagation distance, the remaining light tends to reside predominantly in the lossless sublattice[30]. As the strain is increased, however, the system enters the regime of unbroken $\mathcal{PT}$-symmetry, resulting in a real spectrum. This transition can be readily visualized by exploiting the fact that in the broken $\mathcal{PT}$-phase, the eigenvalues exhibit a wide range of different imaginary parts, and the power remaining in the lattice depends strongly on the injection site. In contrast, the unbroken $\mathcal{PT}$-phase is by definition characterized by all eigenvalues having the same imaginary part and, for an infinite system, the power decay in the lattice becomes entirely independent of the excited waveguide. Therefore, as the strain is increased above the critical value of $\tau = 2 + \frac{\gamma}{c}$, the standard deviation of the transmitted power will eventually vanish[14]. Furthermore, one has to take into account that the modes are non-orthogonal even in the unbroken $\mathcal{PT}$-regime, hence the power is not preserved[3] and one does not observe a sharp drop of the standard deviation at the transition point. We demonstrate this behavior by fabricating 6 samples with $\gamma = 0.15\,\mathrm{cm}^{-1}$, a coupling of $c = 0.475\,\mathrm{cm}^{-1}$ and strains ranging from $1 \leq \tau \leq 2.9$. In each sample, we perform 6 single-channel excitations of bulk sites, corresponding to 3 unit cells, and measure the total power remaining in the lattice at the output facet. The extracted data is plotted in Fig. 3. As expected, the variance substantially decreases and tends toward zero as the lattice is brought into its unbroken phase.

Topological phase transition. The phase transition from the broken to the unbroken $\mathcal{PT}$-symmetry regime in the graphene lattice is inextricably linked to a topological phase transition related to the emergence of topological mid-gap states. Figure 4a summarizes this feature in a τ–γ phase diagram. The presence or absence of topological mid-gap states at the edge of the Hermitian graphene lattice ($\gamma = 0$) can be reconciled from the perspective of the winding number in a Su–Shrieffer–Heeger (SSH) chain perpendicular to the edges[31,32]. A topological phase transition from a

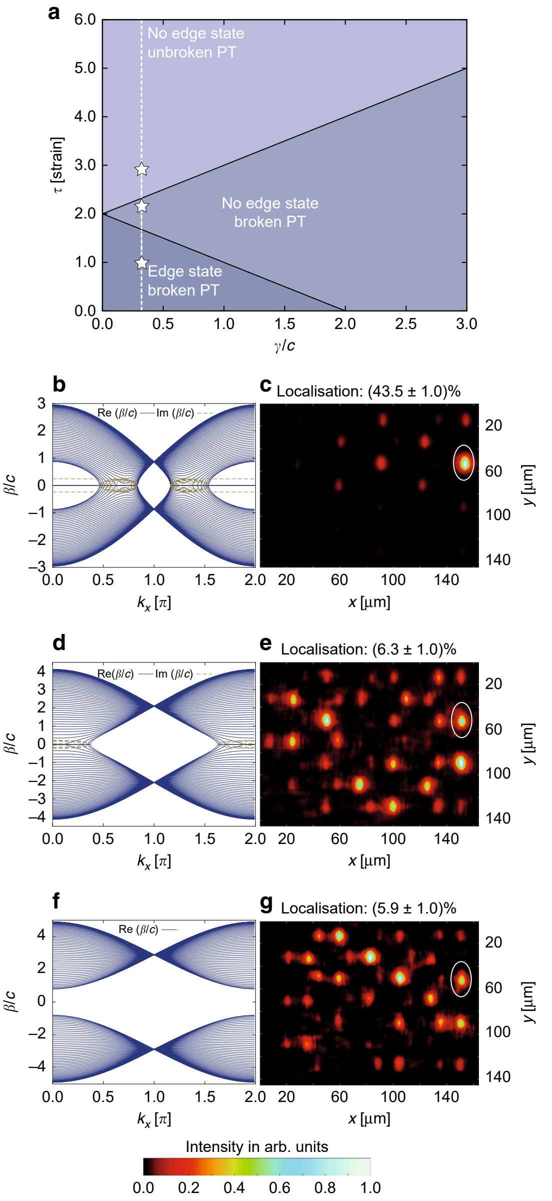

Fig. 4 Demonstration of the topological transition in the $\mathcal{PT}$-symmetric structure. **a** The τ–γ phase diagram shows three distinct phases associated with the strain and loss parameters of our structure. The three stars correspond to the parameters used in (**b**)–(**g**). **b** For a strain of $\tau < 2 - \frac{\gamma}{c}$, the system is in the broken $\mathcal{PT}$-symmetric phase and topological mid-gap states are present. In the left panel, the corresponding dispersion relation is shown. **c** Experimental image at the sample output facet, where light was injected into the marked edge waveguide and remains close to the edge as the mid-gap state exists. The ratio of light in the marked waveguide in proportion to the intensity of all waveguides is about 43.5%. **d** For an intermediate strain $2 - \frac{\gamma}{c} < \tau < 2 + \frac{\gamma}{c}$, the system is still in the broken $\mathcal{PT}$-symmetric phase, but the topological mid-gap states cease to exist. In the left panel, the corresponding dispersion relation is shown. **e** Experimental image at the sample output facet, where light was injected into the marked edge waveguide and spreads into the bulk as no mid-gap state exists. The ratio of light in the marked waveguide in proportion to the intensity of all waveguides is about 6.3%. **f** For sufficiently strong strain $\tau > 2 + \frac{\gamma}{c}$, the system is finally driven into the unbroken $\mathcal{PT}$-symmetric phase, where no topological mid-gap states exist either. In the left panel, the corresponding dispersion relation is shown. **g** Experimental image at the sample output facet, where light was injected into the marked edge waveguide and spreads into the bulk as no mid-gap state exists. The ratio of light in the marked waveguide in proportion to the intensity of all waveguides is about 5.9%

2D topological semimetal to a trivial insulator, accompanied by a change of the SSH winding number, takes place at $\tau = 2$[28,33,34]. For any $\gamma > 0$, however, a topological mid-gap state spontaneously breaks $\mathcal{PT}$-symmetry, since its real dispersive part is pinned. As a consequence, the unbroken $\mathcal{PT}$-symmetric domain of the τ–γ phase diagram does not exhibit any edge modes, as shown in Fig. 4a. In other words, one can either observe unbroken $\mathcal{PT}$-symmetry, or topological mid-gap states, but never both at the same time, since the two phenomena are mutually exclusive[35]. Interestingly, a third domain is wedged between the previously discussed cases in the phase diagram. It arises when the strain τ exceeds the gap threshold determined by γ. As the gap is closed, $\mathcal{PT}$-symmetry is invariably broken—yet, as long as the hyperboloids in the real part of the dispersion relation still touch, topological mid-gap states are prevented from forming at the bearded edge[36]. This can be intuitively explained by the shape of these states, which are known to reside exclusively within one of the sublattices, and, hence, experience solely $+\gamma$ or $-\gamma$. As a consequence, the imaginary part of the mid-gap dispersion is $\pm\gamma$ and, from the perspective of a $\mathcal{PT}$-symmetric SSH chain, this implies the disappearance of the mid-gap state for $\tau \geq 2 - \gamma/c$[14,36]. Therefore, when starting in the topologically non-trivial domain with mid-gap states and broken $\mathcal{PT}$-symmetry, and following a vertical trajectory (fixed γ and increasing τ) in the phase diagram, the system passes not one but two phase transitions. The first one is of topological nature and occurs when the direct gap of the topological mid-gap states closes at $\tau = 2 - \gamma/c$. The second occurs at $\tau = 2 + \gamma/c$ when the gapped unbroken $\mathcal{PT}$-symmetric domain is reached (see Fig. 4a).

These transitions are exactly what we observe in our experiment. For the unstrained system ($\tau = 1$) and a loss of $\gamma = 0.15\ \mathrm{cm}^{-1}$ such that $\frac{\gamma}{c} = 0.32$, the systems exhibits topological mid-gap states (Fig. 4b), which we excite by launching light into an edge waveguide (Fig. 4c). Upon increasing the strain to $\tau = 2.2$, the mid-gap edge states disappear, in the dispersion relation (Fig. 4d) as well as in experiment (Fig. 4e). However, the system is still in the broken $\mathcal{PT}$-symmetric phase, as shown in Fig. 3b. By further increasing the strain to $\tau = 2.9$, we finally drive the system into the unbroken $\mathcal{PT}$-symmetric phase, whereas the mid-gap states are likewise absent (see Fig. 4f for the dispersion relation and Fig. 4g for the experimental data). Our results clearly show the close links between $\mathcal{PT}$-symmetric and topological phase transitions, and their related transition points as shown in Fig. 4a. This rich interplay stems from the fact that it is the very existence of a band gap that allows for the proper definition of a topological invariant in this structure.

Discussion

In our work, we devised and experimentally demonstrated a 2D $\mathcal{PT}$-symmetric crystal, using an optical platform. To this end, we developed a technology to efficiently introduce artificial losses into the system and unequivocally proved that our realized structure is indeed in the unbroken $\mathcal{PT}$-symmetric phase. Moreover, we highlighted the close connection of a $\mathcal{PT}$-symmetry phase transition to a topological phase transition in our graphene lattice. These findings lay the foundations for realizing 2D $\mathcal{PT}$-symmetry in other wave systems beyond photonics, such as matter waves, sound waves, and possibly even plasmonics and electronic circuits. Moreover, our work opens the gate for future investigations exploring the full potential of $\mathcal{PT}$-symmetry in higher dimensions and may provide the tools to experimentally address numerous exciting questions such as the impact of nonlinearity, single photon interference, and many-body effects in 2D $\mathcal{PT}$-symmetric systems.

Methods

Fabrication of the structures. The waveguides were manufactured using the femtosecond laser writing method[29] in 10 cm long samples composed of fused silica glass (Corning 7980). The laser pulses are created by a regenerative Ti: Sapphire amplifier system (Coherent RegA 9000 seeded with a Mira 900) and exhibit an energy of 450 nJ @ 800 nm wavelength and 100 kHz repetition rate. A nano-positioning system in conjunction with a 20× microscope objective (0.35 NA) provides the highly accurate focusing of the laser beam 50–800 µm under the sample surface. By translating the sample with a speed of about 100 mm/min, the refractive index at the focal point is increased by approximately 7×10^{-4}, resulting in waveguides with a mode field diameter of 10.4 µm × 8 µm for the 633 nm illumination wavelength. Intrinsic propagation losses and birefringence were estimated to be 0.2 dB cm^{-1} and 10^{-6}, respectively.

Characterization of the structures. The single lattice site excitations were performed with light of 633 nm from a Helium–Neon laser (Melles-Griot, 35 mW). In order to focus into the sample a 10× microscope objective (0.25 NA) was used. The output facet was imaged with another 10× microscope objective onto a CCD camera (Basler Aviator). Upon characterization, the output intensity patterns resulting from the excitation of lossy sites were normalized to compensate for the systematically lower injection efficiency.

Data availability

All experimental data and any related experimental background information not mentioned in the text are available from the authors on reasonable request.

Received: 11 August 2018 Accepted: 7 December 2018
Published online: 25 January 2019

References

1. Bender, C. M. & Böttcher, S. Real spectra in non-Hermitian Hamiltonians having PT symmetry. *Phys. Rev. Lett.* **80**, 5243–5246 (1998).
2. Bender, C. M., Brody, D. C. & Jones, H. F. Complex extension of quantum mechanics. *Phys. Rev. Lett.* **89**, 270401-1–270401-4 (2002).
3. El-Ganainy, R., Makris, K. G., Christodoulides, D. N. & Musslimani, Z. H. Theory of coupled optical PT-symmetric structures. *Opt. Lett.* **32**, 2632–2634 (2007).
4. Makris, K. G., El-Ganainy, R., Christodoulides, D. N. & Musslimani, Z. H. Beam dynamics in PT symmetric optical lattices. *Phys. Rev. Lett.* **100**, 103904-1–103904-4 (2008).
5. El Ganainy, R. et al. Non-Hermitian physics and PT symmetry. *Nat. Phys.* **14**, 11–19 (2018).
6. Rüter, C. E. et al. Observation of parity-time symmetry in optics. *Nat. Phys.* **6**, 192–195 (2010).
7. Regensburger, A. et al. Parity-time synthetic photonic lattices. *Nature* **488**, 167–171 (2012).
8. Gangaraj, S. A. H. & Monticone, F. Topological waveguiding near an exceptional point: defect-immune, slow-light, and loss-immune propagation. *Phys. Rev. Lett.* **121**, 093901-1–093901-6 (2018).
9. Eichelkraut, T. et al. Mobility transition from ballistic to diffusive transport in non-Hermitian lattices. *Nat. Commun.* https://doi.org/10.1038/ncomms3533 (2013).
10. Musslimani, Z., Makris, K., Ganainy, R. El & Christodoulides, D. Optical solitons in PT periodic potentials. *Phys. Rev. Lett.* **100**, 030402-1–030402-4 (2008).
11. Feng, L., Wong, Z. J., Ma, R. M., Wang, Y. & Zhang, X. Single-mode laser by parity-time symmetry breaking. *Science* **346**, 972–975 (2014).
12. Hodaei, H., Miri, M. A., Heinrich, M., Christodoulides, D. N. & Khajavikhan, M. Parity-time-symmetric microring lasers. *Science* **346**, 975–978 (2014).
13. Zeuner, J. M. et al. Observation of a topological transition in the bulk of a non-Hermitian system. *Phys. Rev. Lett.* **115**, 040402-1–040402-5 (2015).
14. Weimann, S. et al. Topologically protected bound states in photonic PT-symmetric crystals. *Nat. Mater.* **16**, 433–438 (2017).
15. Li, M., Ni, X., Weiner, M., Alù, A. & Khanikaev. A. B. Topological phases and nonreciprocal edge states in non-Hermitian Floquet Insulators. Preprint at https://arxiv.org/abs/1807.00913 (2018).
16. Zhao, K. F., Schaden, M. & Wu, Z. Enhanced magnetic resonance signal of spin-polarized Rb atoms near surfaces of coated cells. *Phys. Rev. A* **81**, 042903-1–042903-11 (2010).
17. Rubinstein, J., Sternberg, P. & Ma, Q. Bifurcation diagram and pattern formation of phase slip centers in superconducting wires driven with electric currents. *Phys. Rev. Lett.* **99**, 167003-1–167003-4 (2007).
18. Chtchelkatchev, N. M., Golubov, A. A., Baturina, T. I. & Vinokur, V. M. Stimulation of the fluctuation superconductivity by PT symmetry. *Phys. Rev. Lett.* **109**, 150405-1–150405-5 (2012).
19. Schindler, J., Li, A., Zheng, M. C., Ellis, F. M. & Kottos, T. Experimental study of active LRC circuits with PT symmetries. *Phys. Rev. A* **84**, 040101-1–040101-5 (2011).
20. Peng, B. et al. Parity–time-symmetric whispering-gallery microcavities. *Nat. Phys.* **10**, 394–398 (2014).
21. Benisty, H. et al. Implementation of PT symmetric devices using plasmonics: principle and applications. *Opt. Express* **19**, 18004–18019 (2011).
22. Bittner, S. et al. PT symmetry and spontaneous symmetry breaking in a microwave billiard. *Phys. Rev. Lett.* **108**, 024101-1–024101-5 (2012).
23. Longhi, S. Quantum-optical analogies using photonic structures. *Laser Photonics Rev.* **3**, 243–261 (2009).
24. Ornigotti, M. & Szameit, A. Quasi PT-symmetry in passive photonic lattices. *J. Opt.* **16**, 065501 (2014).
25. Peleg, O. et al. Conical diffraction and gap solitons in honeycomb photonic lattices. *Phys. Rev. Lett.* **98**, 103901-1–103901-4 (2007).
26. Szameit, A., Rechtsman, M. C., Bahat-Treidel, O. & Segev, M. PT-Symmetry in honeycomb photonic lattices. *Phys. Rev. A* **84**, 021806-1–021806-5 (2011).
27. Zhen, B. et al. Spawning rings of exceptional points out of Dirac cones. *Nature* **525**, 354–358 (2015).
28. Bahat-Treidel, O. et al. Klein tunneling in deformed honeycomb lattices. *Phys. Rev. Lett.* **104**, 063901-1–063901-4 (2010).
29. Szameit, A. & Nolte, S. Discrete optics in femtosecond-laser-written photonic structures. *J. Phys. B* **43**, 163001 (2010).
30. Guo, A. et al. Observation of PT-symmetry breaking in complex optical potentials. *Phys. Rev. Lett.* **103**, 093902-1–093902-4 (2009).
31. Kohmoto, M. & Hasegawa, Y. Zero modes and edge states of the honeycomb lattice. *Phys. Rev. B* **76**, 205402-1–205402-6 (2007).
32. Lee, C. H. et al. Topolectrical circuits. *Commun. Phys.* https://doi.org/10.1038/s42005-018-0035-2 (2018).
33. Zhu, S.-L., Wang, B. & Duan, L. M. Simulation and detection of Dirac fermions with cold atoms in an optical lattice. *Phys. Rev. Lett.* **98**, 260402-1–260402-4 (2007).
34. Rechtsman, M. C. et al. Topological creation and destruction of edge states in photonic graphene. *Phys. Rev. Lett.* **111**, 103901-1–103901-5 (2013).
35. Hu, Y. C. & Hughes, T. L. Absence of topological insulator phases in non-Hermitian PT-symmetric Hamiltonians. *Phys. Rev. B* **84**, 153101-1–153101-4 (2011).
36. Esaki, K., Sato, M., Hasebe, K. & Kohmoto, M. Edge states and topological phases in non-Hermitian systems. *Phys. Rev. B* **84**, 205128-1–205128-19 (2011).

Acknowledgements

A.S. gratefully acknowledges the financial support from the Deutsche Forschungsgemeinschaft (Grants SZ 276/9-1, SZ 276/19-1, and SZ 276/20-1) and the Alfried Krupp von Bohlen und Halbach Foundation. R.T. is supported by DFG-SFB 1170 (Project B04) and ERC-StG-Thomale-TOPOLECTRICS-336012. The authors would also like to thank C. Otto for preparing the high-quality fused silica samples used in all the experiments presented here. A.S. and R.T. are supported by DFG-EXC 2471 „ct.qmat“.

Author contributions

M.K. and A.S. developed the idea and designed the structure. M.K., R.T., and A.S. worked out the theory. M.K., T.B., and L.J.M. fabricated the samples and performed the measurements. A.S. supervised the project. All authors discussed the results and co-wrote the paper.

Additional information

Supplementary Information accompanies this paper at https://doi.org/10.1038/s41467-018-08104-x.

Competing interests: The authors declare no competing interests.

Reprints and permission information is available online at http://npg.nature.com/reprintsandpermissions/

Journal peer review information: *Nature Communications* thanks the anonymous reviewers for their contribution to the peer review of this work. Peer reviewer reports are available.

Publisher's note: Springer Nature remains neutral with regard to jurisdictional claims in published maps and institutional affiliations.

Open Access This article is licensed under a Creative Commons Attribution 4.0 International License, which permits use, sharing, adaptation, distribution and reproduction in any medium or format, as long as you give appropriate credit to the original author(s) and the source, provide a link to the Creative Commons license, and indicate if changes were made. The images or other third party material in this article are included in the article's Creative Commons license, unless indicated otherwise in a credit line to the material. If material is not included in the article's Creative Commons license and your intended use is not permitted by statutory regulation or exceeds the permitted use, you will need to obtain permission directly from the copyright holder. To view a copy of this license, visit http://creativecommons.org/licenses/by/4.0/.

© The Author(s) 2019

8.2 Topological state engineering via supersymmetric transformations

G. Queraltó, M. Kremer, L. J. Maczewsky, M. Heinrich, J. Mompart, V. Ahufinger, and A. Szameit *Topological state engineering via supersymmetric transformations*, Communications Physics **3**, 49 (2020).
DOI: `https://doi.org/10.1038/s42005-020-0316-4`
Author Contributions:

Mark Kremer	project idea, conceptual design, symmetry analysis, sample design based on simulations from G. Q., experimental determination of the sample parameters, sample fabrication, fluorescence and whitelight measurements, data acquisition, data evaluation, figure art, preparation of initial manuscript draft
Gerard Queraltó	project idea, conceptual design, calculation of QR factorisation and SUSY partners, simulations based on parameters retrieved by measurements from M. K., figure art, preparation of initial manuscript draft
Lukas J. Maczewsky	preparation of the manuscript, parameter measurements
Matthias Heinrich	preparation of the manuscript, support with QR factorisation
Jordi Mompart	preparation of the manuscript, supervision
Verònica Ahufinger	preparation of the manuscript, supervision
Alexander Szameit	preparation of the manuscript, supervision

Note: The shared co-first authorship of Gerard Queraltó and Mark Kremer is based on the distinct contributions of both authors. The QR factorisation and the calculation of the superpartners has been performed by Gerard Queraltó, while the symmetry analysis and the experimental realisation is mainly the work of Mark Kremer.

COMMUNICATIONS PHYSICS

ARTICLE

https://doi.org/10.1038/s42005-020-0316-4 OPEN

Topological state engineering via supersymmetric transformations

Gerard Queraltó[1,3], Mark Kremer[2,3], Lukas J. Maczewsky[2], Matthias Heinrich[2], Jordi Mompart[1], Verònica Ahufinger[1] & Alexander Szameit[2]✉

The quest to explore new techniques for the manipulation of topological states simultaneously promotes a deeper understanding of topological physics and is essential in identifying new ways to harness their unique features. Here, we examine the potential of supersymmetric transformations to systematically address, alter and reconfigure the topological properties of a system. To this end, we theoretically and experimentally study the changes that topologically protected states in photonic lattices undergo as supersymmetric transformations are applied to their host system. In particular, we show how supersymmetry-induced phase transitions can selectively suspend and re-establish the topological protection of specific states. Furthermore, we reveal how understanding the interplay between internal symmetries and the symmetry constraints of supersymmetric transformations provides a roadmap to directly access the desirable topological properties of a system. Our findings pave the way for establishing supersymmetry-inspired techniques as a powerful and versatile tool for topological state engineering.

---

[1] Departament de Física, Universitat Autònoma de Barcelona, E-08193 Bellaterra, Barcelona, Spain. [2] Institut für Physik, Universität Rostock, Albert-Einstein-Straße 23, 18059 Rostock, Germany. [3] These authors contributed equally: Gerard Queraltó, Mark Kremer. ✉email: alexander.szameit@uni-rostock.de

Physical laws are intrinsically connected to symmetries, which can be classified in spacetime and internal symmetries. Unlike any other symmetry, supersymmetry (SUSY), originally developed as an extension of the Poincaré Group[1], offers a loophole to the Coleman–Mandula theorem[2], allowing the interplay of spacetime and internal symmetries in a nontrivial way[3]. Despite the lack of direct experimental evidence of SUSY in high-energy physics, where it establishes a relation between bosons and fermions[1], some of its fundamental concepts have been successfully adapted to numerous fields such as condensed matter[4], statistical mechanics[5], nonrelativistic quantum mechanics[6], optics[7,8], and cosmology[9]. In particular, SUSY provides an effective theory to describe quantum phase transitions occurring at the boundary of topological superconductors[10], where topological states characterized by topological invariants emerge[11,12]. In recent years, the field of photonics has shed light on a plethora of phenomena stemming from topological phases (as shown by Lu et al.[13] and Ozawa et al.[14]), and photonic lattices have been established as a versatile experimental platform[15–18]. In a similar vein, SUSY concepts have been introduced to photonics[8] to tackle the long-standing challenge of systematically shaping the modal content of highly multi-mode structures[19–26], controlling scattering characteristics[27–30], designing laser arrays[31,32], and creating band gaps in extremely disordered potentials[33] and topologically protected mid-gap states starting from trivial configurations[34].

In this work, SUSY transformations are applied to manipulate topological properties, which are deeply connected to internal symmetries of the systems. Specifically, we present a method for topological state engineering, e.g., to selectively suspend and re-establish the topological protection of a targeted state, which can be applied to systems described by a tight-binding Hamiltonian such as optical waveguides[35], coupled cavities[36], ultra-cold atoms[37], or acoustic and mechanical systems[38]. Furthermore, it is shown how closely this behavior is linked to symmetry constraints of SUSY transformations[39], enabling these symmetries to be fully or partially preserved, or cancelled in their entirety. As SUSY transformations are tailored to their specific purpose, they imprint their characteristic signature on the topological invariants, as well as the related topological protection. Here, to explore the fruitful interplay between SUSY and topology, we employ femtosecond laser written photonic lattices[35]. Specifically, to elucidate how SUSY enables the manipulation of topological properties, we apply discrete SUSY (DSUSY) transformations to photonic lattices embodying the simplest system with nontrivial topological properties, the Su–Schrieffer–Heeger (SSH) model[40]. Along these lines, we show that SUSY allows for the systematic breaking and recovery of symmetries of the system and thereby constitutes a powerful tool to tailor topological transitions and to manipulate the topological properties of a system.

Results

Theory. In its general quantum-mechanical formulation, unbroken SUSY connects two superpartner Hamiltonians $\mathcal{H}^{(1)}$ and $\mathcal{H}^{(2)}$, sharing a common set of eigenvalues except for the eigenvalue of the ground state of $\mathcal{H}^{(1)}$, which is removed from the spectrum of $\mathcal{H}^{(2)}$. A step forward toward a more general Hamiltonian spectrum manipulation, allowing the removal of different eigenvalues, can be achieved by applying DSUSY transformations[8]. Considering a one-dimensional lattice composed of N evanescently coupled single-mode waveguides, the system is characterized by a discrete Hamiltonian $\mathcal{H}$ given by an $N \times N$ tridiagonal matrix, with the propagation constants occupying the diagonal elements and the coupling strengths the off-diagonal elements. For the waveguide lattices employed here, light propagation along the z-direction can be described using coupled-mode equations[41]:

$$-i\frac{d}{dz}\mathbf{\Psi} = \mathcal{H}\mathbf{\Psi}, \tag{1}$$

where $\mathbf{\Psi} = \left(\psi_1, \dots, \psi_N\right)^T$, with ψ_j describing the modal field amplitude in waveguide j. From the eigenvalue equation

$$\mathcal{H}\mathbf{\Psi}_s = \lambda_s\mathbf{\Psi}_s, \qquad (2,)$$

which relates the eigenfunction $\mathbf{\Psi}_s$ and eigenvalues λ_s of the state s, superpartner Hamiltonians

$$\mathcal{H}_m^{(1)} = \mathcal{H} - \lambda_m I = QR \text{ and } \mathcal{H}_m^{(2)} = RQ, \tag{3}$$

can be obtained using the QR factorization[42], where Q is an orthogonal matrix $(Q^TQ) = I$, R an upper triangular matrix, and I the identity matrix. Note that, in general, the QR factorization is not unique and could lead to different solutions sharing the same eigenvalue spectrum (see Supplementary Note 1).

The superpartner Hamiltonian $\mathcal{H}_m^{(2)}$ shares a common set of eigenvalues with $\mathcal{H}_m^{(1)}$, except for λ_m that has been removed from the spectrum of $\mathcal{H}_m^{(2)}$. In addition, the standard SUSY transformation annihilating the fundamental state can still be carried out with this method, as displayed in Fig. 1a. The corresponding eigenvalue λ_m is removed because its eigenstate $\mathbf{\Psi}_m$ is completely localized in the fully decoupled Nth waveguide and, as such, does not have any influence on the dynamics of the remaining system of $N-1$ waveguides (see Supplementary Fig. 1). By applying these transformations in an iterative way, superpartner structures with desired eigenvalue spectra can be engineered by removing the desired number of eigenvalues, reducing the overall system size. A question that naturally arises, and to this date remains unexplored, is the impact of targeting a state with nontrivial topological properties. Does its removal irrevocably change the topological properties of the system?

The SSH model, one of the most prominent systems for illustrating topological physics, can be implemented using a one-dimensional lattice of evanescently coupled waveguides with two alternating couplings c_1 and c_2 ($c_1 < c_2$). While an infinite lattice is invariant under the exchange of couplings, the presence of edges in a finite SSH chain introduces two distinct types of edge terminations that, in turn, give rise to topological states that can be described by the bulk-edge correspondence and topological invariants. In particular, topological edge states, which can be quantified by a winding number $\mathcal{W} = \mathcal{Z}/\pi$, appear at the end of a region with nonzero Zak phase $\mathcal{Z}$, where $\mathcal{Z} = 0$ or π depending on the edge termination[43,44]. If the lattice terminates with the weak coupling c_1, the winding number is 1 and the lattice supports one topological edge state. On the contrary, if the lattice terminates with the strong coupling c_2, the winding number is 0 and the structure does not support an edge state, as displayed in Fig. 1b. The topological protection of these states is directly related with the existence of internal symmetries in the system. Specifically, the chiral symmetry given by

$$\Gamma\mathcal{H}\Gamma^\dagger = -\mathcal{H}, \tag{4}$$

where Γ is an unitary and Hermitian operator satisfying $\{\mathcal{H}, \Gamma\} = 0$, is responsible of the protection of the zero-energy states. By applying the chiral symmetry operator Γ to the eigenvalue Eq. (2), one obtains $\mathcal{H}(\Gamma\mathbf{\Psi}_s) = -\lambda_s(\Gamma\mathbf{\Psi}_s)$, which entails that the energy spectrum of the system is symmetric around 0. This fact, in turn, guarantees that all the states $\mathbf{\Psi}_s$ with positive energy λ_s have a counterpart $\Gamma\mathbf{\Psi}_s$ with negative energy $-\lambda_s$, with the exception of the zero-energy states, which are topologically protected (see Supplementary Note 2 for more details).

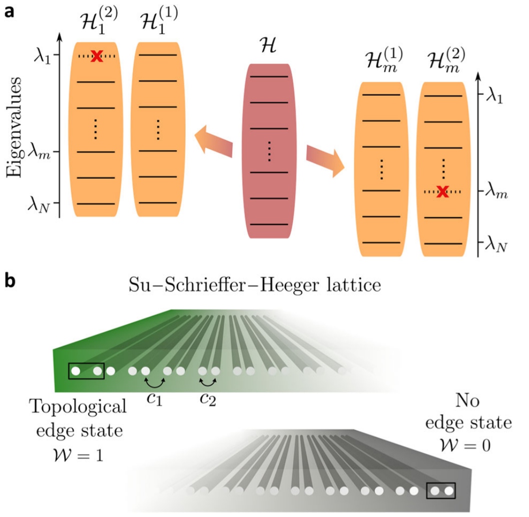

Fig. 1 Supersymmetric transformations and Su-Schrieffer-Heeger model. **a** Schematic representation of the eigenvalue spectrum of the Hamiltonian $\mathscr{H}$ and two sets of superpartner Hamiltonians $\{\mathscr{H}_1{}^{(1)}, \mathscr{H}_1{}^{(2)}\}$ and $\{\mathscr{H}_m{}^{(1)}, \mathscr{H}_m{}^{(2)}\}$, obtained by removing the eigenvalues λ_1 and λ_m using supersymmetric transformations, respectively. **b** Representation of a Su-Schrieffer-Heeger lattice implemented using optical waveguides, which are evanescently coupled with alternating couplings c_1 and c_2 ($c_1 < c_2$). Depending on the termination of the lattice, the structure has Winding number $\mathcal{W} = 1$ and supports a topological edge state on that edge or $\mathcal{W} = 0$ and does not support an edge state on that edge.

DSUSY transformations applied to the Hamiltonian can be expressed in terms of a transformation matrix V as

$$V\mathcal{H}_m^{(1)}V^{-1} = VQRV^{-1} = RQ = \mathcal{H}_m^{(2)}, \tag{5}$$

where $V = Q^{-1}$. If both $\mathcal{H}_m^{(1)}$ and V possess some symmetry, e.g., chiral symmetry satisfying $\{\mathcal{H}_m^{(1)}, \Gamma\} = \{V, \Gamma\} = 0$, then this symmetry is transferred to $\mathcal{H}_m^{(2)}$:

$$\mathcal{H}_m^{(2)} = V\mathcal{H}_m^{(1)}V^{-1} = -V\Gamma\mathcal{H}_m^{(1)}\Gamma^{\dagger}V^{-1} = -\Gamma\mathcal{H}_m^{(2)}\Gamma^{\dagger}. \tag{6}$$

On the other hand, if the transformation matrix V does not obey this symmetry, it will not be reproduced in the superpartner Hamiltonian $\mathcal{H}_m^{(2)}$ either. Exploiting this connection between symmetry constraints of DSUSY transformations and symmetries of the system, superpartner Hamiltonians with modified topological properties can be engineered, and thus establishing a new method for topological state engineering by combining SUSY isospectrality and breaking of symmetries of the system. As a proof of concept, three distinct structures are investigated: (i) the superpartner SP_1, obtained by removing the eigenvalue λ_1 corresponding to a bulk state (see Fig. 2a), (ii) the SSH supporting two topologically protected edge states (see Fig. 2b), and (iii) the superpartner $\mathrm{SP}_{N/2}$, obtained by removing the eigenvalue $\lambda_{N/2}$ corresponding to a topological edge state (see Fig. 2c), whose lattice configurations are schematically illustrated in Fig. 2d, e and f, respectively. Note that, due to the symmetry of the eigenvalue spectrum, equivalent results to the SP_1 and $\mathrm{SP}_{N/2}$ structures would be obtained by removing λ_N and $\lambda_{N/2+1}$, respectively. Subsequently, the degree of protection of the superpartner topological states is probed analytically with respect to their symmetries, as well as numerically by gauging their robustness against chiral disorder[45].

Supersymmetric topological photonic structures. Figure 2c shows the eigenvalue spectrum of the $\mathrm{SP}_{N/2}$ lattice obtained by removing the eigenvalue $\lambda_{N/2}$ corresponding to an edge state of the SSH structure. Since $\lambda_{N/2}$ is a zero-energy eigenvalue, the diagonal elements of the superpartner Hamiltonians $\mathcal{H}_{N/2}^{(1)}$ and $\mathcal{H}_{N/2}^{(2)}$ remain 0. Thus, the superpartner lattice is composed of waveguides with zero detuning (see Supplementary Note 1 for an extended discussion). Here, the transformation matrix possesses chiral symmetry, which is transferred to the superpartner Hamiltonian $\mathcal{H}_{N/2}^{(2)}$ that satisfies $\Gamma\mathcal{H}_{N/2}^{(2)}\Gamma^{\dagger} = -\mathcal{H}_{N/2}^{(2)}$. Therefore, the symmetries of the system are preserved and the topological properties of the remaining zero-energy eigenstate remain intact. By applying DSUSY transformations, two different superpartner lattices supporting one topological state $\mathbf{\Psi}_{N/2+1}$ can be obtained due to the nonunicity of the QR factorization process (see Supplementary Note 1). One supporting an interface state, as displayed in Fig. 2f, and the other supporting an edge state, mostly maintaining the form of Fig. 2e with interchanged couplings and the last waveguide removed. For the interface state solution, the $\mathrm{SP}_{N/2}$ structure resembles two SSH chains with different termination at the interface and strong coupling at the outer edges, as it is illustrated in Supplementary Fig. 3. The topologically protected interface state, whose position in the lattice can be controlled by changing the dimerization $|c_1 - c_2|$, is located between the two SSH lattices and decays exponentially into the bulk. The existence of this interface state is experimentally verified, as discussed in detail in the next section, and its robustness against chiral disorder maintaining the underlying symmetry of the lattice is numerically proved. In particular, by introducing chiral disorder, the deviation of the eigenvalue $\lambda_{N/2+1}$ is proved to be 0, while the eigenstate shape is slightly modified, although it remains localized at the interface. For the edge state solution, the $\mathrm{SP}_{N/2}$ structure resembles the SSH model with interchanged couplings and $N - 1$ waveguides, except for a localized deviation in the couplings with respect to c_1 and c_2 near the leading edge. Here, the transformation constitutes a topological phase transition in the sense that the couplings are interchanged and a waveguide removed, thus one of the edge states is annihilated. As earlier, the remaining edge state is topologically protected and robust against chiral disorder. Note that, by applying another DSUSY transformation removing the remaining zero-energy eigenvalue, the system becomes topologically trivial. Besides, the protocol could be implemented the other way around by applying inverse SUSY transformations[46], i.e., starting with the topologically trivial SSH model and adding a zero-energy eigenvalue to the spectrum. To sum up, by annihilating zero-energy eigenvalues, DSUSY transformations introduce topological phase transitions, leading to the displacement and destruction of topological states.

Let us now consider the SP_1 lattice, obtained by removing the eigenvalue λ_1 corresponding to a bulk state of the SSH structure, as it is displayed in Fig. 2a. Considering that the removal of any bulk state of the system per definition breaks the inversion symmetry of the eigenvalue spectrum, one would expect that the topological protection of the edge states is necessarily destroyed. Nevertheless, the chiral symmetry of the system is partially respected by the DSUSY transformation, preserving the topological protection of one edge state. This can be explained by separating the Hamiltonian $\mathcal{H}_1^{(2)}$ into $\mathcal{H}_{1L}^{(2)}$ and $\mathcal{H}_{1R}^{(2)}$, corresponding to the left and right parts of the lattice, respectively. The chiral symmetry of $\mathcal{H}_{1R}^{(2)}$ is preserved, satisfying $\Gamma\mathcal{H}_{1R}^{(2)}\Gamma^{\dagger} = -\mathcal{H}_{1R}^{(2)}$ and, thus, the topological protection of

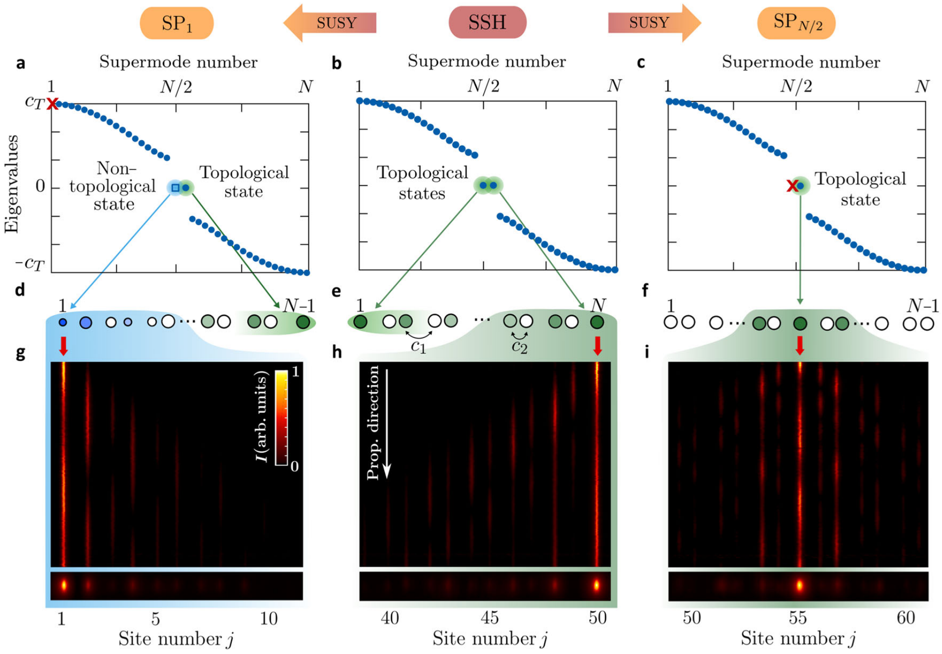

Fig. 2 Supersymmetric topological photonic structures. Eigenvalue spectrum of (**a**) the superpartner SP$_1$ lattice, obtained by removing a bulk state ($m = 1$), (**b**) the Su-Schrieffer-Heeger (SSH) lattice, and (**c**) the superpartner SP$_{N/2}$ lattice obtained by eliminating an edge state ($m = N/2$). The energy gap is $2|c_1 - c_2|$ and $c_T = c_1 + c_2$. Sketch of the (**d**) SP$_1$, (**e**) SSH, and (**f**) SP$_{N/2}$ lattices. Detuning (coupling) is indicated by the size (spacing) of (between) the circles. The intensity of the color inside each waveguide is proportional to the amplitude of the state. Experimentally observed light evolution along the propagation direction and output intensities for the (**g**) nontopological edge state, (**h**) topological edge state, and (**i**) topological interface state. The total length of the sample is $L = 10$ cm and the wavelength used to excite the waveguides is $\lambda = 633$ nm. The SSH, SP$_1$, and SP$_{N/2}$ lattices are composed of $N = 50$, $N = 49$, and $N = 109$ waveguides, respectively. The original SSH lattice used to synthetize the SP$_1$ (SP$_{N/2}$) lattice is composed of $N = 50$ ($N = 110$) waveguides, $c_1 = 0.5\,\mathrm{cm}^{-1}$ and $c_2 = 1.0\,\mathrm{cm}^{-1}$ ($c_2 = 1.8\,\mathrm{cm}^{-1}$). The different number of waveguides and coupling coefficients used to create the superpartner structures are due to experimental restrictions. In particular, the SP$_1$ lattice has weaker couplings to adjust the detunings below $2\,\mathrm{cm}^{-1}$ in order to guarantee that the couplings stay constant when changing the detuning.

the right edge state is maintained. On the contrary, the chiral symmetry of $\mathcal{H}_{1L}^{(2)}$ is destroyed by the appearance of nonzero diagonal elements, which take away the symmetry protection of the left edge state. However, the state remains localized at the edge due to the high detuning between waveguides. Moreover, although the left edge state loses its topological protection, its zero-energy eigenvalue is always pinned to 0 due to SUSY isospectrality. The SP$_1$ lattice exhibits an exponentially decaying detuning on the left side of the lattice, while still resembling the SSH model toward the right part of the lattice (see Supplementary Fig. 3 for more details). The existence of both edge states and their different origins is experimentally verified, as discussed in the next section. Also, the stability of the edge states eigenvalues in the spectrum is numerically checked by introducing chiral disorder. Specifically, for the right edge state the deviation of the eigenvalue $\lambda_{N/2+1}$ tends to 0 as N increases, whereas for the left edge state, the deviation of the eigenvalue $\lambda_{N/2}$ is not affected by the size of the system and increases linearly with the amount of disorder (see Supplementary Note 2 and Supplementary Fig. 4 for more details). Note that by applying another DSUSY transformation removing λ_N, the inversion symmetry of the system is reestablished, and the topological protection of the left edge state can be restored. Furthermore, by removing high-order bulk states only from one side of the spectrum ($1<m<N/2$), the detuned region can be extended across the lattice to facilitate an enhanced coupling with the right edge state, which can even lose its topological protection due to the effect of the detuning. Finally, by applying multiple DSUSY transformations symmetrically, gaps can be carved out of the eigenvalue spectrum while preserving the topological protection of the zero-energy states. Here, in short, we have transformed a lattice supporting two topologically protected edge states to a phase-matched lattice supporting one topologically protected edge state, and one that has lost its topological protection and has become sensitive to the underlying disorder.

To summarize, the effects that DSUSY transformations induce on a system supporting two topologically protected zero-energy states are as follows: (i) the removal of a bulk state that is energetically far from the energy gap (m close to 1 or N), leads to a superpartner structure that supports one topological and one nontopological zero-energy states, (ii) the suppression of a bulk state that is energetically close to the energy gap (m close to $N/2$), destroys the topological protection of both zero-energy states of the superpartner structure, and (iii) the elimination of a zero-energy state ($m = N/2$ or $N/2 + 1$), produce a superpartner structure that supports one topologically protected zero-energy state. Finally, note that, if one removes bulk states of the system in a symmetric way, e.g., $m = 2$ and $m = N - 1$, both zero-energy states will hold their topological properties since chiral symmetry is preserved.

Experimental verification. In order to experimentally corroborate the previous theoretical findings, we employ the femtosecond direct laser-writing technology to inscribe waveguide arrays in fused silica (see "Methods," Supplementary Note 3 and Supplementary Fig. 3 for more details). Specifically, we exploit its ability to independently tune the coupling and detuning by changing the separation between waveguides and the inscription velocity, respectively[20]. To this aim, four different samples are fabricated: (i) the original SSH lattice described by $\mathcal{H}$, (ii) the superpartner $\mathrm{SP}_{N/2}$ lattice described by $\mathcal{H}_{N/2}^{(2)}$, (iii) the superpartner SP_1 lattice described by $\mathcal{H}_1^{(2)}$, and (iv) the SSH lattice weakly coupled to the SP_1 lattice. By launching single site excitations, light evolution of the different states along the different structures can be measured by means of waveguide fluorescence microscopy[35], and output pattern intensities can be extracted. Furthermore, by using a white light source, the wavelength of the injected light can be continuously tuned to evaluate the robustness and different origins of the edge states. Finally, by placing the SSH lattice in close proximity to the SP_1 lattice, evanescent coupling can be introduced between the topological edge state in the former, and the nontopological edge state in the latter. The contrast of the resulting sinusoidal intensity oscillations serves as direct indicator for any detuning between them, or the predicted absence thereof.

The first step to verify the previous theoretical predictions is to prove the existence of the edge and interface states. To this end, we excite the nontopological edge state, the topological edge state and the interface state and observe its evolution along the propagation direction, as displayed in Fig. 2g, h and i, respectively. First, the topological edge state is excited by injecting light into the Nth waveguide, as depicted in Fig. 2h. As a single site excitation is made, and the theoretically expected edge state is exponentially localized within the waveguides N, $N-2$, and $N-4$, as it is illustrated in Fig. 2e, other bulk states of the system are also excited and the injected intensity slightly spreads along the propagation direction. However, one can clearly observe how the output measured intensity distribution is in accordance with the predicted mode profile, showing the expected SSH edge state. Since the SSH lattice is symmetric, a mirrored propagation image would be obtained by injecting light into the first waveguide, exciting the left topological edge state. Note that the confinement of this edge state scales with the difference between the coupling coefficients c_1 and c_2. The next step is to demonstrate the presence of the interface state of the $\mathrm{SP}_{N/2}$ lattice. Although the expected theoretical interface state spans approximately five odd waveguides, as depicted in Fig. 2f, it is nevertheless populated by a single site excitation at the interface waveguide, as displayed in Fig. 2i. Moreover, as can be observed from the output intensity pattern, most of the light is localized at the interface waveguide itself. Note that, for the $\mathrm{SP}_{N/2}$ structure supporting only one edge state, light evolution and output intensity would resemble the previously obtained for the SSH lattice. The next stage is to prove the existence of the nontopological edge state of the SP_1 lattice, which has lost its topological protection due to the breaking of chiral symmetry of one part of the system. To do that, the first waveguide of the SP_1 lattice is excited, as it is displayed in Fig. 2g. While the localization is still visible, it may be noted that the output intensity distribution for the nontopological edge state does not have the staggered profile that characterizes the topological edge states. Instead, the nontopological edge state is mainly localized due to the high detuning in the first and second waveguides of the lattice, as it is depicted in Fig. 2d. Since this edge state is solely mediated by the detuning, it is less robust against perturbations than the topological state, as we numerically verified in Supplementary Note 2 and illustrated in Supplementary Fig. 4. Furthermore, a strong indication to this reasoning can be seen when we excite both edge states tuning the wavelength continuously from 500 to 720 nm. The experimental results obtained for the propagation of the different states are in good agreement with the tight-binding simulations, as shown in Supplementary Fig. 5.

To verify the different origin of the edge states of the SP_1 lattice, we excite both edges with different wavelengths and observe the output intensities after 10 cm of propagation, as can be seen in Fig. 3a, b. Experimentally, this is achieved by using a white light source combined with a narrow wavelength filter, as discussed in detail in "Methods" section. The first observation is that, despite their different topological natures, both edge states remain localized at the corresponding edges of the SP_1 lattice, represented in Fig. 3c. However, since the nontopological edge state is supported by the detuning, its degree of localization strongly decreases toward longer wavelengths (see Fig. 3a). This occurs because at longer wavelengths, the coupling substantially increases while the detuning decreases, thus the former becomes the dominant term and the confinement of the edge state is reduced. On the contrary, it gets fully localized into a single waveguide for shorter wavelengths, where the detuning is the dominant term. The confirmation that

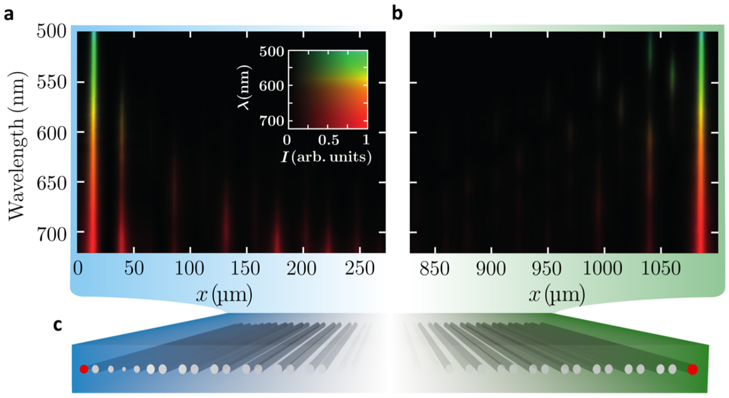

Fig. 3 Wavelength dependence of the edge states. Experimentally observed output intensities for different wavelengths (500 nm ≤ λ ≤ 720 nm) obtained by exciting (**a**) the nontopological and (**b**) the topological edge states of the SP_1 lattice, schematically represented in **c**. The red dots indicate the excited waveguides. The relation between the wavelength used and its intensity measured at the output is represented in the inset. The total length of the sample is $L = 10$ cm and the SP_1 lattice is composed of $N = 49$ waveguides.

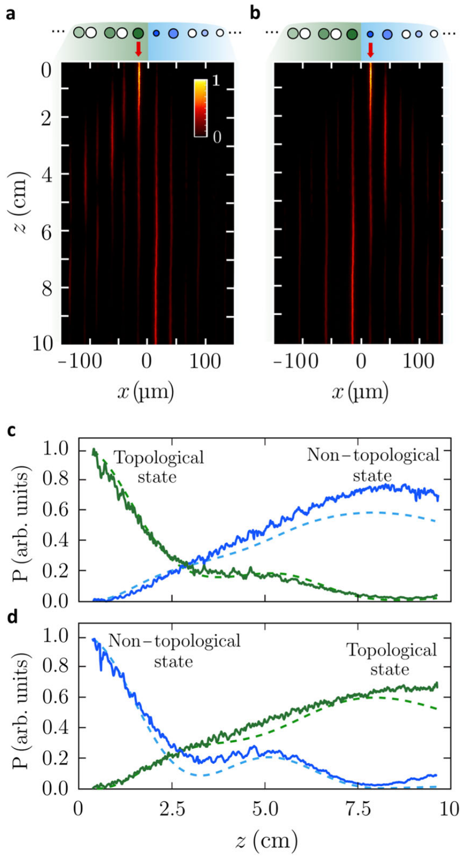

Fig. 4 Coupling of topological and nontopological edge states. Experimentally observed light evolution along the propagation direction when the waveguides supporting (**a**) the topological and (**b**) the nontopological edge states of the coupled structure, schematically displayed above, are excited. Power oscillations when the waveguide supporting (**c**) the topological (green line) and (**d**) the nontopological (blue line) edge state is excited. The *y* axis is the normalized power extratced from the fluorescence images in **a** and **b**. The *x* axis is the propagation distance in cm. The solid lines correspond to the experimental results while the dashed lines correspond to the tight-binding numerical simulations. The total length of the sample is $L = 10$ cm, the wavelength used to excite the waveguides is $\lambda = 633$ nm and the lattice is composed of $N = 99$ waveguides.

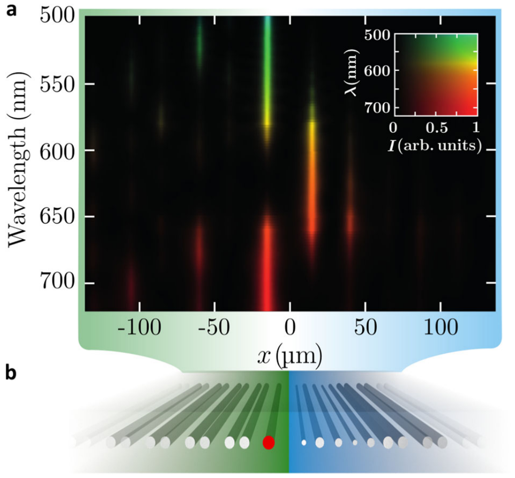

Fig. 5 Wavelength dependence of the coupled edge. a Experimentally observed output intensities for different wavelengths obtained by exciting the topological edge state of the coupled lattice, indicated with the red dot in **b**. **b** Schematic representation of the Su-Schrieffer-Heeger (SSH) lattice weakly coupled to the superpartner SP_1 lattice. The relation between the wavelength used and its intensity measured at the output is represented in the inset. The total length of the sample is $L = 10$ cm, the wavelength range used to excite the waveguides is $500\,\text{nm} \leq \lambda \leq 720$ nm and the lattice is composed of $N = 99$ waveguides.

the existence of this edge state is due to detuning is a strong indication for less robustness, since it does not have a topological origin. On the other hand, as shown in Fig. 3b, the topological state strictly maintains its characteristic staggered intensity structure across the investigated spectral range. Note that the slight delocalization at short wavelengths occurs as both couplings decrease and their absolute difference $|c_1 - c_2|$, which is related with the edge state confinement, becomes too small to strongly confine the state at the edge.

So far, we have proved the existence of the different topological states, as well as the different origin of the edge states of the SP_1 lattice. The last step is to verify that the nontopological edge state indeed does possess a zero-energy eigenvalue, as expected from SUSY transformation. To this aim, we weakly couple the nontopological edge state with the topological state, as displayed in Fig. 4a, b. Here, if the two states have the same energy, one would expect their coupling with a full exchange of power. On the contrary, if the two states have different energies, one would expect only a partial exchange of power. In Fig. 4a, b, we show the light evolution along the propagation direction when we excite either the waveguide supporting the topological state or the nontopological edge state, respectively. Moreover, in Fig. 4c, d, one can see how the topological edge state is coupled to the nontopological one and vice versa, transmitting around 70% of the injected power to the other edge state. Furthermore, one can observe how light is completely outcoupled from the excited waveguide, indicating that both edge states share the same propagation constant. Note that the intensity oscillations are in good agreement with the tight-binding simulations, shown by the dashed lines of Fig. 4c, d. The full oscillation pattern between edge states, both experimental and simulated, can be observed in Supplementary Fig. 5. Finally, we have checked that both edge states share the same energy independently of the wavelength by exciting them with a white light source, as it is displayed in Fig. 5. By increasing the wavelength, the coupling increases, leading to a reduced effective length scale of the chip. Looking at the output intensities, the full exchange of intensity between waveguides can be observed, confirming that both superpartner share the same eigenvalue spectrum.

Discussion

In our work, we studied the interplay between topological nontrivial systems and SUSY transformations. For this, we picked one of the most prominent models for illustrating topological physics, the SSH model, and demonstrated how topological phase transitions can be induced by DSUSY transformation. In particular, we showed that while this topological transition may suspend the topological protection of a state, it can readily be reestablished by applying another DSUSY transformation. Moreover, DSUSY transformations can also be used to annihilate topological states as well as to displace them from the edge to the inner part of the lattice. We exemplified this by transforming a lattice supporting two topological edge states to a lattice supporting (i) one topological edge or interface state, and (ii) one topological and one nontopological edge states. We experimentally demonstrated those theoretical findings implementing the superpartner structures using femtosecond laser written waveguides.

Clearly, SUSY techniques constitute a powerful tool to design structures with desirable topological properties, which can be extended to higher dimensions and chiral edge states in future works. Moreover, iterative DSUSY transformations could serve to remove any number of states from the system and reduce its overall size while preserving the desired part of the spectrum and the system's topological properties. Furthermore, inverse SUSY transformations[29,46] could be used to introduce zero-energy states, which will be topologically protected when these transformations are applied to systems having topology protecting symmetries. Finally, note that the method for topological state engineering presented here, based on applying DSUSY transformations, can be extended to any platform allowing independent control of the coupling and detuning of the sites, which are described by discrete Hamiltonians such as coupled cavities[36], ultra-cold atoms trapped in lattice potentials[37] or acoustic and mechanical systems[38].

Methods

Experimental design. Our experiments were conducted in femtosecond laser written photonic lattices, where the above-mentioned structures are fabricated and characterized as described below.

Fabrication of the structures. The waveguides were fabricated in 10 cm fused silica glass (Corning 7980) samples by using the femtosecond laser-writing method[35]. The laser system consists of a Coherent RegA 9000 amplifier seeded with a Coherent Vitara S Titanium:Sapphire laser with an energy of 250 nJ at 800 nm, 100 kHz repetition rate, and a pulse width of ~130 fs. By moving the sample with a high-precision positioning stage (Aerotech ALS 180) at speeds between 91 and 103 mm min^{-1}, the refractive index change at the focal point was around 7×10^{-4}. The created waveguides exhibit a mode field diameter of about 10.4 ×8 μm at 633 nm. The propagation losses and birefringence are estimated to be 0.2 dB cm^{-1} and 1×10^{-7}, respectively.

Characterization of the structures. In order to probe the propagation, the samples were illuminated with light from a Helium–Neon laser at 633 nm (Melles-Griot). The single lattice sites were excited with a 10× microscope objective (0.25 NA). In turn, the color centers that formed during the fabrication process, enable a direct observation of the propagation dynamics by using fluorescence microscopy[35]. The recorded images were post processed to reduce noise, distortions, and the influence of background light.

The intensities at the output facet at different wavelength were measured by using a white light source (NKT SuperK EXTREME) combined with a narrow wavelength filter (Photon ETC LLTF-SR-VIS-HP8). The light is then coupled into a single lattice site of the sample with a 10× microscope objective (0.25NA) and the resulting light at the output facet of the sample is imaged onto a CCD camera (BASLER Aviator) with another 10× microscope objective. The recorded images were post processed to reduce noise and subsequently integrated over a strip along the direction perpendicular to the lattice orientation for each wavelength. The resulting intensity distribution for the different wavelengths are then normalized to the maximum value to increase the visibility.

Data availability

All experimental data and any related experimental background information not mentioned in the text are available from the authors on reasonable request.

Received: 4 November 2019; Accepted: 19 February 2020;
Published online: 12 March 2020

References

1. Kane, G. & Shifman, M. *The Supersymmetric World: The Beginnings of the Theory* (World Scientific Publishing, Singapur, 2001).
2. Coleman, S. & Mandula, J. All possible symmetries of the S matrix. *Phys. Rev.* **159**, 1251–1256 (1967).
3. Haag, R., Lopuszanski, J. T. & Sohnius, M. All possible generators of supersymmetries of the S-matrix. *Nucl. Phys. B* **88**, 257–274 (1975).
4. Sourlas, N. Introduction to supersymmetry in condensed matter physics. *Phys. D.* **15**, 115–122 (1985).
5. Junker, G. *Supersymmetric Methods in Quantum and Statistical Physics* (Springer-Verlag, Heidelberg, 1996).
6. Cooper, F., Khare, A. & Sukhatme, U. Supersymmetry and quantum mechanics. *Phys. Rep.* **251**, 267–385 (1995).
7. Chumakov, S. M. & Wolf, K. B. Supersymmetry in Helmholtz optics. *Phys. Lett. A* **193**, 51–52 (1994).
8. Miri, M. A., Heinrich, M., El-Ganainy, R. & Christodoulides, D. N. Supersymmetric optical structures. *Phys. Rev. Lett.* **110**, 233902 (2013).
9. Dine, M. *Supersymmetry and String Theory: Beyond the Standard Model* (Cambridge University Press, Cambridge, 2007).
10. Grover, T., Sheng, D. N. & Vishwanath, A. Emergent space-time supersymmetry at the boundary of a topological phase. *Science* **344**, 280–283 (2014).
11. Qi, X. L. & Zhang, S.-C. Topological insulators and superconductors. *Rev. Mod. Phys.* **83**, 1057–1110 (2011).
12. Chiu, C.-K., Teo, J. C. Y., Schynder, A. P. & Ryu, S. Classification of topological quantum matter with symmetries. *Rev. Mod. Phys.* **88**, 035005 (2016).
13. Lu, L., Joannopoulos, J. D. & Soljačić, M. Topological photonics. *Nat. Photon.* **8**, 821–829 (2014).
14. Ozawa, T. et al. Topological photonics. *Rev. Mod. Phys.* **91**, 015006 (2019).
15. Kraus, Y. E., Lahini, Y., Ringel, Z., Verbin, M. & Zilberberg, O. Topological states and adiabatic pumping in quasicrystals. *Phys. Rev. Lett.* **109**, 106402 (2012).
16. Rechtsman, M. C. et al. Photonic Floquet topological insulators. *Nature* **496**, 196–200 (2013).
17. Khanikaev, A. B. et al. Photonic topological insulators. *Nat. Mater.* **12**, 233–239 (2013).
18. Hafezi, M., Mittal, S., Fan, J., Migdall, A. & Taylor, J. M. Imaging topological edge states in silicon photonics. *Nat. Photon.* **7**, 1001–1005 (2013).
19. Miri, M. A., Heinrich, M. & Christodoulides, D. N. Supersymmetry-generated complex optical potentials with real spectra. *Phys. Rev. A* **87**, 043819 (2013).
20. Heinrich, M. et al. Supersymmetric mode converters. *Nat. Commun.* **5**, 3698 (2014).
21. Principe, M., Castaldi, G., Consales, M., Cusano, A. & Galdi, V. Supersymmetry-inspired non-Hermitian optical couplers. *Sci. Rep.* **5**, 8568 (2015).
22. Queraltó, G., Ahufinger, V. & Mompart, J. Mode-division (de)multiplexing using adiabatic passage and supersymmetric waveguides. *Opt. Express* **25**, 27396–27404 (2017).
23. Macho, A., Llorente, R. & García-Meca, C. Supersymmetric transformations in optical fibers. *Phys. Rev. Appl.* **9**, 014024 (2018).
24. Queraltó, G., Ahufinger, V. & Mompart, J. Integrated optical devices based on adiabatic transitions between supersymmetric structures. *Opt. Express* **26**, 33797–33806 (2018).
25. Walasik, W., Midya, B., Feng, L. & Litchinitser, N. M. Supersymmetry-guided method for mode selection and optimization in coupled systems. *Opt. Lett.* **43**, 3758–3761 (2018).
26. Contreras-Astorga, A. & Jakubský, V. Photonic systems with two-dimensional landscapes of complex refractive index via time-dependent supersymmetry. *Phys. Rev. A* **99**, 053812 (2019).
27. Longhi, S. Supersymmetric transparent optical intersections. *Opt. Lett.* **40**, 463–466 (2015).
28. Heinrich, M. et al. Observation of supersymmetric scattering in photonic lattices. *Opt. Lett.* **39**, 6130–6133 (2014).
29. Miri, M. A., Heinrich, M. & Christodoulides, D. N. SUSY-inspired one-dimensional transformation optics. *Optica* **1**, 89–95 (2014).
30. García-Meca, C., Ortiz, A. M. & Sáez, R. L. Supersymmetry in the time domain and its applications in optics. *Nat. Commun.* **11**, 813 (2020).
31. Hokmabadi, M. P., Nye, N. S., el-Ganainy, R., Christodoulides, D. N. & Khajavikhan, M. Supersymmetric laser arrays. *Science* **363**, 623–626 (2019).
32. Midya, B. et al. Supersymmetric microring laser arrays. *Photonics Res.* **7**, 363–367 (2019).
33. Yu, S., Piao, X., Hong, J. & Park, N. Bloch-like waves in random-walk potentials based on supersymmetry. *Nat. Commun.* **6**, 8269 (2015).
34. Midya, B., Walasik, W., Litchinitser, N. M. & Feng, L. Supercharge optical arrays. *Opt. Lett.* **43**, 4927–4930 (2018).
35. Szameit, A. & Nolte, S. Discrete optics in femtosecond-laser-written photonic structures. *J. Phys. B* **43**, 163001 (2010).
36. Ding, J. & Miri, M. A. Mode discrimination in dissipatively coupled laser arrays. *Opt. Lett.* **44**, 5021 (2019).
37. Atala, M. et al. Direct measurement of the Zak phase in topological Bloch bands. *Nat. Phys.* **9**, 795 (2013).

38. Ma, G., Xiao, M. & Chan, C. T. Topological phases in acoustic and mechanical systems. *Nat. Rev. Phys.* **1**, 281–294 (2019).
39. Barkhofen, S., Lorz, L., Nitsche, T., Silberhorn, C. & Schomerus, H. Supersymmetric polarization anomaly in photonic discrete-time quantum walks. *Phys. Rev. Lett.* **121**, 260501 (2018).
40. Su, W. P., Schrieffer, J. R. & Heeger, A. J. Solitons in polyacetylene. *Phys. Rev. Lett.* **42**, 1698–1701 (1979).
41. Jones, A. L. Coupling of optical fibers and scattering in fibers. *J. Opt. Soc. Am.* **55**, 261–271 (1965).
42. Hogben, L. *Handbook of Linear Algebra* (Chapman & Hall/CRC, New York, 2006).
43. Zak, J. Berry's phase for energy bands in solids. *Phys. Rev. Lett.* **62**, 2747 (1988).
44. Asbóth, J. K., Oroszlány, L. & Pályi, A. *A Short Course on Topological Insulators* (Springer International Publishing, Cham, 2016).
45. Weimann, S. et al. Topologically protected bound states in photonic PT-symmetric crystals. *Nat. Mater.* **16**, 433438 (2017).
46. Longhi, S. Invisibility in non-Hermitian tight-binding lattice. *Phys. Rev. A* **82**, 32111 (2010).

Acknowledgements

G.Q., J.M., and V.A. acknowledge financial support by Spanish Ministry of Science, Innovation and Universities MICINN (Contract No. FIS2017-86530-P) and Generalitat de Catalunya (Contract No. SGR2017-1646). G.Q. also acknowledges the financial support of German Academic Exchange Service (DAAD). A.S. thanks the Deutsche Forschungsgemeinschaft for funding this research (grants BL 574/13-1, SZ 276/15-1, and SZ 276/20-1). The authors would like to thank C. Otto for preparing the highly quality-fused silica samples used in all our experiments.

Author contributions

G.Q., M.K., and M.H. developed the theory. M.K., L.M., and G.Q. fabricated the samples and performed the measurements. M.H., J.M., V.A., and A.S. supervised the project. All authors discussed the results and co-wrote the paper.

Competing interests

The authors declare no competing interests.

Additional information

Supplementary information is available for this paper at https://doi.org/10.1038/s42005-020-0316-4.

Correspondence and requests for materials should be addressed to A.S.

Reprints and permission information is available at http://www.nature.com/reprints

Publisher's note Springer Nature remains neutral with regard to jurisdictional claims in published maps and institutional affiliations.

Open Access This article is licensed under a Creative Commons Attribution 4.0 International License, which permits use, sharing, adaptation, distribution and reproduction in any medium or format, as long as you give appropriate credit to the original author(s) and the source, provide a link to the Creative Commons license, and indicate if changes were made. The images or other third party material in this article are included in the article's Creative Commons license, unless indicated otherwise in a credit line to the material. If material is not included in the article's Creative Commons license and your intended use is not permitted by statutory regulation or exceeds the permitted use, you will need to obtain permission directly from the copyright holder. To view a copy of this license, visit http://creativecommons.org/licenses/by/4.0/.

© The Author(s) 2020

Supplementary Figures

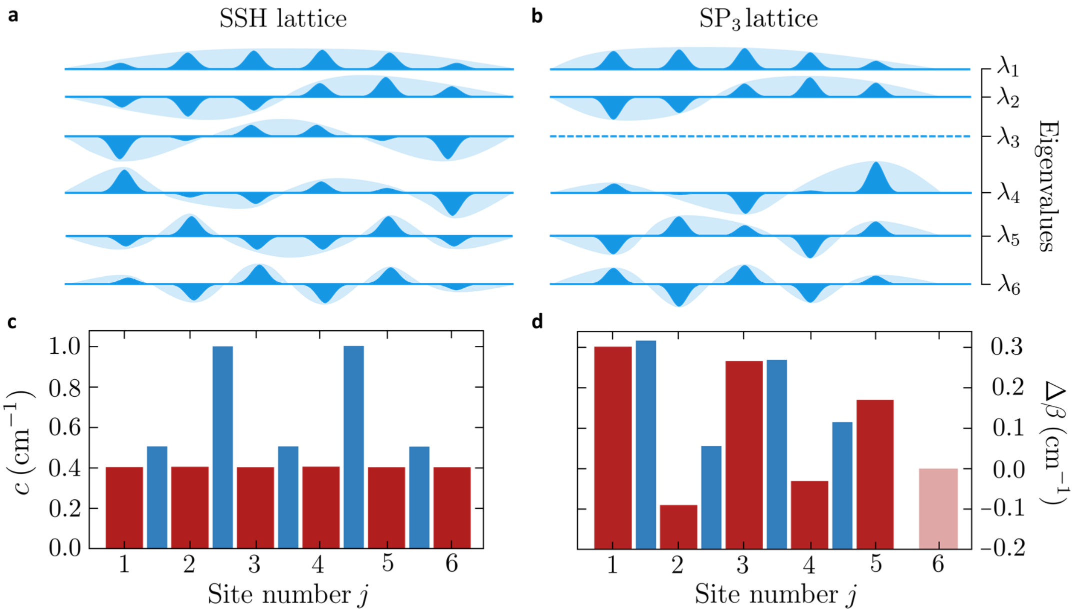

Supplementary Figure 1. Discrete optical supersymmetry. Eigenvalue spectrum and eigenstate profiles corresponding to **a** the Su-Schrieffer-Heeger (SSH) lattice and **b** the superpartner SP$_3$ lattice, obtained by removing the eigenvalue λ_3 using discrete supersymmetric transformations. Discrete representation in terms of the waveguide's detuning $\Delta\beta$ (red bars) and couplings c (blue bars) of the **c** SSH and **d** SP$_3$ lattices. The SSH lattice is composed of $N = 6$ waveguides, $c_1 = 0.5$ cm^{-1} and $c_2 = 1.0$ cm^{-1}.

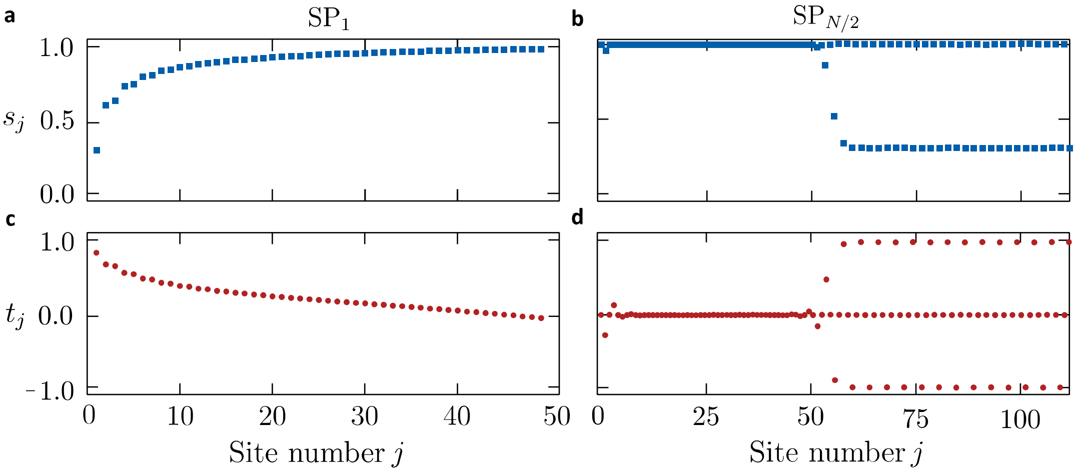

Supplementary Figure 2. Givens rotation method. Representation of s_j and t_j of the Givens rotation matrices $g_j = t_j\sigma_0 + is_j\sigma_y$, where σ_0 is the two-dimensional identity matrix, σ_y the y-Pauli matrix and j the site number within the lattice. **a** and **b** show the s_j elements associated with the superpartner SP$_1$ lattice and the superpartner SP$_{N/2}$ lattice, respectively. **c** and **d** display the t_j elements associated with the SP$_1$ lattice and SP$_{N/2}$ lattice, respectively. The original Su-Schrieffer-Heeger lattice used to construct the SP$_1$ (SP$_{N/2}$) lattice is composed of $N = 50$ ($N = 110$) waveguides, $c_1 = 0.5$ cm^{-1} and $c_2 = 1.0$ cm^{-1} ($c_2 = 1.8$ cm^{-1}).

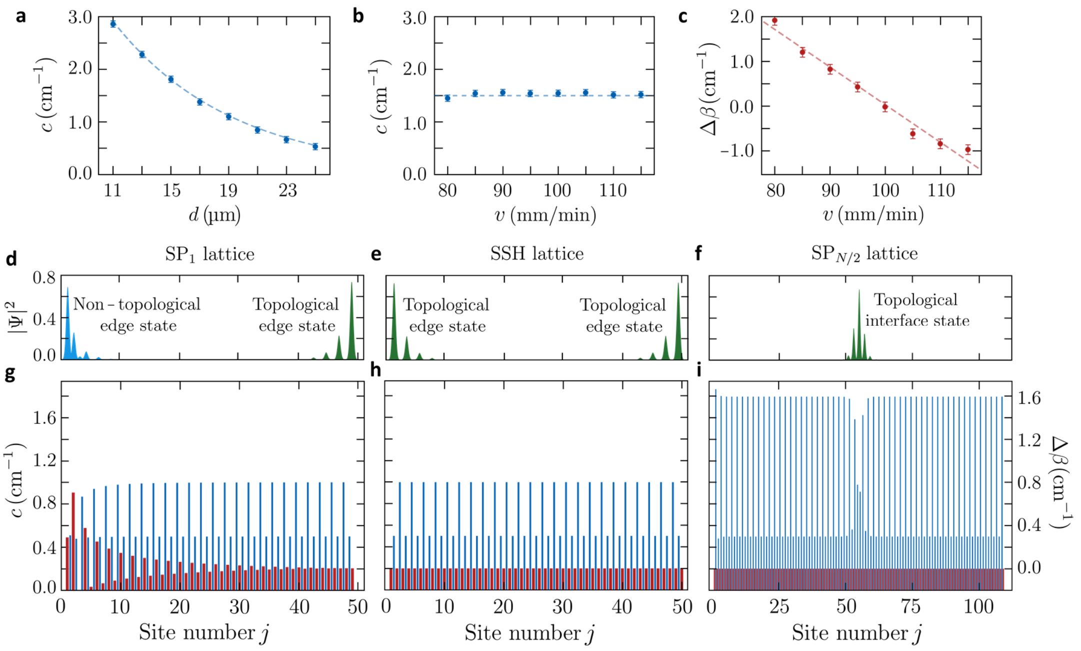

Supplementary Figure 3. Experimental implementation of supersymmetric lattices. Coupling coefficient c dependence with respect to **a** the waveguide separation d, calibrated using pairs of evanescently coupled waveguides with different separation, and, **b** the writing speed v, calibrated using pairs of evanescently coupled waveguides written with different velocities. **c** Detuning $\Delta\beta$ dependence with respect to the writing velocity. The dots correspond to the experimentally obtained values while the dashed lines are **a** the exponential and **b-c** the linear fits. The error bars in **a-c** indicate the experimental error associated to the couplings and detunings. Eigenstate amplitudes of the edge and interface states for **d** the superpartner SP$_1$ lattice, **e** the Su-Schrieffer-Heeger (SSH) lattice and, **f** the superpartner SP$_{N/2}$ lattice. Discrete representation in terms of the detunings $\Delta\beta$ (red bars) and couplings c (blue bars) of the **g** SP$_1$, **h** SSH, and **i** SP$_{N/2}$ lattices. The original SSH lattice used to construct the SP$_1$ (SP$_{N/2}$) lattice is composed of $N = 50$ ($N = 110$) waveguides, $c_1 = 0.5\ \mathrm{cm}^{-1}$ and $c_2 = 1.0\ \mathrm{cm}^{-1}$ ($c_2 = 1.8\ \mathrm{cm}^{-1}$).

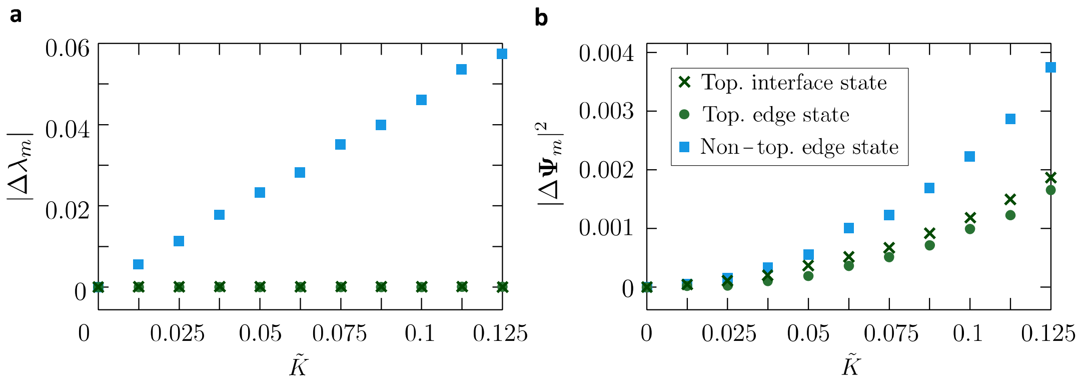

Supplementary Figure 4. Robustness against chiral disorder. Deviation of the **a** eigenvalue λ_s and **b** eigenstate shape $\mathbf{\Psi}_s$ with respect to the ones of the original lattice ($K = 0$) when chiral disorder is introduced into the system, for: the non-topological edge state $s = 25$ (squares), the topological edge state $s = 26$ (circles) and the topological interface state $s = 56$ (crosses). The introduced chiral disorder is of the form $\Delta c = \xi_q \widetilde{K}$, where $\widetilde{K} = \xi_q K|c_1 - c_2|/2$ being K the disorder strength, $|c_1 - c_2|$ the dimerization, and $-1 \leq \xi_q \leq 1$ a random number that affects the couplings of unit cell q. The total deviation is averaged over 5000 different simulations with different random disorder. All the simulations were carried out using the lattices of Supplementary Figure 3 **g-i**.

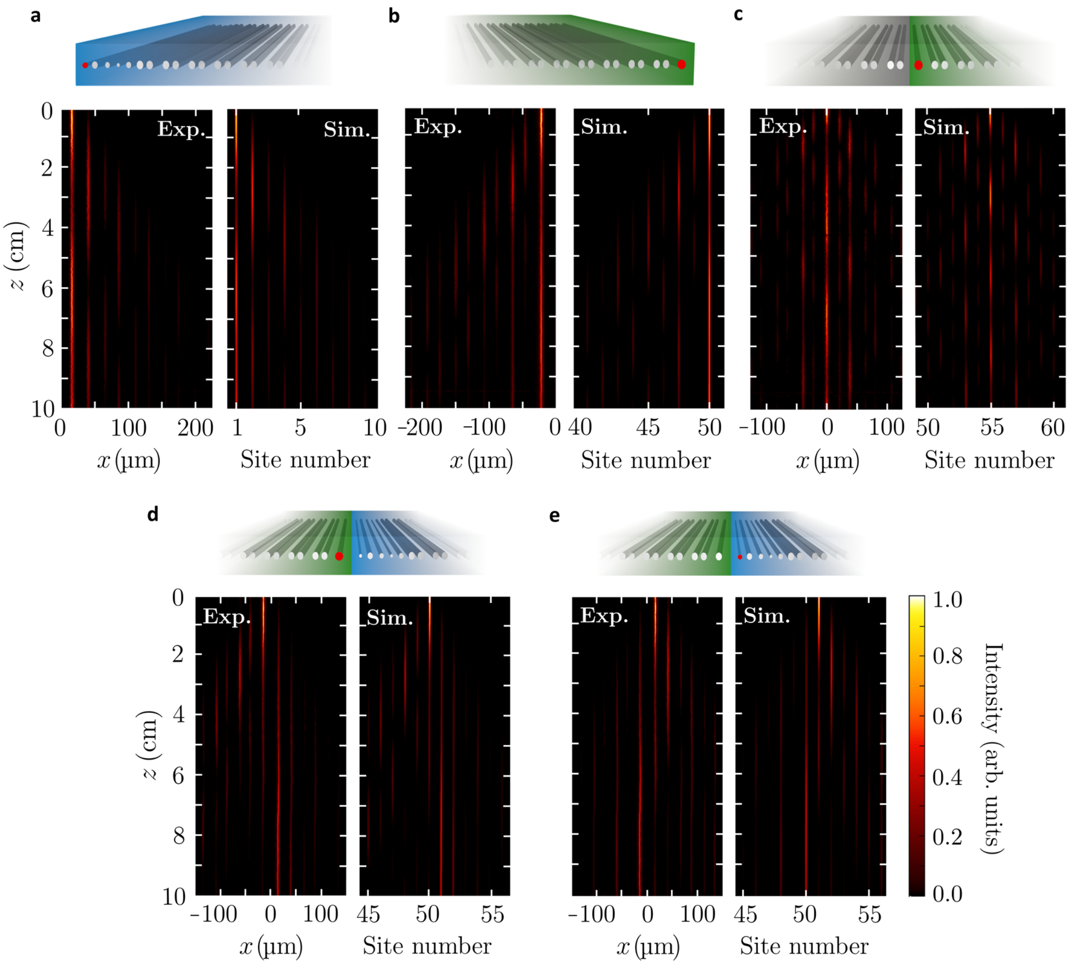

Supplementary Figure 5. Experimental results versus numerical simulations. Intensity distribution, extracted by means of fluorescence microscopy (Exp.), is plotted together with tight-binding binding simulations (Sim.), for **a** the superpartner SP_1 lattice, **b** the Su-Schrieffer-Heeger (SSH) lattice, **c** the superpartner $SP_{N/2}$ lattice, and **d-e** the coupled SSH and SP_1 lattices. The corresponding lattices are shown schematically above the propagation pictures. The red dots of each structure indicate the excited waveguide, corresponding to the **a** and **e** non-topological edge state, **b** and **d** topological edge state, and **c** topological interface state. All the simulations have a correction of $\Delta c = -0.05\text{cm}^{-1}$ with respect to the lattices represented in Supplementary Figure 3 **g-i**, to adjust the results to the real experimental values. The results show an overall good agreement between the experiments and the simulations, confirming the validity of the theoretical description. Only a quantitative discrepancy in **c** due to locally increased coupling caused by tightly spaced waveguides at the interface, can be observed. However, the qualitative behavior is well reproduced.

Supplementary Notes

Supplementary Note 1: Discrete supersymmetric transformations

In the quantum-mechanical formalism [1], Supersymmetry (SUSY) connects an operator $\mathcal{H}^{(1)} = A^{\dagger}A$, which can be decomposed in terms of an operator A and its Hermitian adjoint $A^{\dagger}$, with $\mathcal{H}^{(2)} = AA^{\dagger}$. From the eigenvalue equation

$$\mathcal{H}^{(1)}\Psi_s^{(1)} = \lambda_s^{(1)}\Psi_s^{(1)}, \tag{1}$$

where $\lambda_s^{(1)}$ is the eigenvalue and $\Psi_s^{(1)}$ is the eigenstate of state s, one can derive

$$A\mathcal{H}^{(1)}\Psi_s^{(1)} = A\left(A^{\dagger}A\right)\Psi_s^{(1)} = \mathcal{H}^{(2)}\left(A\Psi_s^{(1)}\right) = \lambda_s^{(1)}\left(A\Psi_s^{(1)}\right), \tag{2}$$

obtaining that $A\Psi_s^{(1)}$ is an eigenstate of $\mathcal{H}^{(2)}$ with eigenvalue $\lambda_s^{(1)}$, establishing SUSY isospectrality. For unbroken SUSY, the ground state of $\mathcal{H}^{(1)}$ is annihilated and removed from the spectrum of $\mathcal{H}^{(2)}$. Discrete SUSY (DSUSY) transformations can be applied to discrete systems using symmetric and asymmetric methods such as the Cholesky algorithm and the *QR* factorization, respectively [2]. In general, a *QR* factorization of a matrix $B \in \mathbb{R}^{m\times n} (m \geq n)$ is a decomposition into $B = QR$, where $Q \in \mathbb{R}^{m\times m}$ is an orthogonal matrix and $R \in \mathbb{R}^{m\times n}$ is an upper triangular matrix [2]. Considering a discrete Hamiltonian $\mathcal{H}$, describing a system of N identical evanescently-coupled waveguides with alternating coupling strengths c_1 and c_2:

$$\mathcal{H} = \begin{pmatrix} 0 & c_1 & 0 & \cdots & 0 \\ c_1 & 0 & c_2 & \ddots & \vdots \\ 0 & c_2 & \ddots & \ddots & 0 \\ \vdots & \ddots & \ddots & \ddots & c_1 \\ 0 & \cdots & 0 & c_1 & 0 \end{pmatrix}, \tag{3}$$

the superpartner Hamiltonians obtained using the *QR* factorizations are

$$\mathcal{H}_m^{(1)} = \mathcal{H} - \lambda_m I = QR \text{ and } \mathcal{H}_m^{(2)} = RQ, \tag{4}$$

where $\mathcal{H}_m^{(2)}$ represents a lattice with $N - 1$ waveguides and the same eigenvalues as $\mathcal{H}_m^{(1)}$, except for λ_m supported by the single waveguide that is uncoupled from the system.

To illustrate DSUSY transformations we consider a one-dimensional array of $N = 6$ weakly-coupled waveguides supporting six states, as it is displayed in Supplementary Figure 1a we eliminate λ_3 from the eigenvalue spectrum of $\mathcal{H}_m^{(2)}$, as it is illustrated in Supplementary Figure 1b. Thus, starting with the Su-Schrieffer-Heeger (SSH) model, see Supplementary Figure 1c, we synthetize the superpartner structure SP_3 represented in Supplementary Figure 1d. In particular, to perform the *QR* factorization, we use the Givens Rotation method that is numerically stable, thus, suitable for application on large lattices [3]. This method is based on applying rotations

$G_j = g_j \otimes I$, where I is the $N \times N$ identity matrix, to the tri-diagonal Hamiltonian $\mathcal{H}_m^{(1)}$, forming

$$R = \prod_{j=1}^{N-1} G_j \, \mathcal{H}_m^{(1)} \text{ and } Q = \prod_{j=1}^{N-1} G_j^T \, . \tag{5}$$

The rotations $g_j \in \mathbb{R}^{2\times 2}$ are applied to each element $a_{j,j}$ of $\mathcal{H}_m^{(1)}$ introducing zeroes at the sub-diagonal elements $a_{j+1,j}$:

$$g_j \begin{pmatrix} a_{j,j} \\ a_{j+1,1} \end{pmatrix} = \begin{pmatrix} t_j & s_j \\ -s_j & t_j \end{pmatrix} \begin{pmatrix} a_{j,j} \\ a_{j+1,1} \end{pmatrix} = \begin{pmatrix} r_j \\ 0 \end{pmatrix}, \tag{6}$$

where $t_j = a_{j,j}/r_j$, $s_j = a_{j+1,j}/r_j$ and $r_j = \left[a_{j,j}^2 + a_{j+1,j}^2\right]^{1/2}$, which can be rewritten in terms of the corresponding Pauli matrices as

$$g_j = t_j \sigma_0 + i s_j \sigma_y. \tag{7}$$

Recall that the Pauli matrices are

$$\sigma_0 = \begin{pmatrix} 1 & 0 \\ 0 & 1 \end{pmatrix}, \quad \sigma_x = \begin{pmatrix} 0 & 1 \\ 1 & 0 \end{pmatrix}, \quad \sigma_y = \begin{pmatrix} 0 & -i \\ i & 0 \end{pmatrix} \text{ and } \sigma_z = \begin{pmatrix} 1 & 0 \\ 0 & -1 \end{pmatrix}. \tag{8}$$

These rotation functions g_j can be related to the topological transitions. For the SP$_1$ lattice represented in Supplementary Figure 3g, we can observe in Supplementary Figures 2a and c, how $g_j \to i\sigma_y$ towards the right part of the lattice, where the superpartner still resembles the SSH model. Besides, $g_j \sim t_j \sigma_0$ is the dominant term throughout the left side of the lattice, inducing a small deviation in the couplings with respect to the original SSH lattice and introducing an exponentially decaying detuning. For the SP$_{N/2}$ lattice represented in Supplementary Figure 3i supporting an interface state, we can observe in Supplementary Figures 2b and d, how $s_j \to 1$ and $t_j \to 0$ for $j < j_{\text{interface}}$. Thus, $g_j \to i\sigma_y$, interchanging the couplings c_1 and c_2 of the original SSH lattice. Around $j_{\text{interface}}$, there is a transition to a more complex behavior $g_{j,\text{even}} \to i\sigma_y$, $g_{j,\text{odd}} \to \pm\sigma_0 + i\sigma_y c_2/c_1$, which leads to a recovering of the original SSH configuration. Note that, a degenerate solution exists for the SP$_{N/2}$ lattice resembling the SSH model with interchanged couplings and $N-1$ waveguides, with $g_j \to i\sigma_y$ constituting a topological phase transition.

Supplementary Note 2: robustness of the topological states

The Hamiltonian $\mathcal{H}$ of the Su-Schrieffer-Heeger (SSH) model, given by Eq. (3), is a $N \times N$ tridiagonal matrix with zero-valued diagonal elements ($\Delta\beta = 0$) and off-diagonal elements alternating between c_1 and c_2 ($c_1 < c_2$). This system supports two topologically protected zero-energy edge states, which appear at the edge of a region with non-zero Zak phase $\mathcal{Z}$:

$$\mathcal{Z} = \mathrm{i} \oint u^*(k) \partial_k u(k) dk, \tag{9}$$

where k is the Bloch wavenumber within the first Brillouin zone and $u(k)$ the corresponding eigenvector in k-space [4]. The topological protection of the zero-energy edge states is closely related with the existence and breaking of the symmetries of the system. In particular, the SSH model can be characterized with two main symmetries (i) the Chiral symmetry and, (ii) the Particle Hole symmetry (PHS). On the one hand, the Chiral or symmetry, is defined by the unitary and Hermitian operator Γ, which anti-commutes with the Hamiltonian $\mathcal{H}$ i.e., $\{\mathcal{H}, \Gamma\} = 0$. On the other hand, the PHS is defined by an anti-unitary operator P, which also anti-commutes with the Hamiltonian $\mathcal{H}$, having $\{\mathcal{H}, \mathrm{P}\} = 0$. The application of these operators to the Hamiltonian leads to

$$\Gamma \mathcal{H} \Gamma^\dagger = -\mathcal{H}, \quad P \mathcal{H} P^{-1} = -\mathcal{H}. \tag{10}$$

Note that, since chiral and PHS exist, time reversal symmetry also exists for this model, hence, $\Gamma P \mathcal{H} P^{-1} \Gamma^\dagger = \mathcal{H}$. Moreover, the chiral operator Γ can be expressed in terms of the z Pauli matrix as $\Gamma = \sigma_z \oplus \sigma_z \oplus \cdots \oplus \sigma_z$, which is an $N \times N$ matrix of the form

$$\Gamma = \begin{pmatrix} 1 & 0 & 0 & \cdots & 0 \\ 0 & -1 & 0 & \ddots & \vdots \\ 0 & 0 & \ddots & \ddots & 0 \\ \vdots & \ddots & \ddots & 1 & 0 \\ 0 & \cdots & 0 & 0 & -1 \end{pmatrix}. \tag{11}$$

Besides, the chiral operator acts locally within each unit cell and follows the same algebra than σ_z, satisfying $\Gamma^\dagger \Gamma = \Gamma^2 = 1$. To numerically prove the topological protection of the states, we introduce chiral disorder of the form [5]:

$$\tilde{c}_1^q = c_1 + \Delta c, \;\; \tilde{c}_2^q = c_2 - \Delta c, \tag{12}$$

where $\Delta c = \xi_q K |c_1 - c_2|/2$. The disorder in quantified in terms of the disorder strength K, the dimerization $|c_1 - c_2|$, and a random number $-1 \leq \xi_q \leq 1$ that affects the couplings of each unit cell q, formed by two sites. To prove the robustness, we compute the deviation of the eigenvalues and eigenstates with respect to the case without disorder ($K = 0$):

$$|\Delta\lambda_s| = |\lambda_s - \lambda_s(K = 0)| \text{ and } |\Delta\mathbf{\Psi}_s|^2 = |\mathbf{\Psi}_s - \mathbf{\Psi}_s(K = 0)|. \tag{13}$$

Due to their symmetries, the zero-energy eigenvalues, corresponding to the topological edge states, should be robust against this kind of disorder, while the other states should exhibit an eigenvalue deviation.

For the SP$_1$ lattice of Supplementary Figure 3g, by introducing up to 25% of disorder with respect of $|c_1 - c_2|$, we can observe in Supplementary Figure 4a how there is no deviation of the eigenvalue λ_{26} corresponding to the topological edge state. On the other hand, if we take a look at the deviation of the eigenvalue λ_{25} corresponding to the non-topological edge state, we can confirm that the state is not topologically protected and the deviation of its eigenvalue with respect to the non-disordered case increases linearly with the amount of disorder. Note that for the topological edge state the deviation of the eigenvalue λ_{26} reduces as N increases, whereas the eigenvalue deviation of the non-topological edge state $\Delta\lambda_{25}$ is not affected by the size of the system. Regarding the changes in the eigenstate shapes, shown in Supplementary Figure 4b, we can observe how the non-topological edge state suffers more deviations than the topological one. In both cases, the change in the eigenstate shapes are small, and the states remain localized at the corresponding edges of the SP$_1$ lattice.

For the SP$_{N/2}$ lattice of Supplementary Figure 3i, it is numerically shown that by introducing up to 25% of disorder with respect of $|c_1 - c_2|$, there is no deviation of the zero-energy eigenvalue λ_{56} corresponding to the topological interface state, as it is shown in Supplementary Figure 4a. In this case, although the eigenstate shape is more perturbed than for the topological edges, it still remains localized at the interface. The higher deviation in this case may be produced due to the fact that the interface state spreads along more waveguides than the edge states. Thus, disorder introduced to the system has more impact on the modification of its shape, while it does not affect its eigenvalue which is protected by the symmetries of the system. Moreover, if any other kind of disorder not preserving the chiral symmetry of the system is introduced, the topological states are no longer topologically protected and their zero-energy eigenvalues suffer deviations of the same order than the non-topological states.

Supplementary Note 3: design of the supersymmetric structures

The experimental implementation of the SUSY structures with femtosecond laser written waveguides is based on the similarity between the Schrödinger and the Helmholtz equations [6]. On the one hand, the Schrödinger equation of quantum mechanics is given by:

$$\mathrm{i}\hbar\frac{\partial}{\partial t}\Psi(x,y,t) = -\frac{\hbar^2}{2m}\nabla^2\Psi(x,y,t) + V(x,y,t)\Psi(x,y,t), \tag{14}$$

where $\Psi(x,y,t)$ is the wavefunction, $\hbar = h/2\pi$ is the reduced Planck constant and $V(x,y,t)$ is the potential. On the other hand, the paraxial Helmholtz equation is:

$$\mathrm{i}ƛ\frac{\partial}{\partial z}\mathrm{E}(x,y,z) = -\frac{ƛ^2}{2n_0}\nabla^2\mathrm{E}(x,y,z) - \Delta n(x,y,z)\mathrm{E}(x,y,z), \tag{15}$$

In turn, wavefunction $\Psi(x,y,t)$ in the Schrödinger equation is replaced by the electric field amplitude $\mathrm{E}(x,y,z)$ in the Helmholtz equation, the potential $V(x,y,t)$ is replaced by the refractive index profile $-\Delta n(x,y,z)$, the propagation in time is replaced by the spatial coordinate z, which can be monitored by means of fluorescence microscopy, and the reduced Planck constant is replaced by the reduced wavelength $ƛ = \lambda/2\pi$. In the tight-binding approximation, Eq. (14) furthermore simplifies to:

$$\mathrm{i}\frac{\partial}{\partial z}\psi_j = \beta_j\psi_j + c_{j,j+1}\psi_{j+1} + c_{j,j-1}\psi_{j-1}, \tag{16}$$

where ψ_j is the field amplitude at site j, β_j the propagation constant and $c_{j,j\pm1}$the coupling between adjacent waveguides.

For the implementation of the SUSY structures, both, the coupling as well as the detuning need to be tuned individually. The coupling (c) is changed by using different distances (d) between waveguides, while the detuning $(\Delta\beta)$ is changed by using different writing velocities (v). The relation between distance and coupling (writing speed and detuning) is retrieved from directional couplers, by measuring the coupling length and the intensity contrast. The results are plotted in Supplementary Figure 3 a-c. The coupling is well fitted by an exponential function of the distance between waveguides, while the detuning depends linearly on the writing speed. The exponential and linear fits are:

$$c(d) = k_1\exp(-k_2 d)\,,\quad k_1 = 10.93\ \mathrm{cm}^{-1},\quad k_2 = 0.121\ \mathrm{\mu m}^{-1},$$

$$\Delta\beta(v) = k_3 v + k_4,\quad k_3 = -0.8327\ \mathrm{min\,cm}^{-1}\,,\quad k_4 = 8.376\ \mathrm{cm}^{-1}.$$

Note that the coupling is virtually unaffected by changes in the writing speed, as shown in Supplementary Figure 3b. This allows for an independent tuning of both parameters for a wide parameter range. The couplings and detunings used in the fabrication process are displayed in

Supplementary Figure 3g-i, and the edge and interface eigenstates supported by those lattices are displayed in Supplementary Figure 3 d-f. Note that, the SP_1 ($\text{SP}_{N/2}$) structure is obtained taking an original SSH lattice with $c_1 = 0.5\ \text{cm}^{-1}$ and $c_2 = 1.0\ \text{cm}^{-1}$ ($c_2 = 1.8\ \text{cm}^{-1}$). Although a bigger contrast between the couplings would be better to have more localized edge states, for the SP_1 lattice we had the experimental restriction to adjust the detuning below 2 cm^{-1} in order to guarantee that the coupling stays constant when changing the detuning. This could not be fulfilled when using higher couplings for the SSH lattice.

Supplementary references

1. Cooper, F., Khare, A. & Sukhatme, U. Supersymmetry and quantum mechanics. *Phys. Rep.* **251**, 267-385 (1995).
2. Hogben, L. *Handbook of Linear Algebra* (Chapman & Hall/CRC, New York, 2006).
3. Miri, M. A., Heinrich, M., El-Ganainy, R. & Christodoulides, D. N. Supersymmetric optical structures. *Phys. Rev. Lett.* **110**, 233902 (2013).
4. Zak, J. Berry's phase for energy bands in solids. *Phys. Rev. Lett.* **62**, 2747 (1988).
5. Weimann, S. et al. Topologically protected bound states in photonic PT-symmetric crystals. *Nat. Mater.* **16**, 433438 (2017).
6. Szameit, A. & Nolte, S. Discrete optics in femtosecond-laser-written photonic structures. *J. Phys. B* **43**, 163001 (2010).

8.3 A square-root topological insulator with non-quantized indices realized with photonic Aharonov-Bohm cages

M. Kremer, I. Petrides, E. Meyer, M. Heinrich, O. Zilberberg, and A. Szameit *A square-root topological insulator with non-quantized indices realized with photonic Aharonov-Bohm cages*, Nature Communications **11**, 907 (2020).
DOI: `https://doi.org/10.1038/s41467-020-14692-4`

Author Contributions:

Mark Kremer	project idea, conceptual design, calculation of band structures and topological invariants, disorder simulations, sample design, experimental determination of the sample parameters, sample fabrication, fluorescence measurements, data acquisition, data evaluation, figure art, preparation of initial manuscript draft
Ioannis Petrides	conceptual design, development of the theoretical framework for the square-root operation, calculation of topological invariants, figure art, preparation of initial manuscript draft
Eric Meyer	preparation of the manuscript, data evaluation
Matthias Heinrich	preparation of the manuscript
Oded Zilberberg	preparation of the manuscript, supervision
Alexander Szameit	preparation of the manuscript, supervision

Note: The shared co-first authorship of Ioannis Petrides and Mark Kremer is based on the distinct contributions of both authors. The square-root formalism has been developed by Ioannis Petrides, while the theoretical disorder analysis and the experimental realisation is mainly the work of Mark Kremer.

nature COMMUNICATIONS

ARTICLE

https://doi.org/10.1038/s41467-020-14692-4 OPEN

A square-root topological insulator with non-quantized indices realized with photonic Aharonov-Bohm cages

Mark Kremer[1,3], Ioannis Petrides[2,3], Eric Meyer[1], Matthias Heinrich[1], Oded Zilberberg[2✉] & Alexander Szameit[1✉]

Topological Insulators are a novel state of matter where spectral bands are characterized by quantized topological invariants. This unique quantized nonlocal property commonly manifests through exotic bulk phenomena and corresponding robust boundary effects. In our work we study a system where the spectral bands are associated with non-quantized indices, but nevertheless possess robust boundary states. We present a theoretical analysis, where we show that the square of the Hamiltonian exhibits quantized indices. The findings are experimentally demonstrated by using photonic Aharonov-Bohm cages.

---

[1] Institut für Physik, Universität Rostock, Albert-Einstein-Straße 23, 18059 Rostock, Germany. [2] Institut für Theoretische Physik, ETH Zürich, Wolfgang-Pauli-Straße 27, 8093 Zürich, Switzerland. [3]These authors contributed equally: Mark Kremer, Ioannis Petrides. ✉email: odedz@phys.ethz.ch; alexander.szameit@uni-rostock.de

The Klein–Gordon Hamiltoninan is a famous example, where taking its square-root lead to fundamentally new insides: with the help of the resulting Dirac Hamiltonian, describing a massive spin-1/2 fermionic particle, it was possible to explain the fine-structure spectra of atoms and the anomalous Zeeman effect[1]. Interestingly, as it emerged much later, the square-root procedure has proven to be useful also in other fields: it explains the robust boundary modes of mechanical lattices and connects it to the topological band theory of electronic systems[2], it relates bosons and fermions via supersymmetric transformations[3], and, in addition, it generates rich models from nontrivial topological insulators (TIs)[4].

TIs—a new phase of matter—have to date seen a variety of manifestations with prominent examples including the two dimensional (2D)[5] and four dimensional (4D) quantum Hall effects[6], one dimensional (1D) topological superconductors[7], 2D[8] and three dimensional (3D) TIs[9], crystalline and quasi-crystalline TIs[10,11], and higher-order TIs[12]. All available realizations of TIs, however, share a common feature: their spectral bands are attributed a nonlocal topological index that is quantized[13–15]. Hence, whereas different realizations of TIs can vary locally, as long as their topological characterization persists, they will exhibit the same topological phenomena. In other words, the quantization of topological indices lies at the foundation of the characteristic robustness of bulk responses and associated boundary phenomena in TIs.

In our work, we use a square-root procedure to provide a topological framework of a 1D TI with non-quantized bulk indices. This explains the robust boundary states found in its spectrum. Specifically, we analyze a system with three spectral bands, which possess non-quantized Zak's phases. However, spectral symmetries lead to quantized topological invariants, revealed when squaring the Hamiltonian, which determine its topological phase. The resulting states, related to the invariants by the bulk boundary correspondence, may be seen as in-gap, protected and controllable qubits. Photonic platforms have proven to serve as versatile platforms for the implementation of topological phenomena[15], such as Floquet TIs[16], TIs on a silicon platform[17], 2D[11] and 4D topological Hall physics[18], as well as non-Hermitian topological physics[19]. Along these lines, we utilize photonic waveguide arrays with a specifically tailored effective negative hopping to implement our theoretical findings.

Results

Theoretical model. We consider a chain made of Aharonov–Bohm cages, i.e., a quasi-1D lattice composed of interconnected plaquettes, see Fig. 1a. Each lattice site is coupled to its neighbors with hopping amplitude t, while each plaquette is threaded by a flux ϕ. The momentum space Hamiltonian of this model is given by

$$H(k) = t\begin{pmatrix} 0 & 1+\mathrm{e}^{-\mathrm{i}k} & \mathrm{e}^{-\mathrm{i}\phi}+\mathrm{e}^{-\mathrm{i}k} \\ 1+\mathrm{e}^{\mathrm{i}k} & 0 & 0 \\ \mathrm{e}^{\mathrm{i}\phi}+\mathrm{e}^{\mathrm{i}k} & 0 & 0 \end{pmatrix} \equiv t\sum_{i=1}^{4} d_i\lambda_{3+i}, \tag{1}$$

where λ_i, with $i = 1, \ldots, 8$, are the eight Gell–Mann matrices (defined in Supplementary Note 5) and $\mathbf{d} = (d_1, d_2, d_3, d_4)$ is a 4-component real-valued vector with $d_1 = 1 + \cos k$, $d_2 = \sin k$, $d_3 = \cos\phi + \cos k$, and $d_4 = \sin\phi + \sin k$. The spectrum of $H(k)$ has three bands: a central band that remains nondispersive for all values of the flux ϕ, and two additional particle–hole symmetric bands. For $\phi = 0$, the three bands cross, while for $\phi = \pi$ the spectrum is gapped with three flat bands at energies $E_i \in \{-2t, 0, 2t\}$, see Fig. 1b. The latter case corresponds to the Aharonov–Bohm caging effect, where the particles become immobile due to destructive interference[20–22].

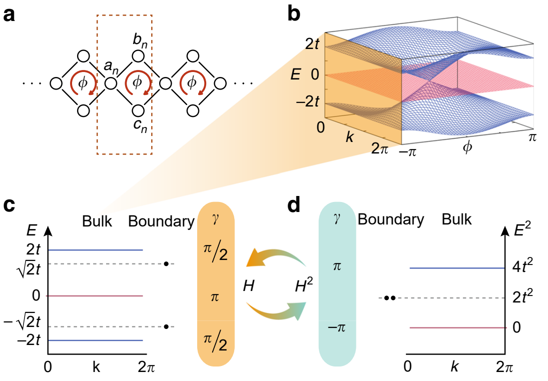

Fig. 1 The Aharonov–Bohm cages. a A chain of Aharonov–Bohm cages [cf. Eq. (1)], with three sites a_n, b_n, c_n in the nth unit cell and a flux ϕ threading each plaquette. **b** The energy dispersion $E(k)$ of the chain as a function of the flux ϕ. **c** The energy dispersion $E(k)$ at $\phi = \pi$ consists of three flat band at energies 0 and $\pm 2t$. The band at $E = 0$ has a quantized Zak's phase $\gamma = \pi$ while the other two bands show a non-quantized winding of $\pi/2$. At a termination of the chain with site a_n, two in-gap boundary states appear at $E = \pm\sqrt{2}t$. **d** Squaring the Hamiltonian (1) yields a model (2) with one flat band at $E = 0$ and two degenerate flat bands at $E = 4t^2$. Both bands have a quantized Wilczek-Zee phase $|\gamma| = \pi$.

For each band, we can evaluate a 1D topological invariant, Zak's winding phase $\gamma_i = \int_{\mathrm{BZ}} \mathrm{d}k\mathcal{A}_i(k)$, where $\mathcal{A}_i(k) = \mathrm{i}\langle v_i(k)|\partial_k|v_i(k)\rangle$ is the Berry connection of the ith band and $|v_i(k)\rangle$ is the corresponding eigenstate[23]. For a standard 1D TI (e.g., the Su–Shrieffer–Heeger (SSH) model), the winding phase takes quantized values of π (or 0) corresponding to encircling (or not encircling) a singularity in quasi-momentum phase space[24]. For our model, we find that the zero-energy band has a winding phase $\gamma_2 = \pi$, whereas the top and bottom bands have $\gamma_1 = \gamma_3 = -\pi/2$. Moreover, the winding phases are quantized to these values, $\gamma_2 \in \{0, \pi\}$ mod 2π and $\gamma_1 = \gamma_3 \in \{0, \frac{\pi}{2}\}$ mod 2π, by a nonsymmorphic transformation $\chi = \frac{1}{3}\mathbb{1} - \mathrm{e}^{\mathrm{i}k}\lambda_3 - \frac{1}{3}\lambda_8$ (see Supplementary Note 1 for the transformation for a general ϕ flux). The Hamiltonian $H(k)$ holds one additional non-symmorphic symmetry $\Pi = \frac{1}{3}\mathbb{1} + \mathrm{e}^{\mathrm{i}k}\lambda_3 - \frac{1}{3}\lambda_8$ (see Supplementary Note 1 for the transformation for a general ϕ flux) that quantizes the winding phases to $\gamma_2 \in \{0, \pi\}$ mod 2π and $\gamma_1 + \gamma_3 \in \{0, \pi\}$ mod 2π[25]. Thus, a χ-breaking term in the Hamiltonian $H(k)$ makes the phases γ_1 and γ_3 of the spectrally separated bands non-quantized and continuously mixed.

The AB-cages chain, with $\phi = \pi$ and open boundary conditions, has two in-gap states at energies $\pm\sqrt{2}t$ localized on the same boundary. Interestingly, their localization and energy are robust against disorder that does not break the Π- or χ-symmetry (see Fig. 2 and Supplementary Note 7). Hence, the AB-cages chain has robust boundary states, even when the winding phases γ_1 and γ_3 are not quantized. Commonly, robust boundary states appear in a gap that lies above bands that have a quantized topological index[13–15]. The appearance of such symmetry-protected states is a surprising occurrence for our case where non-quantized bulk windings arise.

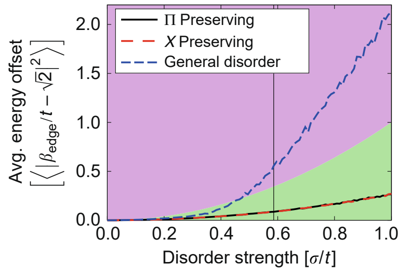

Fig. 2 Disorder analysis. The averaged mean squared difference $\langle|\beta_{\mathrm{edge}}/t-\sqrt{2}|^2\rangle$ between the boundary state energy β_{edge} in the presence of disorder and the energy of the undisturbed system $\beta_0=\sqrt{2}t$, as a function of the disorder strength σ. Three different disorder types are used, which either do not break one of the symmetries (χ or Π) or break both. All three disorder types are chosen such that on average both symmetries, χ and Π, are preserved, i.e., the disorder distribution has a vanishing mean. The vertical solid line indicates the size of the gap between the boundary state and the nearest bulk band. The red and green regions define an energy offset that is bigger (red) or smaller (green) than $(\sigma/t)^2$, which corresponds to the energy scale of the disorder. The disorder-averaging simulations were run using a lattice with 99 sites and every disorder strength σ was realized 10,000 times.

The topological aspects of the model are revealed by taking the square of the Hamiltonian matrix (1)

$$H^2(k) = t^2\begin{pmatrix} 2m_0 & 0 & 0 \\ 0 & m_0+m_3 & m_1+\mathrm{i}m_2 \\ 0 & m_1-\mathrm{i}m_2 & m_0-m_3 \end{pmatrix} \equiv t^2 m_0\left(\frac{4}{3}\mathbb{1}+\frac{1}{3}\lambda_8\right)+t^2\sum_{i=1}^{3} m_i\lambda_i, \qquad (2)$$

where $m_0=\sqrt{m_1^2+m_2^2+m_3^2}$, $m_1=1+\cos(k)+\cos(\phi)+\cos(k-\phi)$, $m_2=\sin(k)+\sin(\phi)-\sin(k-\phi)$, and $m_3=\cos(k)-\cos(k-\phi)$. The squared Hamiltonian is block diagonal with a single band $|w_1\rangle$ at energy $\Lambda_1=2t^2m_0$ and a 2×2 subblock with $|w_2\rangle$ and $|w_3\rangle$ eigenstates at energies $\Lambda_2=0$ and $\Lambda_3=2t^2m_0$, respectively. The latter two form a subblock that corresponds to a topologically nontrivial 1D model which maps to the SSH model by a rotation with $\mathrm{e}^{\mathrm{i}\lambda_3\frac{(\pi-\phi)}{4}}\mathrm{e}^{\mathrm{i}\lambda_2\frac{\pi}{4}}$. Specifically, at $\phi=\pi$, the resulting 2×2 subblock is equivalent to the SSH-chain with 0 intra-cell coupling, $2t^2$ inter-cell coupling, and a constant $2t^2$ energy shift (see Supplementary Fig. 3).

Importantly, $|w_1\rangle$ and $|w_3\rangle$ form a degenerate subspace at energy $\Lambda_1=\Lambda_3=2t^2m_0$. Therefore, these bands are assigned a Wilzcek–Zee phase which generalizes Zak's phase to multiband scenarios[26], $\gamma=\int_{\mathrm{BZ}}\mathrm{Tr}\,(\mathcal{A}(k))\mathrm{d}k$, where $\mathcal{A}(k)^{nm}=\langle v_n(k)|\partial_k|v_m(k)\rangle$, and n, m run over the involved states. For the squared Hamiltonian $H^2(k)$, the Wilzcek–Zee phase of both the zero-energy band and the degenerate subspace is quantized to $\{0,\pi\}$ mod 2π due to the Π- and χ-transformations (see Supplementary Note 3). As a result, the standard bulk-boundary correspondence of 1D TIs applies[27] and the open boundary spectrum of the Hamiltonian (2) maintains mid-gap states localized at the boundary. When $\phi=\pi$, the energy of these states is pinned to $2t^2$. Hence, the two energetically separated states appearing at the boundary of the AB cages are mapped, under the squaring operation, onto topological boundary states of the squared Hamiltonian. This leads to their characteristic robustness, both in localization and energy, against disorder that preserves the corresponding symmetry that quantizes the topological phases in $H^2(k)$ (see Fig. 2).

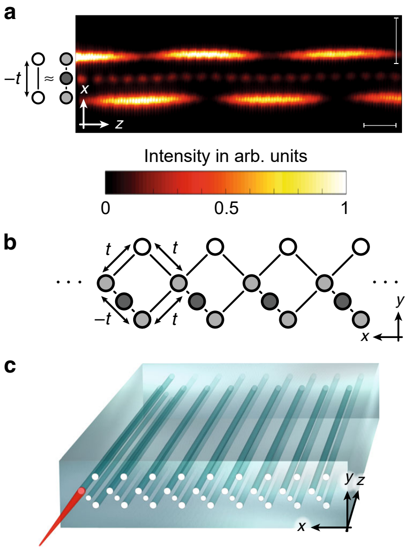

Fig. 3 Experimental implementation. a Light dynamics in the three level system of two waveguides and an auxiliary waveguide with carefully chosen refractive index. Since most of the amplitude is in the original waveguides, we can trace out the dynamics of the auxiliary waveguide and obtain a two-level system with an effective negative hopping $-t$. The horizontal scale bar corresponds to 1 cm, while the vertical scale bar corresponds to 25 µm. **b** Placing such a defect within each plaquette of the lattice structure generates a total flux of $\phi=\pi$. **c** An illustration of the quasi-1D array of evanescently coupled waveguides used in the experiment. Light is selectively injected into an input facet of the device and directly imaged using fluorescence microscopy.

Experimental realization. We implement the AB-cages chain (1) in photonic waveguide lattices fabricated using the femtosecond laser writing technique in bulk glass[28]. The evolution of light propagating along the z-direction of an array of single-mode waveguides can be well described in the paraxial approximation through a set of coupled mode equations $\mathrm{i}\partial_z\psi=H\psi$. The wavefunction ψ represents the excited optical wavepacket as a superposition of bound modes of the waveguides. The matrix H has diagonal elements corresponding to the refractive indices of the waveguides and off-diagonal coupling elements being proportional to the overlap between the bound modes of neighboring waveguides. Thus, discrete Schrödinger equations can be simulated in waveguide arrays with the benefit that the time coordinate in the quantum regime is mapped onto a spatial propagation distance in the optical system. In other words, the propagation of an optical wavepacket through a waveguide system simulates the temporal dynamics of an electron in a potential landscape. Notably, using fluorescence microscopy we can directly image the light propagation along the device[29].

In order to generate an effective AB-phase threading each cage, we use Peierls' substitution and associate an effective phase to one of the hopping amplitudes, see Fig. 3. Engineering a hopping phase for photons is challenging since the positive refractive index of each waveguide always results in a real and positive coupling between the waveguides. Nevertheless, by positioning an auxiliary waveguide with a well-tuned refractive index in between two waveguides[30], an effective negative coupling between the two original waveguides is generated (see Supplementary Note 8). Crucially, the auxiliary waveguide is engineered such that it does

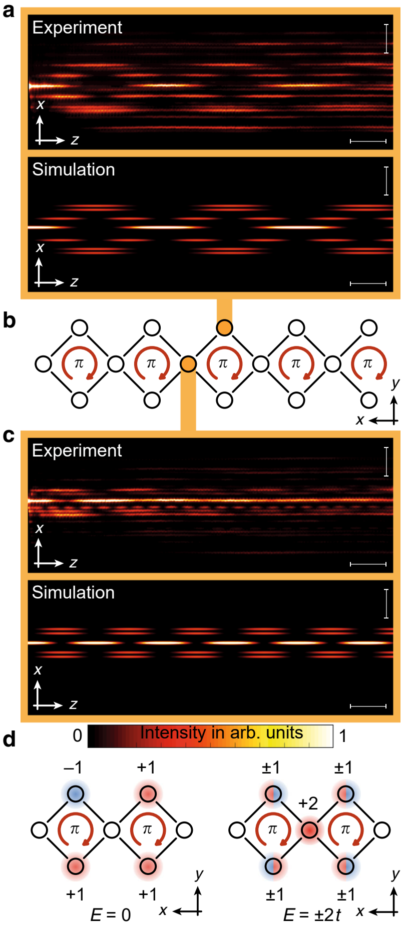

Fig. 4 Bulk dynamics. a Light dynamics when exciting the top waveguide in a bulk plaquette. The total envelope remains localized and shows breathing only within the plaquette. Differences between simulations and experiment arise mainly due to small amounts of light leaking into neighboring waveguides during the excitation of the waveguide. This generates a slightly different initial state launched into the system resulting in small deviations of the propagation dynamics. The horizontal scale bar corresponds to 1 cm, while the vertical scale bar corresponds to 50 µm. **b** The two waveguides that are probed in the experiments demonstrating the flatness of the bulk spectrum. **c** Light dynamics in the structure when a waveguide between two plaquettes is excited. The total envelope shows a local breathing while being localized within the plaquette. The horizontal scale bar corresponds to 1 cm, while the vertical scale bar corresponds to 50 µm. **d** The amplitude distribution of the three bulk eigenstates of the system.

not contribute significantly to the dynamics of the system, see Fig. 3a. By choosing the refractive index of the two original waveguides to energetically match the effective two-level system with the rest of the lattice (see Supplementary Note 8) and placing a negative coupling in each plaquette of our waveguide structure (see Fig. 3b), an overall flux of π within the plaquettes is created, resulting in the desired AB-caging effect (see Fig. 3c for an illustration of the device).

We first establish our ability to generate the AB-caging effect in the bulk of the chain by probing the light dynamics to test the flatness of the bands, see Fig. 4. Exciting a single waveguide within a plaquette will excite all k-states of Bloch bands that overlap with this site. For flat bands, the light will stay bound to the injection point and will not disperse. We perform two experiments corresponding to two different injection sites within the unit cell, see Fig. 4a–c. Indeed, despite of some residual spreading due to imperfect injection and weak disorder in the device, in both experiments the propagating wavepacket remains confined to the injected unit cell. The experimental measurements agree well with tight-binding simulations of the AB chain. In contrast, light propagation for the case of vanishing flux $\phi = 0$ shows no localization and the wavepacket spreads to the entire lattice (see Supplementary Fig. 7).

From the light propagation along the sample (see Fig. 4), we can additionally measure the energy of the bands: launching light into a waveguide that connects two plaquettes solely excites the two states in the bands at $E = \pm 2t$, as the state from the band at $E = 0$ has no weight in this site, see Fig. 4c, d. The resulting beating pattern is, therefore, generated by two modes with a beating length l_b that is connected to the energy difference ΔE of the participating modes by[31] $l_b = \frac{\pi}{\Delta E}$. From the beating in Fig. 4c, we measure $l_b = 0.9$ cm, which corresponds to $\Delta E = \pm 3.4\ \mathrm{cm}^{-1}$. Taking into account the particle-hole symmetry of the model, the energy of the two bands are therefore measured to be at $E = \pm 1.7\ \mathrm{cm}^{-1}$ while the third band lies at $E = 0$.

We, now, demonstrate the existence of the boundary states in our square-root model. The amplitude distribution of the predicted boundary modes is shown in Fig. 5a, b. The two states differ by a phase flip and appear at two inequivalent eigenenergies, cf. Fig. 1c. Hence, similarly to the bulk experiments above, light injected into the outermost waveguide simultaneously excites both boundary modes and the resulting light pattern exhibits a beating with a frequency corresponding to the difference between their eigenenergies, see Fig. 5c. Our experimental data agree well with tight-binding simulations shown in Fig. 5d. From the beating structure, we can determine the energy of the boundary modes E_e: we observe a beating with $l_b = 1.3$ cm and, hence, deduce that $E_e = \pm 1.2\ \mathrm{cm}^{-1}$. Comparing the observed energies in the bulk and in the boundary, we find that $\frac{E^2}{E_e^2} \sim 2$, in agreement with the predictions of the model (1).

Discussion

In our work, we have predicted and demonstrated the physics of a square-root TI, using a photonic platform. Specifically, we show that the AB cages with $\phi = \pi$ have in-gap states at energies $\pm\sqrt{2}t$, above bands possessing $\pi/2$ or π mod 2π Zak's phases. We find that these states are robust, both in energy and localization, against disorder that does not break the symmetries that quantize the topological indices in the corresponding system where the square of the Hamiltonian is taken. Furthermore, we show that the squaring operation bijectively maps the boundary states of H to specific boundaries of H^2. Extending this description to the regime where γ_1 and γ_3 are not quantized, e.g., by adding a term that preserves Π but breaks χ, we find that the localization and energy deviation of the boundary states remain robust against additional Π-preserving disorder, but their energies are now fixed to a different value (see Supplementary Note 6). In this case, the mapping of the square operation is generalized using the properties of SU(3) algebra, while the symmetry protection in the square-root model still manifests due to the quantization of the topological indices of the squared Hamiltonian by the Π-symmetry (see Supplementary Note 6). Contrary to previous implementations of photonic AB cages using different experimental techniques[22], we provide an interpretation to the underlying physics which is independent of the specific model.

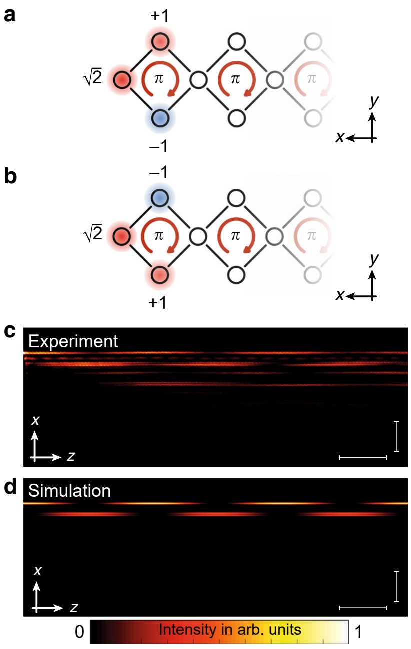

Fig. 5 Boundary dynamics and symmetry protection. a Amplitude distribution of the boundary state with energy $E = \sqrt{2}t$. **b** Amplitude distribution of the boundary state with energy $E = -\sqrt{2}t$. **c** Beating pattern between two boundary states excited by launching light into the outermost waveguide of the structure. The horizontal scale bar corresponds to 1 cm, while the vertical scale bar corresponds to 50 µm. **d** Tight-binding simulations confirming the behavior.

With our work, we hope to stimulate a range of new theoretical and experimental studies exploring the implications and breadth of such phases of matter. In this vein, our experimental results give rise to various important questions: First, can our square-root TI phase be realized in ultracold atomic setups, where topological quantities can be observed via bulk wavepacket dynamics, rather than by detection of boundary states? Second, the boundary states appearing at $\pm\sqrt{2}t$ energies form a two-level system (with states $1/2\left[\sqrt{2}|a\rangle \pm (|b\rangle - |c\rangle)\right]$) that can be used as a qubit that is energetically separated from the bulk bands and is robust to disorder. Making the hopping of the last site weaker or methodically breaking the nonsymmorphic symmetries of the AB-cages model offer a control handle to reduce or asymmetrically tune the energy splitting of the boundary states. Can this be used for single-qubit operations? Third, our procedure differs from recent works[2,4] where the square of a even-dimensional model has been used to map between models with different degrees of freedom but same quantized winding phase. In our work the dimension of the Hilbert space is fixed, and the topological invariant reveals itself upon squaring; the question arises if there are other nonlinear maps between Hamiltonians that admit such a description? Fourth, the phenomenology of our model resembles the valence-bond structure of the Affleck, Kennedy, Lieb, and Tasaki ground state of the Haldane spin-chain[32]: each unit cell in the bulk has three states that form a spin-1 subspace, coupling to their neighbors with a specific tunnel coupling such that an unpaired spin-1/2 is left at the boundary. Can our work suggest a connection to the topology of spin models? Fifth, the quantized $\pi/2$ phases of the AB-cages model in the electronic domain will result into a boundary state with a $e/4$ charge. Can such a novel quasiparticle have nontrivial braiding statistics? Could its charge be tuned by controllably breaking the symmetries of the system? Finally, can the theoretical framework be generalized to higher dimensions? The answers to these questions are now in experimental reach.

Methods

Sample fabrication. The waveguides were written inside a high-purity 10 cm long fused silica wafer (Corning 7980) using a RegA 9000 seeded by a Mira Ti:Al_2O_3 femtosecond laser. Pulses centered at 800nm with duration of 150 fs were used at a repetition rate of 100 kHz and energy of 450 nJ. The pulses were focused 500 µm under the sample surface using an objective with a numerical aperture of 0.35 while the sample was translated at constant speed of 40, 200, and 220 mm/min, corresponding to the different detunings, by high-precision positioning stages (ALS130, Aerotech Inc.). The mode field diameters of the guided mode were 10.4 µm × 8.0 µm at 633 nm. Propagation losses were estimated to be 0.2 dB/cm. The waveguides are equally spaced by 21.5 µm for the positive and 28 µm for the negative coupling, resulting in an inter-site hopping of $|t| = 0.85\,\mathrm{cm}^{-1}$.

Fluorescence imaging. For the direct monitoring of the light propagation in our samples, we used a fluorescence microscopy technique[29]. A massive formation of nonbridging oxygen hole color centers occurs during the writing process, when fused silica with a high content of hydroxide is used, resulting in a homogeneous distribution of these color centers along the waveguides. When light from a Helium–Neon laser at $\lambda = 633$ nm is launched into the waveguides, the nonbridging oxygen hole color centers are excited and the resulting fluorescence ($\lambda = 650$ nm) can be directly observed using a CCD camera with an appropriate narrow linewidth filter. As the color centers are formed exclusively inside the waveguides, this technique yields a high signal-to-noise ratio.

Data availability

The data that support the findings of this study are available from the corresponding author upon reasonable request.

Received: 9 October 2019; Accepted: 23 January 2020;
Published online: 14 February 2020

References

1. Peskin, M. E. & Schroeder, D. V. *An Introduction to Quantum Field Theory*. (Addison-Wesley, Reading, 1995).
2. Kane, C. & Lubensky, T. Topological boundary modes in isostatic lattices. *Nat. Phys.* **10**, 39–45 (2014).
3. Cooper, F., Khare, A. & Sukhatme, U. Supersymmetry and quantum mechanics. *Phys. Rep.* **251**, 267–385 (1995).
4. Arkinstall, J., Teimourpour, M., Feng, L., El-Ganainy, R. & Schomerus, H. Topological tight-binding models from nontrivial square roots. *Phys. Rev. B* **95**, 165109-1–165109-16 (2017).
5. Klitzing, Kv, Dorda, G. & Pepper, M. New Method for high-accuracy determination of the fine-structure constant based on quantized hall resistance. *Phys. Rev. Lett.* **45**, 494–497 (1980).
6. Zhang, S.-C. & Hu, J. A four-dimensional generalization of the quantum Hall effect. *Science* **294**, 823–828 (2001).
7. Kitaev, A. Y. Unpaired Majorana fermions in quantum wires. *Physics* **44**, 131–136 (2001).
8. Kane, C. L. & Mele, E. J. Z 2 topological order and the quantum spin hall effect. *Phys. Rev. Lett.* **95**, 146802-1–146802-4 (2005).
9. Hsieh, D. et al. A topological Dirac insulator in a quantum spin Hall phase. *Nature* **452**, 970–974 (2008).
10. Fu, L. Topological crystalline insulators. *Phys. Rev. Lett.* **106**, 106802-1–106802-4 (2011).
11. Kraus, Y. E., Lahini, Y., Ringel, Z., Verbin, M. & Zilberberg, O. Topological states and adiabatic pumping in quasicrystals. *Phys. Rev. Lett.* **109**, 106402-1–106402-5 (2012).
12. Benalcazar, W. A., Bernevig, B. A. & Hughes, T. L. Quantized electric multipole insulators. *Science* **357**, 61–66 (2017).
13. Hasan, M. Z. & Kane, C. L. Colloquium: topological insulators. *Rev. Mod. Phys.* **82**, 3045–3067 (2010).
14. Qi, X.-L. & Zhang, S.-C. Topological insulators and superconductors. *Rev. Mod. Phys.* **83**, 1057–1110 (2011).
15. Ozawa, T. et al. *Reviews of Modern Physics* **91**, 15006-1–15006-76 (2019).
16. Rechtsman, M. C. et al. Photonic floquet topological insulators. *Nature* **496**, 196–200 (2013).

17. Hafezi, M., Mittal, S., Fan, J., Migdall, A. & Taylor, J. M. Imaging topological edge states in silicon photonics. *Nat. Photonics* **7**, 1001–1005 (2013).
18. Zilberberg, O. et al. Photonic topological boundary pumping as a probe of 4d quantum hall physics. *Nature* **553**, 59–62 (2018).
19. Weimann, S. et al. Topologically protected bound states in photonic parity-time-symmetric crystals. *Nat. Mater.* **16**, 433–438 (2017).
20. Vidal, J., Mosseri, R. & Douçot, B. Aharonov-Bohm cages in two-dimensional structures. *Phys. Rev. Lett.* **81**, 5888–5891 (1998).
21. Longhi, S. Aharonov-bohm photonic cages in waveguide and coupled resonator lattices by synthetic magnetic fields. *Opt. Lett.* **39**, 5892–5895 (2014).
22. Mukherjee, S., Di Liberto, M., Öhberg, P., Thomson, R. R. & Goldman, N. Experimental observation of Aharonov-Bohm cages in photonic lattices. *Phys. Rev. Lett.* **121**, 075502-1–075502-6 (2018).
23. Zak, J. Berry's phase for energy bands in solids. *Phys. Rev. Lett.* **62**, 2747–2750 (1989).
24. Asbóth, J. K, Oroszlány, L. & Pályi, A. *A Short Course on Topological Insulators*. (Springer: Berlin, 2016).
25. Marques, A. M. & Dias, R. G. One-dimensional topological insulators with noncentered inversion symmetry axis. *Phys. Rev. B* **100**, 041104-1–041104-5 (2019).
26. Wilczek, F. & Zee, A. Appearance of gauge structure in simple dynamical systems. *Phys. Rev. Lett.* **52**, 2111–2114 (1984).
27. Prodan, E. & Schulz-Baldes, H. *Bulk and Boundary Invariants for Complex Topological Insulators*. (Springer, Berlin, 2016).
28. Szameit, A. & Nolte, S. Discrete optics in femtosecond-laser-written photonic structures. *J. Phys. B* **43**, 163001-1–163001-25 (2010).
29. Szameit, A. et al. Quasi-incoherent propagation in waveguide arrays. *Appl. Phys. Lett.* **90**, 241113-1–241113-3 (2007).
30. Keil, R. et al. Universal sign control of coupling in tight-binding lattices. *Phys. Rev. Lett.* **116**, 213901-1–213901-5 (2016).
31. Yariv, A. *Quantum Electronics*. 3rd ed. (John Wiley & Sons, New York, 1989).
32. Affleck, I., Kennedy, T., Lieb, E. H. & Tasaki, H. Rigorous results on valence-bond ground states in antiferromagnets. *Phys. Rev. Lett.* **59**, 799–802 (1987).

Acknowledgements

We thank J. Shapiro, G.-M. Graf, D. Bercioux, and J. Vidal for fruitful discussions. I.P. and O.Z. acknowledge financial support from the Swiss National Science Foundation (SNF). A.S. thanks the Deutsche Research Foundation (grants SZ 276/7-1, SZ 276/9-1, BL 574/13-1, and SZ 276/19-1) and the Krupp von Bohlen and Halbach foundation. The authors would also like to thank C. Otto for preparing the high-quality fused silica samples used in all experiments presented here.

Author contributions

M.K., I.P., A.S., and O.Z. developed the concept, I.P. and O.Z. developed the theory, M.K., E.M., M.H., and A.S. designed the lattice structure, M.K. and E.M. performed the experiments, all authors discussed the results and co-wrote the paper.

Competing interests

The authors declare no competing interests.

Additional information

Supplementary information is available for this paper at https://doi.org/10.1038/s41467-020-14692-4.

Correspondence and requests for materials should be addressed to O.Z. or A.S.

Peer review information *Nature Communications* thanks Meng Xiao and the other, anonymous, reviewer(s) for their contribution to the peer review of this work. Peer reviewer reports are available.

Reprints and permission information is available at http://www.nature.com/reprints

Publisher's note Springer Nature remains neutral with regard to jurisdictional claims in published maps and institutional affiliations.

Open Access This article is licensed under a Creative Commons Attribution 4.0 International License, which permits use, sharing, adaptation, distribution and reproduction in any medium or format, as long as you give appropriate credit to the original author(s) and the source, provide a link to the Creative Commons license, and indicate if changes were made. The images or other third party material in this article are included in the article's Creative Commons license, unless indicated otherwise in a credit line to the material. If material is not included in the article's Creative Commons license and your intended use is not permitted by statutory regulation or exceeds the permitted use, you will need to obtain permission directly from the copyright holder. To view a copy of this license, visit http://creativecommons.org/licenses/by/4.0/.

© The Author(s) 2020

Supplementary Information for

A square-root topological insulator with non-quantised indices realised with photonic Aharonov-Bohm cages

Mark Kremer[1], Ioannis Petrides[2,], Eric Meyer[1], Matthias Heinrich[1],
Oded Zilberberg[2], and Alexander Szameit[1]

[1] *Institut für Physik, Universität Rostock, Albert-Einstein-Straße 23, 18059 Rostock, Germany.*
[2] *Institut für Theoretische Physik, ETH Zürich, Wolfgang-Pauli-Straße 27, 8093 Zürich, Switzerland.*

SUPPLEMENTARY FIGURES

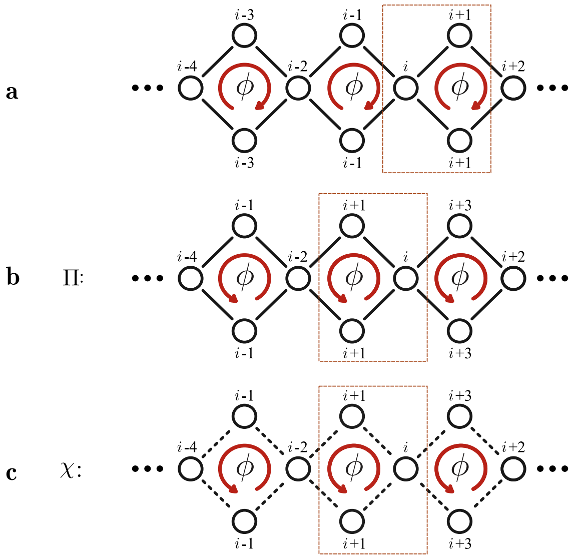

Supplementary Figure 1. The two non symmorphic symmetries, Π and χ, acting on an infinite chain of AB-cages with periodic boundary conditions. **a** The original lattice of AB-cages with flux ϕ threading each plaquette. **b** The lattice obtained after a Π transformation. **c** The lattice obtained after a χ transformation. The dashed box shows a chosen set of basis points. Solid (dashed) lines denote positive (negative) hopping strengths.

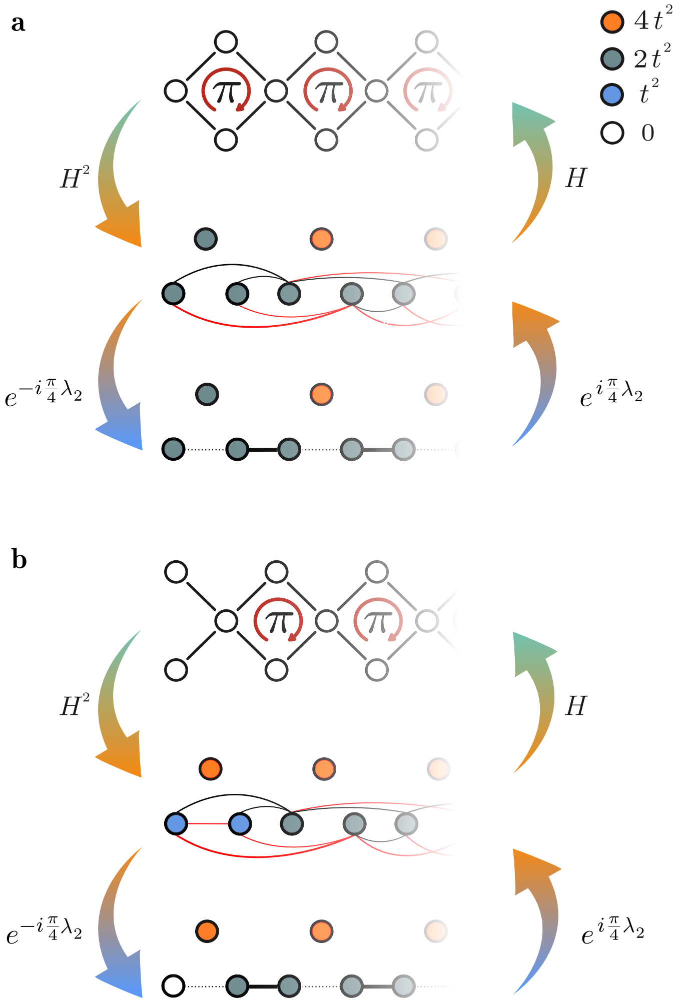
a
π
π
π
H^2
H
$e^{-i\frac{\pi}{4}\lambda_2}$
$e^{i\frac{\pi}{4}\lambda_2}$
● $4t^2$
● $2t^2$
● t^2
○ 0
b
π
π
H^2
H
$e^{-i\frac{\pi}{4}\lambda_2}$
$e^{i\frac{\pi}{4}\lambda_2}$

Supplementary Figure 2. Square mapping semi-infinite chains. **a** A semi-infinite chain of Aharonov-Bohm cages with a termination that supports two nontrivial topological in-gap boundary states [cf. Supplementary Eq. (10)]. The corresponding H^2 model exhibits at its boundary two in-gap degenerate states: one appears as a standard manifestation of the SSH model's bulk-boundary correspondence and the second belongs to the subspace of isolated states, now found at a lower energy [cf. Supplementary Eq. (18)]. **b** A semi-infinite chain of Aharonov-Bohm cages with a termination that does not support topological in-gap boundary modes [cf. Supplementary Eq. (12)]. The corresponding H^2 model similarly does not exhibit topological in-gap boundary states: the standard SSH model has a termination with corresponding boundary mode that is lowered to hybridize with the bulk band at zero energy [cf. Supplementary Eq. (21)].

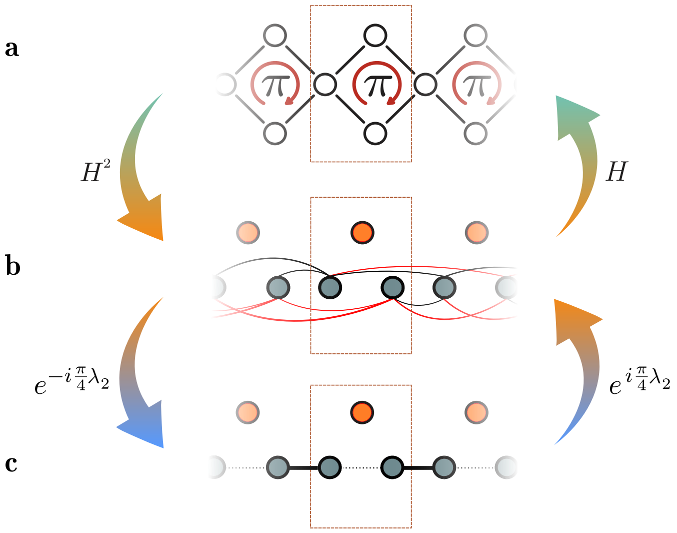

Supplementary Figure 3. Square mapping the infinite chain. **a** An infinite chain of Aharonov-Bohm cages with $\phi = \pi$ is mapped to **b** a chain with positive (black) and negative (red) next-to-nearest neighbour hopping and one decoupled state per unit cell. Rotating the basis with $\mathrm{e}^{-\mathrm{i}\frac{\pi}{4}\lambda_2}$, the latter is mapped to **c** the SSH model with an additional decoupled state per unit cell.

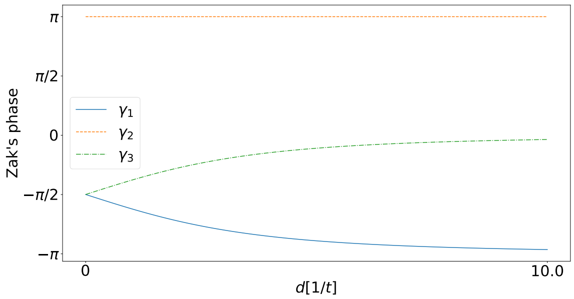

Supplementary Figure 4. Zak's winding phases of the bands of $H(k)$ [cf. Supplementary Eq. (32)] as a function of the on-site potential d. The winding of the zero-energy band γ_2 remains unaltered, whereas γ_1 and γ_3 are continuously mixed to the point where $\gamma_1 \to \pi$ and $\gamma_3 \to 0$.

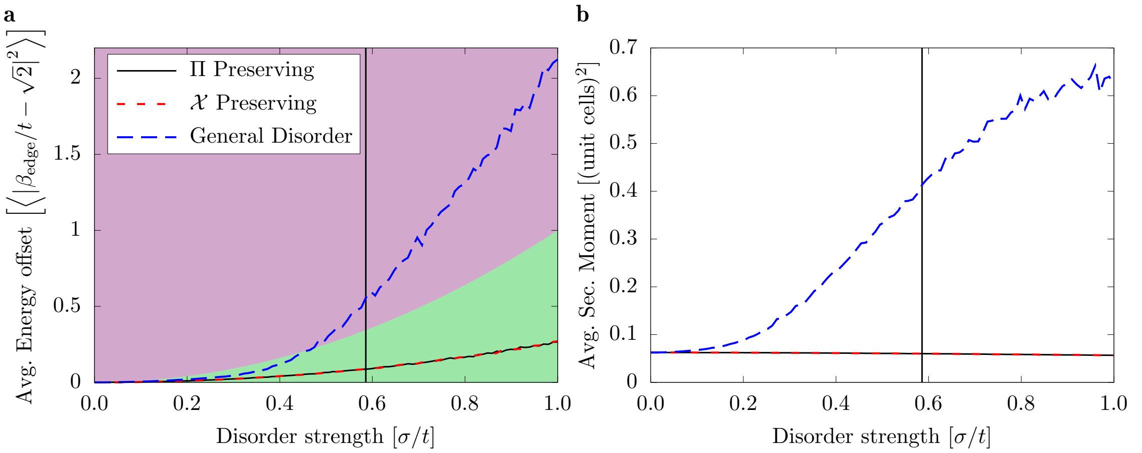

Supplementary Figure 5. **Disorder Analysis of Energy and Localisation.** **a** Disorder analysis of the energy offset of the topological edge state with on average preserved symmetries. The vertical axis shows the averaged mean squared difference $\langle|\beta_{\text{edge}}/t-\beta_0/t|^2\rangle$ of the edge state energy β_{edge} in the presence of disorder and the energy of the undisturbed system $\beta_0=\sqrt{2}t$. The vertical colored solid line indicates where the standard deviation of the disorder reaches the size of the gap from the boundary state to the nearest bulk band in each corresponding case. The red and green regions define an energy offset that is bigger (red) or smaller (green) than $(\sigma/t)^2$, which would correspond to a an energy offset proportional to the disorder strength.**b** The average second moment (localization length) of the eigenstate, corresponding to the eigenenergy of **a**. Each disorder type was realized to either preserve, or break certain symmetries, as labeled in the plots. The disorder-averaging simulations were run using a lattice with 99 sites and every disorder strength was realized 10000 times.

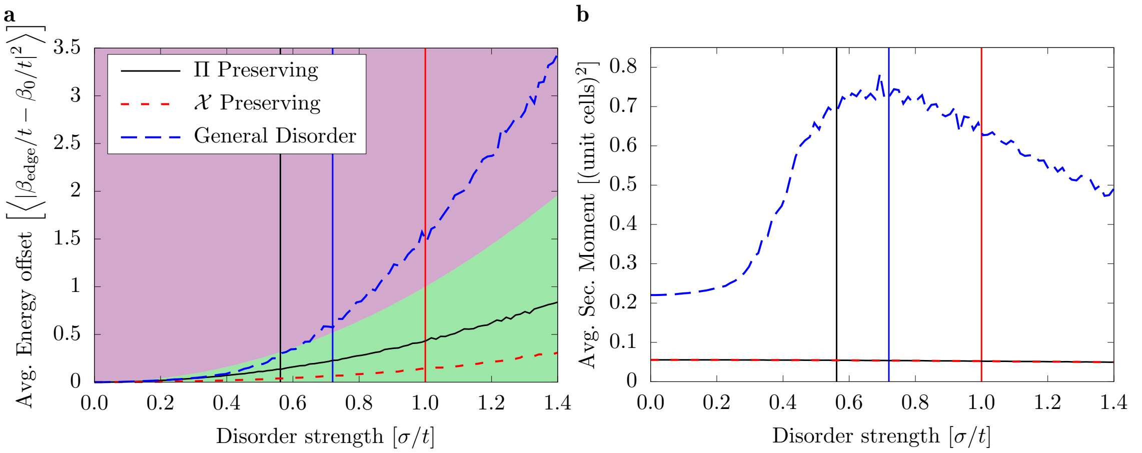

Supplementary Figure 6. **Disorder Analysis of Energy and Localisation.** **a** Disorder analysis of the energy offset of the topological edge state with on average broken symmetries. The vertical axis shows the averaged mean squared difference $\langle|\beta_{\text{edge}}/t-\beta_0/t|^2\rangle$ of the edge state energy β_{edge} in the presence of disorder and the energy of the undisturbed system β_0 (i.e., when $\sigma=0$). The vertical colored solid lines indicate where the standard deviation of the disorder reaches the size of the gap from the boundary state to the nearest bulk band in each corresponding case. The red and green regions define an energy offset that is bigger (red) or smaller (green) than $(\sigma/t)^2$, which would correspond to a an energy offset proportional to the disorder strength.**b** The average second moment (localization length) of the eigenstate, corresponding to the eigenenergy of **a**. Each disorder type was realized to either preserve, or break certain symmetries, as labeled in the plots. The disorder-averaging simulations were run using a lattice with 99 sites and every disorder strength was realized 10000 times.

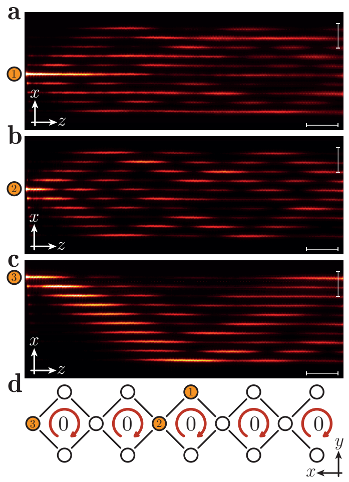

Supplementary Figure 7. **Propagation without Flux.** **a** Light dynamics when exciting the top site in a single bulk plaquette without flux (labeled as 1 in **d**). The horizontal scale bar corresponds to 1 cm, while the vertical scale bar corresponds to 50 μm. **b** Light dynamics when exciting the lattice site inbetween two bulk plaquettes without flux (labeled as 2 in **d**). The horizontal scale bar corresponds to 1 cm, while the vertical scale bar corresponds to 50 μm. **c** Light dynamics when exciting the edge lattice site of a lattice without flux (labeled as 3 in **d**). The horizontal scale bar corresponds to 1 cm, while the vertical scale bar corresponds to 50 μm. **d** Overview of which lattice sites are excited in **a**-**c**.

SUPPLEMENTARY NOTES

Supplementary Note 1

Here we discuss the Bulk properties of $H(k)$.The spectrum of $H(k)$ [cf. Eq. (1) in the main text] has three bands at energies $\pm t\sqrt{2}\sqrt{1+\cos k+\cos{(k-\phi)}}$ and 0, see Fig. 1a in the main text. When the flux threading the plaquettes is $\phi \neq 0 \bmod 2\pi$, the three bands are isolated from each other, therefore, an Abelian Zak's phase can be defined to each,

$$\gamma_i = \mathrm{i}\int\limits_{-\pi}^{\pi} \mathrm{d}k \langle v_i(k)|\partial_k|v_i(k)\rangle \,, \tag{1}$$

where $i=1,2,3$ labels the bands in increasing energy. The bulk band solutions $|v_i(k)\rangle$ are found by diagonalizing the Hamiltonian $H(k)$ and can be written in a nonsingular, analytical form

$$|v_1\rangle = \frac{1}{2\sqrt{2}}\begin{pmatrix} -2\sqrt{2+\cos k+\cos{(k-\phi)}} \\ 1+\mathrm{e}^{\mathrm{i}k} \\ \mathrm{e}^{\mathrm{i}\phi}+\mathrm{e}^{\mathrm{i}k} \end{pmatrix}, \quad |v_2\rangle = \frac{1}{2}\begin{pmatrix} 0 \\ \mathrm{e}^{\mathrm{i}\phi}+\mathrm{e}^{\mathrm{i}k} \\ 1+\mathrm{e}^{\mathrm{i}k} \end{pmatrix}, \quad |v_3\rangle = \frac{1}{2\sqrt{2}}\begin{pmatrix} 2\sqrt{2+\cos k+\cos{(k-\phi)}} \\ 1+\mathrm{e}^{\mathrm{i}k} \\ \mathrm{e}^{\mathrm{i}\phi}+\mathrm{e}^{\mathrm{i}k} \end{pmatrix}. \tag{2}$$

Using Supplementary Eqs. (1) and (2), we find

$$\begin{aligned} \gamma_1 = \gamma_3 &= \frac{3\pi}{2} \bmod 2\pi \\ \gamma_2 &= \pi \bmod 2\pi \,. \end{aligned} \tag{3}$$

The winding phases of $H(k)$ [cf. Supplementary Eqs. (3)] are constrained by two nonsymmorphic symmetries (see Supplementary Figure 1), namely

$$\chi = \begin{pmatrix} 1 & 0 & 0 \\ 0 & -\mathrm{e}^{-\mathrm{i}k} & 0 \\ 0 & 0 & -\mathrm{e}^{-\mathrm{i}\phi}\mathrm{e}^{-\mathrm{i}k} \end{pmatrix} \text{ and } \Pi = \begin{pmatrix} 1 & 0 & 0 \\ 0 & \mathrm{e}^{-\mathrm{i}k} & 0 \\ 0 & 0 & \mathrm{e}^{-\mathrm{i}\phi}\mathrm{e}^{-\mathrm{i}k} \end{pmatrix}, \tag{4}$$

The above transformations act on the Hamiltonian in the following way

$$\Pi H(k)\Pi^{-1} = H^*(k) \,, \tag{5}$$

$$\chi H(k)\chi^{-1} = -H^*(k) \,, \tag{6}$$

where $H^*(k)$ is the conjugate Hamiltonian and the equalities are up to gauge transformations. These symmetries lead to the following relations between the winding phases of the bands:

$$\begin{aligned} \Pi: \quad & \gamma_1+\gamma_3 \in \{0,\pi\} \quad && \text{and} \quad && \gamma_2 \in \{0,\pi\}\,, \\ \chi: \quad & \gamma_1=\gamma_3 \in \{0,\pm\pi/2\} \quad && \text{and} \quad && \gamma_2 \in \{0,\pi\}\,. \end{aligned} \tag{7}$$

Breaking the χ symmetry with an onsite potential allows γ_1 and γ_3 to take any phase value, but, interestingly, their sum remains a $\mathbb{Z}_2$ invariant due to the Π symmetry(see Supplementary Note 6).

Supplementary Note 2

Here we discuss the boundary properties of H. To derive the explicit solutions of boundary states, we first consider a semi-infinite AB-cages chain, at $\phi=\pi$, with a termination shown in Supplementary Figure 2A. The real-space representation of the Hamiltonian is given by

$$H = t\begin{pmatrix} D & T & 0 & \cdots \\ T^\dagger & D & T & \ddots \\ 0 & T^\dagger & D & \ddots \\ \vdots & \ddots & \ddots & \ddots \end{pmatrix}, \tag{8}$$

where t is the hopping amplitude,

$$D = \begin{pmatrix} 0 & 1 & -1 \\ 1 & 0 & 0 \\ -1 & 0 & 0 \end{pmatrix}, \quad \text{and} \quad T = \begin{pmatrix} 0 & 0 & 0 \\ 1 & 0 & 0 \\ 1 & 0 & 0 \end{pmatrix}. \tag{9}$$

Solutions localized within the unit cell of the termination can generally be written as $|e\rangle = (a, b, c, 0, \cdots)^T$ and must satisfy the matrix equation $H|e\rangle = E_e|e\rangle$, with E_e the energy of the boundary state. This leads to two orthogonal solutions given by

$$|e_1\rangle = \frac{1}{2}\left(\sqrt{2}, 1, -1, 0, \cdots\right)^T \text{ and } |e_2\rangle = \frac{1}{2}\left(\sqrt{2}, -1, 1, 0, \cdots\right)^T, \tag{10}$$

with $E_{e_1} = \sqrt{2}t$ and $E_{e_2} = -\sqrt{2}t$, respectively.

Following the same procedure, we now consider the alternative termination of the chain, shown in Supplementary Figure 2B. The real-space representation of the Hamiltonian is given by

$$H = \begin{pmatrix} D & T^\dagger & 0 & \cdots \\ T & D & T^\dagger & \ddots \\ 0 & T & D & \ddots \\ \vdots & \ddots & \ddots & \ddots \end{pmatrix}. \tag{11}$$

Solving the matrix equation $H|e\rangle = E_e|e\rangle$ for a localized state of the form $|e\rangle = (a, b, c, 0, \cdots)^T$ leads to a single solution

$$|e_0\rangle = \frac{1}{\sqrt{2}}(0, 1, 1, 0, \cdots)^T, \tag{12}$$

with $E_{e_0} = 0$. Importantly, this mode is degenerate with the central bulk band and does not manifest as a topological in-gap state.

Supplementary Note 3

Here we discuss the bulk properties of $H^2(k)$. The spectrum of $H^2(k)$ [cf. Eq. (2) in the main text], has a 2-fold degenerate subspace at energy $2t^2(1 + \cos k + \cos(k - \phi))$ and a single band at zero energy [cf. Fig. 1D in the main text]. In order to properly capture the topological phase of the degenerate bands we use a generalization of Supplementary Eq. (1), called the Wilzcek-Zee phase,

$$\gamma = \int\limits_{k}^{k+2\pi} \mathrm{Tr}\mathcal{A}(k)\mathrm{d}k, \tag{13}$$

where $\mathcal{A}(k)^{nm} = \langle v_n(k)|\partial_k|v_m(k)\rangle$, and n, m run over the involved states. The bulk solutions of $H^2(k)$ can be written in compact form as

$$|w_1\rangle = \begin{pmatrix} 1 \\ 0 \\ 0 \end{pmatrix}, \quad |w_2\rangle = \frac{1}{\sqrt{2}}\begin{pmatrix} 0 \\ \mathrm{e}^{\mathrm{i}\phi} + \mathrm{e}^{\mathrm{i}k} \\ 1 + \mathrm{e}^{\mathrm{i}k} \end{pmatrix}, \quad |w_3\rangle = \frac{1}{\sqrt{2}}\begin{pmatrix} 0 \\ 1 + \mathrm{e}^{\mathrm{i}k} \\ \mathrm{e}^{\mathrm{i}\phi} + \mathrm{e}^{\mathrm{i}k} \end{pmatrix}, \tag{14}$$

with eigenvalues $2t^2(1 + \cos k + \cos(k - \phi))$, 0 and $2t^2(1 + \cos k + \cos(k - \phi))$, respectively. The squared model, $H^2(k)$, has a band composed of decoupled sites, $|w_1\rangle$, that is degenerate with $|w_3\rangle$. The sub-model, defined by $|w_2\rangle$ and $|w_3\rangle$, is related to an effective Su-Schrieffer-Heeger (SSH) by a rotation $\mathrm{e}^{\mathrm{i}\lambda_3\frac{(\pi-\phi)}{4}}\mathrm{e}^{\mathrm{i}\lambda_2\frac{\pi}{4}}$. At $\phi = \pi$, the resulting effective SSH model is equivalent to a chain with 0 intra-cell coupling, $2t^2$ inter-cell coupling, and a constant $2t^2$ energy shift, see Supplementary Figure 3A, B and C. Using Supplementary Eq. (13) we find

$$\gamma_{1,3} = \pi \bmod 2\pi \quad \text{and} \quad \gamma_2 = \pi \bmod 2\pi. \tag{15}$$

where $\gamma_{1,3}$ denotes the phase of the degenerate subspace spanned by $|w_1\rangle$ and $|w_3\rangle$, and γ_2 is the phase of the single band at zero energy.

The two nonsymmorphic symmetries, Π and χ, obeyed by $H(k)$ are preserved under the squaring operation,

$$\begin{aligned}\Pi H^2(k)\Pi^{-1} &= \left(H^*(k)\right)^2 ,\\ \chi H^2(k)\chi^{-1} &= \left(H^*(k)\right)^2 .\end{aligned} \tag{16}$$

These transformations lead to the following relations between the Wilzcek-Zee phases:

$$\begin{aligned}\Pi: &\quad \gamma_{1,3} \in \{0,\pi\} \quad \text{and} \quad \gamma_2 \in \{0,\pi\},\\ \chi: &\quad \gamma_{1,3} \in \{0,\pi\} \quad \text{and} \quad \gamma_2 \in \{0,\pi\}.\end{aligned} \tag{17}$$

Importantly, breaking the χ-symmetry with an onsite potential on the a lattice sites does not make $\gamma_{1,3}$ nor γ_2 lose its quantization. This is because the Π-symmetry protects this quantization.

Supplementary Note 4

In this section we discuss the boundary states of H^2 and their mapping to the boundary states of H. The bulk indices of $H^2(k)$ show that the band polarization of the chain is quantized to nontrivial values. Since the bulk material is insulating, the bulk band polarization manifests as localized states on the boundary [1]. In the following, we give the correspondence between the boundary state found in the spectrum of H (cf. Supplementary Note 2) and the boundary states found in the spectrum of its square, H^2. To this end, we will analyze the two inequivalent lattice termination of H and map those to lattice terminations of H^2.

We start by considering the lattice termination of H given in Supplementary Eq. (8) (cf. Supplementary Figure 2A). Squaring this matrix leads to

$$H^2 = \begin{pmatrix} D^2 + TT^\dagger & \{D,T\} & 0 & \cdots \\ \{D,T^\dagger\} & D^2 + \{T,T^\dagger\} & \{D,T\} & \ddots \\ 0 & \{D,T^\dagger\} & D^2 + \{T,T^\dagger\} & \ddots \\ \vdots & \ddots & \ddots & \ddots \end{pmatrix}, \tag{18}$$

where we have used the fact that $TT = T^\dagger T^\dagger = 0$. The resulting edge termination of H^2 is shown in Supplementary Figure 2A. Importantly, the decoupled state of the boundary unit-cell appears at a lower energy. This is due to the fact that, at the edge, the intra-cell hopping is described by the matrix $D^2 + TT^\dagger$, as opposed to the matrix $D^2 + \{T,T^\dagger\}$ found in the bulk. Localized solutions of the form $|e^2\rangle = (a,b,c,0,\cdots)^T$ are found by solving the matrix equation $H^2\,|e^2\rangle = E_{e^2}\,|e^2\rangle$. This leads to two orthogonal solutions,

$$|e_1^2\rangle = (1,0,0,0,\cdots)^T \text{ and } |e_2^2\rangle = \frac{1}{\sqrt{2}}\,(0,1,-1,0,\cdots)^T , \tag{19}$$

with $E_{e_1^2} = E_{e_2^2} = 2t^2$. We note that $|e_2^2\rangle$ is a topological state related to the standard bulk-edge correspondence of the SSH model, while $|e_1^2\rangle$ appears to be originating from a nontopological inert band. Nevertheless, this distinction is basis-dependent and the appearance of the doubly-degenerate boundary states is a crucial manifestation to our model. Under the square-root operation, the boundary states of H, given in Supplementary Eq. (10), are mapped to linear combinations of $|e_1^2\rangle$ and $|e_2^2\rangle$:

$$|e_1\rangle = \frac{1}{\sqrt{2}}\left(|e_1^2\rangle + |e_2^2\rangle\right) \text{ and } |e_2\rangle = \frac{1}{\sqrt{2}}\left(|e_1^2\rangle - |e_2^2\rangle\right) . \tag{20}$$

Following the same procedure as above, we now consider the lattice termination of H given in Supplementary Eq. (11) (cf. Supplementary Figure 2B). This leads to the squared Hamiltonian

$$H^2 = \begin{pmatrix} D^2 + T^\dagger T & \{D,T^\dagger\} & 0 & \cdots \\ \{D,T\} & D^2 + \{T,T^\dagger\} & \{D,T^\dagger\} & \ddots \\ 0 & \{D,T\} & D^2 + \{T,T^\dagger\} & \ddots \\ \vdots & \ddots & \ddots & \ddots \end{pmatrix}. \tag{21}$$

The resulting edge termination of H^2, shown in Supplementary Figure 2B, displays an intra-cell coupling of the form $D^2 + T^\dagger T$. This leads to a localized solution,

$$|e_0^2\rangle = \frac{1}{\sqrt{2}} (0, 1, 1, 0, \cdots)^T , \tag{22}$$

with energy $E_{e_0^2} = 0$. Comparing with Supplementary Eq. (12), we find that the above state is mapped onto the same state of H:

$$|e_0\rangle = |e_0^2\rangle . \tag{23}$$

In summary, we have provided a relation between the boundary states found in the spectrum of H and H^2. The quantized bulk phases of H^2 lead to a standard topological bulk-edge correspondence, reminiscent of the SSH model, that, under the square root, are mapped to specific boundaries of H. This direct relationship establishes the appearance of protected boundary states in the spectrum of H, despite the fact that the bands below the gap may not have quantized topological indices.

Supplementary Note 5

In this Section, we show a general procedure with which the square root of a standard 2-band 1D TI dressed with an auxiliary state can be taken and discuss extensions to the case where the auxiliary state becomes hybridized. We start by considering non-interacting spinless electrons in a 1-dimensional lattice with three orbital degrees of freedom (d.o.f.) on each lattice site. Assuming that one orbital d.o.f. is completely decoupled from the other two, a general hybridization between the latter two can be written in the basis of 3×3 Hermitian matrices λ_i, with $i = 1, ..., 3$, i.e. the generators of the SU(2) algebra. These are the three Pauli matrices embedded in a 3-dimensional space

$$\lambda_1 = \begin{pmatrix} 0 & 0 \\ 0 & \sigma_x \end{pmatrix} , \quad \lambda_2 = \begin{pmatrix} 0 & 0 \\ 0 & \sigma_y \end{pmatrix} , \quad \lambda_3 = \begin{pmatrix} 0 & 0 \\ 0 & \sigma_z \end{pmatrix} . \tag{24}$$

where together with

$$\lambda_4 = \begin{pmatrix} \sigma_x & 0 \\ 0 & 0 \end{pmatrix} , \quad \lambda_5 = \begin{pmatrix} 0 & 0 & 1 \\ 0 & 0 & 0 \\ 1 & 0 & 0 \end{pmatrix} , \quad \lambda_6 = \begin{pmatrix} \sigma_y & 0 \\ 0 & 0 \end{pmatrix} , \quad \lambda_7 = \begin{pmatrix} 0 & 0 & -\mathrm{i} \\ 0 & 0 & 0 \\ \mathrm{i} & 0 & 0 \end{pmatrix} , \tag{25}$$

and $\lambda_8 = \mathrm{diag}(-2, 1, 1)$ are the eight Gell-Mann matrices. Thus, a general momentum space Hamiltonian is given by

$$H^2(k) = \alpha \begin{pmatrix} 1 & 0 \\ 0 & 0_{2\times 2} \end{pmatrix} + h_0 \begin{pmatrix} 0 & 0 \\ 0 & \mathbb{1}_{2\times 2} \end{pmatrix} + \sum_{i=1}^{3} h_i \lambda_i , \tag{26}$$

where $\mathbb{1}_{2\times 2} = \mathrm{diag}(1, 1)$, $0_{2\times 2} = \mathrm{diag}(0, 0)$, α is the energy at which the decoupled orbital lies, $\mathbf{h} = (h_1, h_2, h_3)$ is a 3-component real-valued vector, and $h_0 = |\mathbf{h}|$ is the energy offset from zero of the two hybridized states. The 1-dimensional topological invariant of the system is encoded in the winding of the Bloch vector $\hat{\mathbf{h}} = \frac{\mathbf{h}}{|\mathbf{h}|}$, defined as

$$w = \frac{1}{2} \int\limits_{\mathrm{BZ}} \mathrm{d}k \hat{\mathbf{h}} \times \partial_k \hat{\mathbf{h}} . \tag{27}$$

A nontrivial TI has a Bloch vector constrained to move in a specific plane in the SU(2) subspace and its trajectory, as one moves through the 1-dimensional BZ, traces a circle. This leads to a nontrivial π winding in the bulk and mid-gap states localized on the boundary [1]. Such constraint implies that one of the components of $\hat{\mathbf{h}}$ is zero and that $H^2(k)$ has a chiral-like symmetry, Θ, that anticommutes with the 2×2 subblock, $\sum_{i=1}^{3} h_i \lambda_i$. As long as the 2×2 subblock of hybridized states remains decoupled from the remaining itinerary state and Θ is not broken by any perturbation or disorder, the boundary states remain topologically protected, in similitude to standard chiral 1D TIs.

In order to define the square-root operation, we need to find a self adjoint Hamiltonian $\sqrt{H^2}(k)$ that squares to Supplementary Eq. (26). Using the properties of the $SU(3)$ algebra, the most general self adjoint Hamiltonian that squares to Supplementary Eq. (26) is given by

$$\sqrt{H^2}(k) = \sum_{i=1}^{4} d_i \lambda_{i+3} , \tag{28}$$

where $\mathbf{d} = (d_1, d_2, d_3, d_4)$ is a 4-component real-valued vector. The square of $\sqrt{H^2}(k)$, given by

$$\left(\sqrt{H^2}(k)\right)^2 = \sum_{i=1}^{4} d_i^2 \lambda_{i+3}^2 + \sum_{i<j}^{4} d_i d_j \{\lambda_{i+3}, \lambda_{j+3}\} \equiv H^2(k)\,, \tag{29}$$

defines a relation between the components of $\mathbf{d}$ and $\mathbf{h}$, namely

$$\begin{aligned} 2h_0 &= \mathbf{d}\cdot\mathbf{d} = \alpha\,, \\ h_1 &= d_1 d_3 + d_2 d_4\,, \\ h_2 &= d_1 d_4 - d_3 d_2\,, \\ h_3 &= \frac{(d_1^2 + d_2^2 - d_3^2 - d_4^2)}{2}\,, \end{aligned} \tag{30}$$

We note that the above equations do not have a unique solution. Therefore, a given $\mathbf{h}$ can have different square root realizations. In fact, any unitary transformation of $\sqrt{H^2}(k)$ has no effect on the resulting $H^2(k)$.

If additional terms proportional to the remaining Gell-Mann matrices are included in Supplementary Eq. (28) the squared model will have all three orbits hybridized. Nonetheless, if there exists a symmetry that quantizes $\gamma_{1,3}$ and γ_2 in the same way as in Supplementary Eq. (17), the resulting squared model will be a topological insulator with (in the nontrivial case) protected in-gap boundary states. For example, an onsite potential d on the a site of the AB cages introduces terms proportional to λ_i, where $i = \{4, 5, 6, 7\}$, to the squared Hamiltonian $H^2(k)$. However, such on site potential term preserves the Π-symmetry and breaks the χ-symmetry. As a result, the squared Hamiltonian at 1/3-filling has quantized winding numbers and topologically protected in-gap boundary states. In the square root model, these states are found above bands with nonquantized phases [cf. Supplementary Eq. (7)], yet remain robust against additional disorder that does not break the quantization in the squared model $H^2(k)$ (cf. Supplementary Note 6 and Supplementary Note 7).

Going back to our original model, the AB-cages at $\phi = \pi$, we find that $H^2(k)$ has $h_1 = 0$ and, therefore, the subblock $\sum_{i=1}^{3} h_i \lambda_i$ has a chiral symmetry given by $\Theta = \mathrm{e}^{\mathrm{i}\frac{\pi}{2}\lambda_1}$, that quantizes the topological phases to

$$\Theta: \qquad \gamma_{1,3} \in \{0, \pi\} \qquad \text{and} \qquad \gamma_2 \in \{0, \pi\}\,, \tag{31}$$

where $\gamma_{1,3}$ denotes the phase of the degenerate subspace, and γ_2 is the phase of the single band at zero energy. Such symmetry is preserved when the AB-cages model is of the form of Supplementary Eq. (28), i.e., there are no additional terms proportional to the remaining Gell-Mann matrices, and the hopping strength between sites is equal. In this case, the topological boundary states appear in the middle of the gap and are pinned to their energy due to the chiral symmetry Θ.

For completeness, we note that different gauge choices of the AB-cages lead to an equivalent squared model. This has to do with the fact that transformations which preserve the boundary conditions have vanishing contribution to the topological invariant. Therefore, the Bloch vector, $\mathbf{h}$, will still correspond to a nontrivial TI that winds around a circle as we go around the 1-dimensional BZ. Conversely, the two alternative unit-cell choices of the AB-cages that we did not consider here lead to a Bloch vector $\mathbf{h}$ that does not correspond to a standard TI.

Supplementary Note 6

In this section we discuss the interplay of an onsite potential with the Π-preserving term. Adding an onsite potential of the form

$$H(k) = \begin{pmatrix} d & t + t\mathrm{e}^{-\mathrm{i}k} & t\mathrm{e}^{-\mathrm{i}\phi} + t\mathrm{e}^{-\mathrm{i}k} \\ t + t\mathrm{e}^{\mathrm{i}k} & 0 & 0 \\ t\mathrm{e}^{\mathrm{i}\phi} + t\mathrm{e}^{\mathrm{i}k} & 0 & 0 \end{pmatrix}, \tag{32}$$

leads to scrambling of winding phases γ_1 and γ_3, while γ_2 remains quantized, see Supplementary Figure 4 [cf. Supplementary Eq. (7)]. Importantly, the boundary states given in Supplementary Eq. (10) remain solutions of the Hamiltonian but with modified energies

$$E_{e_1} = \frac{1}{2}\left(d + \sqrt{d^2 + 8}\right) \text{ and } E_{e_2} = \frac{1}{2}\left(d - \sqrt{d^2 + 8}\right)\,, \tag{33}$$

while the boundary state given in Supplementary Eq. (12) remains pinned to zero energy, i.e., it does not manifest as a topological in-gap state.

The robustness of the boundary states against additional disorder (cf. Supplementary Figs. 5 and 6) stems from the fact that the Π-transformation [cf. Supplementary Eq. (6)] remains a symmetry of both $H(k)$ and $H^2(k)$, while the χ-symmetry is broken. Since the quantization of the Wilzcek-Zee phases persists under the addition of this term [cf. Supplementary Eq. (17)], the localization of the boundary states is unaffected (cf. Supplementary Note 7 and Supplementary Figs. 5 and 6).

Supplementary Note 7

One of the fundamental aspects of topological insulators is the robustness of their boundary states against disorder that does not break the symmetry that quantizes the topological invariant. Such a property is paramount towards realizing fault-tolerant and impurity-insensitive devices. In this Section, we investigate the robustness of the boundary states found in the AB-cages against different kinds of disorder.

The topological robustness of boundary states is commonly quantified by calculating the energy offset of the topological state as well as its localization length over many disorder realizations. For a comprehensive analysis, we study, on one hand, (a) disorder that on average preserves both symmetries, Π and χ, and on the other hand (b) terms that on average break each of these symmetries individually and jointly and analyze the impact of additional disorder on top of the symmetry-broken model. The analyzed quantities are the averaged mean squared difference of the boundary state energy in the presence of disorder, β_{edge}, from the energy of the undisturbed system, β_0 (i.e. when $\sigma = 0$) and the second moment of the corresponding eigenstates. The former shows the robustness of the energy while the latter quantifies the localization of the boundary state and is related to the localization length. The disorder is assumed to be of Gaussian shape with standard deviation σ and a vanishing mean for case (a) or a mean equal to the coupling strength t for the case (b). Each studied disorder strength was average over 10000 realizations on a lattice with 99 sites.

In order to analyze the ensuing impact of symmetry-breaking terms and disorder, we consider three different types, namely, potential terms d on sites a, and complex coupling terms α on the hopping amplitudes between sites b and c

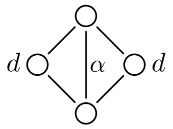

(34)

The corresponding symmetries that survive under the addition of such terms are

$$\begin{array}{ccc} \text{Term} & \text{Preserved} & \text{Broken} \\ d & \Pi & \chi\,, \\ \mathrm{Re}(\alpha) & \chi & \Pi\,. \end{array} \tag{35}$$

The results are displayed in Supplementary Figs. 5 and 6 for vanishing mean and non-vanishing mean disorder realizations, respectively. A Π-preserving, but χ-breaking, disorder is implemented by adding a real detuning term d that on average is either $\langle d\rangle = 0$ or t (see black curve in Supplementary Figs. 5 and 6). A χ-preserving, but Π-breaking, disorder is implemented by adding a real coupling term α that on average is either $\langle\alpha\rangle = 0$ or t (see red curve in Supplementary Figs. 5 and 6). A general disorder that breaks all symmetries is implemented by combining a complex coupling α and a detuning d (see blue curve in Supplementary Figs. 5 and 6 for $\langle\alpha\rangle = \langle d\rangle = 0$ and $\mathrm{Re}(\langle\alpha\rangle) = \mathrm{Im}(\langle\alpha\rangle) = \langle d\rangle = t$, respectively). We illustrate the robustness of the edge state energies more clearly, by splitting the plot into two regions with an energy offset that is bigger (red) or smaller (green) than $(\sigma/t)^2$, since $(\sigma/t)^2$ would correspond to a an energy offset proportional to the disorder strength.

We find that, indeed, in case of zero average disorder, the boundary modes remain robust in both energy and localization length against a symmetry-preserving disorder and as long as the disorder strength is not large enough to mix the boundary states with the nearest bulk band. In the case of either Π- or χ-preserving disorder we find that the energy offset is always in the green region (see Supplementary Figure 5a), while the wavefunctions remain highly localized within a unit cell (see Supplementary Figure 5b). In contrast, the boundary states do not show any protection against a general disorder, neither in energy, since we find that the energy offset is mostly in the red region (see Supplementary Figure 5a), nor localization, even though the symmetries are preserved on average. For nonzero average disorder (i.e. adding a nonzero symmetry-breaking term to the Hamiltonian and applying an additional disorder), the boundary states still appear, but are now pinned to a different energy, other than $\pm\sqrt{2}t$. This is due to the fact that the square-root map between the effective-SSH and the AB-cages model no longer holds. Nevertheless, the remaining unbroken symmetries in the modified AB-cages model still provide protected boundary states since the corresponding squared model is again a nontrivial TI (see Supplementary Figure 6).

Supplementary Note 8

In this Section, we provide additional information on the effective negative hopping between two main waveguides when an auxiliary waveguide is introduced between them. The auxiliary waveguide is strongly detuned from the main waveguides and, hence, inhibits direct coupling between them. Moreover, it is generating an effective negative hopping between the main waveguides through a carefully-tuned second-order tunneling process, i.e., this approach allows us to effectively flip the sign of the coupling amplitude between them. Embedding such a negative hopping amplitude inside the square structure of our system realizes an artificial gauge field of a π flux for the photons, i.e., when a particle goes around the square it collects the negative sign which is equivalent to a $e^{i\pi}$ phase.

For completeness, we provide here a more detailed description of such negative hopping generation (cf. also Ref. [2]). We start by considering two main waveguides with a small detuning δ, coupled to each other via the overlap of evanescence modes with a neighbouring auxiliary waveguide with detuning Δ. Using the tight-binding approximation, the equations of motions for the electric-field amplitude in the three waveguides, a, b and c, are given by

$$i\partial_z \begin{pmatrix} a \\ b \\ c \end{pmatrix} = \begin{pmatrix} \delta & \kappa & 0 \\ \kappa & \Delta & \kappa \\ 0 & \kappa & \delta \end{pmatrix} \begin{pmatrix} a \\ b \\ c \end{pmatrix},$$

where κ is the coupling strength. In order to engineer the negative coupling between the two main waveguides, a and c, we choose

$$\Delta = \frac{\kappa^2 - \delta^2}{\delta},$$

and find the eigenvectors and eigenvalues

$$\mathbf{u}_1 = \begin{pmatrix} 1 \\ 0 \\ -1 \end{pmatrix} \qquad \beta_1 = \delta$$

$$\mathbf{u}_2 = \begin{pmatrix} 1 \\ -2\dfrac{\delta}{\kappa} \\ 1 \end{pmatrix} \qquad \beta_2 = -\delta$$

$$\mathbf{u}_3 = \begin{pmatrix} 1 \\ \kappa/\delta \\ 1 \end{pmatrix} \qquad \beta_3 = \delta + \frac{\kappa^2}{\delta}.$$

In the limit where $\delta \ll \kappa$ the eigenvectors can be approximated by

$$\tilde{\mathbf{u}}_1 = \begin{pmatrix} 1 \\ 0 \\ -1 \end{pmatrix} \qquad \tilde{\mathbf{u}}_2 \approx \begin{pmatrix} 1 \\ 0 \\ 1 \end{pmatrix} \qquad \tilde{\mathbf{u}}_3 \approx \begin{pmatrix} 0 \\ \kappa/\delta \\ 0 \end{pmatrix},$$

and the eigenvalues by

$$\beta_1 = \delta\,, \quad \beta_2 = -\delta\,, \quad \beta_3 \approx \frac{\kappa^2}{\delta}\,,$$

respectively. Since $\tilde{\mathbf{u}}_3$ is decoupled from the remaining two states and its eigenvalue is much larger, its dynamics will not contribute much to the evolution of amplitudes a and c, hence it can be traced out. The effective model obtained after tracing out the auxiliary waveguide b is equivalent to having two waveguides that are coupled with a negative amplitude, i.e.,

$$\mathrm{i}\partial_z \begin{pmatrix} a \\ c \end{pmatrix} = \begin{pmatrix} 0 & -\delta \\ -\delta & 0 \end{pmatrix} \begin{pmatrix} a \\ c \end{pmatrix} .$$

One can see by direct calculation that the eigenvalues and eigenvectors of the above Hamiltonian are equivalent to $\tilde{\mathbf{u}}_1$ and $\tilde{\mathbf{u}}_3$ with eigenvalues δ and $-\delta$ respectively. Embedding such an effective model inside the square structure of our AB-cages system and carefully choosing the detuning δ such that it matches the coupling strength between waveguides on the other edges of the square, realizes an artificial gauge field with π flux threading each square.

Supplementary Note 9

In this section we discuss the propagation without flux. In order to demonstrate that the edge states, as well as the complete localisation of the bulk states originate from the flux of $\phi = \pi$ we also fabricated a lattice without flux and measured the resulting intensities (see Supplementary Figure 7). It can clearly be seen that for the case of vanishing flux no localisation occurs when exciting the bulk (see Supplementary Figure 7a-b). When exciting the edge of the lattice there is basically no light residing, which confirms that there is no edge state present (see Supplementary Figure 7c).

SUPPLEMENTARY REFERENCES

---

[1] Resta, R. & Vanderbilt, D. *Physics of Ferroelectrics.* (Springer, Berlin, 2007).
[2] Keil, R. et al. Universal sign control of coupling in tight-binding lattices. *Physical Review Letters* **116**, 213901-1–213901-5 (2016).

8.4 Optimal design strategy for non-Abelian geometric phases using Abelian gauge fields based on quantum metric

M. Kremer, L. Teuber, A. Szameit, and S. Scheel *Optimal design strategy for non-Abelian geometric phases using Abelian gauge fields based on quantum metric*, Physical Review Research **1**, 033117 (2019).

DOI: `https://doi.org/10.1103/PhysRevResearch.1.033117`

Author Contributions:

Mark Kremer	conceptual design, sample design based on calculations from L. T., experimental determination of the sample parameters, sample fabrication, data acquisition, data evaluation, figure art, preparation of initial manuscript draft
Lucas Teuber	conceptual design, optimisation with the quantum metric, based on parameters retrieved by measurements from M. K., calculation of the Wilson loops based on experimental data, theoretical explanations in the initial draft, preparation of initial draft
Stefan Scheel	preparation of the manuscript, supervision
Alexander Szameit	preparation of the manuscript, supervision

Note: The shared co-first authorship of Lucas Teuber and Mark Kremer is based on the distinct contributions of both authors. The theoretical considerations are mainly the work of Lucas Teuber, while the experimental realisation is mainly the work of Mark Kremer.

PHYSICAL REVIEW RESEARCH **1**, 033117 (2019)

Optimal design strategy for non-Abelian geometric phases using Abelian gauge fields based on quantum metric

Mark Kremer,[*] Lucas Teuber,[*] Alexander Szameit,[†] and Stefan Scheel
Institut für Physik, Universität Rostock, Albert-Einstein-Straße 23-24, D-18059 Rostock, Germany

(Received 24 January 2019; published 20 November 2019)

Geometric phases, which are ubiquitous in quantum mechanics, are commonly more than only scalar quantities. Indeed, often they are matrix-valued objects that are connected with non-Abelian geometries. Here, we show how generalized non-Abelian geometric phases can be realized using electromagnetic waves traveling through coupled photonic waveguide structures. The waveguides implement an effective Hamiltonian possessing a degenerate dark subspace in which an adiabatic evolution can occur. The associated quantum metric induces the notion of a geodesic that defines the optimal adiabatic evolution. We exemplify the non-Abelian evolution of an Abelian gauge field by a Wilson loop.

DOI: 10.1103/PhysRevResearch.1.033117

I. INTRODUCTION

Geometry and quantum mechanics are inextricably linked. Whenever a quantum system evolves in Hilbert space, its wave function acquires a phase that solely depends on the path the quantum system has taken. This concept of geometric phases was introduced by Berry [1] who pointed out that there are instances in which these emerging phase factors cannot be removed by some gauge transformation. A famous example is the Aharonov-Bohm effect [2] in which the wave function of a charged particle traveling in a loop around a solenoidal magnetic field acquires a phase proportional to the flux through the surface enclosed by the loop, i.e., a line integral over the (Abelian) vector potential. Here, the emerging (Abelian) phase is merely a complex number.

However, any quantum system with degenerate energy levels possesses a far richer structure as matrix-valued geometric phases [3], known as non-Abelian holonomies. These can occur as soon as the emerging phase depends on the order of consecutive paths. In contrast to the vector potential in the Aharonov-Bohm scenario, a non-Abelian gauge field is responsible for the appearance of these matrix-valued phases. Such phases are crucial for topological quantum computation [4,5], non-Abelian anyon statistics [6], and the quantum simulation of Yang-Mills theories. Non-Abelian synthetic gauge fields are usually realized in systems where coupled energy levels naturally lead to the required degeneracy, such as in cold atomic samples [7] and artificial atoms in superconducting circuits [8]. In the case of electromagnetic fields, due to their intrinsic Abelian nature, the required degeneracy is more intricate to design. One successful scheme utilized the spin-orbit coupling of polarized light in asymmetric microcavities [9].

In our paper, we focus on a different degree of freedom and synthesize a non-Abelian geometric phase by implementing adiabatic population transfer [10] of light. We employ an integrated photonic structure possessing dark states in which a non-Abelian geometric phase associated with a U(2) group transformation is realized. The quantum metric spanned by the subspace of the dark states induces a geodesic that defines the optimal adiabatic evolution of these non-Abelian phases.

II. THEORY

Gauge fields naturally arise in the context of field theories when demanding the invariance of a field under some transformation. Invariance under multiplication by a scalar phase factor leads to the concept of Abelian gauge fields, such as the four-vector potential of electromagnetism with commuting components. In contrast, matrix-valued phases entail non-Abelian gauge fields where the commutator of the individual components involves the structure constants of the underlying Lie algebra. Famous examples are Yang-Mills theories of particle physics [11].

A wave packet evolving in the presence of a gauge field acquires a geometric phase. For Abelian gauge fields, this is the famous Berry-Pancharatnam phase [1,12]. The non-Abelian generalization is known as the Wilson loop,

$$W_{\mathcal{C}} = \mathrm{Tr}\left[\mathcal{P}\exp\left(-\oint_{\mathcal{C}} \mathbf{A}_\nu dx^\nu\right)\right], \qquad (1)$$

which is the trace of the path-ordered ($\mathcal{P}$) exponential of the non-Abelian gauge field $\mathbf{A}_\nu$ [13]. Our system is a nontrivial collection of interacting Abelian subsystems and, thus, non-Abelian, being characterized by a Wilson loop $W_{\mathcal{C}} < 2$ [14,15].

---

[*] These authors contributed equally to this work.
[†] alexander.szameit@uni-rostock.de

Published by the American Physical Society under the terms of the Creative Commons Attribution 4.0 International license. Further distribution of this work must maintain attribution to the author(s) and the published article's title, journal citation, and DOI.

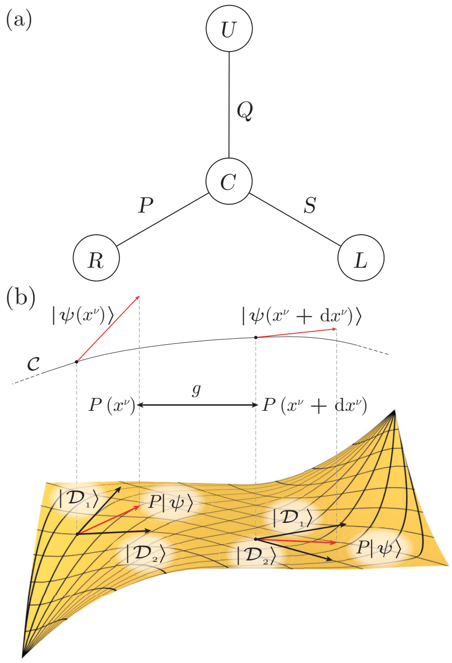

FIG. 1. (a) Scheme of the four-waveguide system. (b) Visualization of changing the dark subspace projector along curve $\mathcal{C}$. The change in the dark subspace projectors of the system is given by the quantum metric $\boldsymbol{g}$.

In order to implement this concept, one seemingly requires a non-Abelian gauge field. However, this is not necessary as a non-Abelian structure naturally appears whenever the evolution of a quantum system is confined to a degenerate subspace of some Hamiltonian [3]. As a consequence, generating non-Abelian geometric phases is not connected to the presence of a non-Abelian gauge field but to the existence of a degenerate subspace.

In our paper, we consider the system sketched in Fig. 1 that consists of four potential wells C, U, R, and L that are coupled with time-dependent hopping constants Q, S, and P. The Schrödinger equation for the field amplitudes a_L, a_U, a_R, and a_C in the individual wells reads, therefore,

$$i\partial_t \begin{pmatrix} a_\mathrm{L} \\ a_\mathrm{R} \\ a_\mathrm{U} \\ a_\mathrm{C} \end{pmatrix} = \begin{pmatrix} 0 & 0 & 0 & S \\ 0 & 0 & 0 & P \\ 0 & 0 & 0 & Q \\ S & P & Q & 0 \end{pmatrix} \begin{pmatrix} a_\mathrm{L} \\ a_\mathrm{R} \\ a_\mathrm{U} \\ a_\mathrm{C} \end{pmatrix}. \tag{2}$$

This Hamiltonian supports two dark states with zero eigenvalues,

$$|\mathcal{D}_1\rangle = \sin\theta|w_\mathrm{L}\rangle - \cos\theta|w_\mathrm{R}\rangle, \tag{3}$$

$$|\mathcal{D}_2\rangle = \cos\theta\,\sin\phi|w_\mathrm{L}\rangle + \sin\theta\,\sin\phi|w_\mathrm{R}\rangle - \cos\phi|w_\mathrm{U}\rangle, \tag{4}$$

where $|w_{\mathrm{U,R,L}}\rangle$ are the eigenmodes of the potential wells U, R, L, respectively, with the angle parametrization $\theta = \arctan(P/S)$ and $\phi = \arctan(Q/\sqrt{S^2+P^2})$. Notably, they do not involve the eigenstate $|w_\mathrm{C}\rangle$ to which all other states are coupled. These dark states span a (dark) subspace in which the adiabatic evolution of a wave function along a closed path can be described by a non-Abelian geometric phase (1) with the gauge field,

$$(\mathbf{A}_\nu)_{ki} = \langle\mathcal{D}_k|\frac{\partial}{\partial x^\nu}|\mathcal{D}_i\rangle \tag{5}$$

written in the coordinates $\{x^\nu\} = \{S, P, Q\}$. In the context of adiabatic evolution, the Hamiltonian (2) is a generalization [10] of the stimulated Raman adiabatic passage (STIRAP) protocol [16]. What is required is to ensure adiabaticity of the evolution.

Interestingly, adiabatic transport is equivalent to parallel transport in a curved (metric) space via vanishing covariant derivative [17], i.e., along a geodesic defined in our parameter manifold. The quantum metric $g_{\mu\nu} = \mathrm{Tr}(\partial_\mu P\,\partial_\nu P)$ is constructed [18,19] from infinitesimal changes of the dark subspace projector $P(x^\nu) = \sum_i |\mathcal{D}_i(x^\nu)\rangle\langle\mathcal{D}_i(x^\nu)|$ via

$$\|dP\|^2 = \mathrm{Tr}(\partial_\mu P\,\partial_\nu P)dx^\mu dx^\nu = g_{\mu\nu}dx^\mu dx^\nu$$

[see Fig. 1(b)]. This is the real part of a quantity known as the quantum metric tensor [17–20], whose imaginary part is the field strength tensor of the (non-Abelian) gauge field $\mathbf{F}_{\mu\nu} = \partial_\mu\mathbf{A}_\nu - \partial_\nu\mathbf{A}_\mu - [\mathbf{A}_\mu, \mathbf{A}_\nu]$.

The coordinates $x^\nu(z)$ in parameter space themselves are a function of the propagation distance z. The quantum metric $g_{\mu\nu}$ defines a path length (action) along the curve $\mathcal{C}$ in the parameter manifold from the input facet z_i to the output facet z_f,

$$L = \int_{z_\mathrm{i}}^{z_\mathrm{f}} \sqrt{g_{\mu\nu}\partial_z x^\mu \partial_z x^\nu}\,dz. \tag{6}$$

The principle of least action defines a geodesic that describes the evolution with the least diabatic error through parameter space [18]. As a consequence, the notion of adiabaticity is intimately connected to the concept of the quantum metric. This defines the optimal strategy for determining the time dependence of the parameters for adiabatic evolution in parameter space. Starting from the desire to realize non-Abelian geometric phases, one first has to find a Hamiltonian with a degenerate subspace [3] on which a metric can be defined. The geodesic induced by this metric then specifies the variation of the parameters of the Hamiltonian such that the evolution through parameter space occurs with the least diabatic error. A closed path along the geodesic in parameter space then necessarily results in a non-Abelian geometric phase. In the case of the tripod Hamiltonian with the three real couplings S, P, and Q, we find for the quantum metric,

$$\mathbf{g} = 2\,\mathrm{diag}[1, \cos^2(\phi)]. \tag{7}$$

Note that the metric is two-dimensional since the mixing angles θ and ϕ are the relevant parameters here. This is because the normalization of the dark states makes one parameter degree of S, P, and Q obsolete.

In an actual implementation, however, the experimental constraints might limit the possible curves that can be realized with the result that we might not be able to obtain perfect geodesics. Nevertheless, L is a possible measure for the quality of a certain curve/parameter variation and may be used for optimization, i.e., helps to find the curve with the least diabatic error/path length for given constraints (such as pulse shape, total propagation length, etc.). In our experimental implementation, we minimize L under the constraint of a given Gaussian pulse shape with a limited number of parameters determining the exact shape. Minimizing L over these shape parameters provides the curves with the least diabatic error for a given total length $z_f - z_i$. This idea was used to obtain optimized coupling variations when designing the waveguide system for different gauge fields or Wilson loops. We furthermore compared the path-length optimization with the deviations from a perfect adiabatic evolution to justify our approach. For details see Appendices D and F.

III. EXPERIMENT

In order to implement our findings, we employ a photonic platform manifested in the form of integrated coupled waveguides. Using the analogy between the quantum evolution of a wave function and the propagation of an optical wave packet in the paraxial approximation [21], the quantum wells in our structure can be replaced by optical waveguides. The temporal evolution of the light amplitudes in those waveguides is governed by Eq. (2) with the sole difference that the time evolution is replaced by the evolution along the waveguides described by the spatial coordinate z [see Fig. 2(a)]. Our design protocol yields a spatial evolution of the intersite hoppings Q, S, and P with an example depicted in Fig. 2(b). The hoppings S and P resemble the Stokes and pump pulses of Gaussian shape in the counterintuitive sequence known from STIRAP [16] with Q as an additional constant coupling. The evolution of the parameters in parameter space is chosen to form a closed-loop trajectory as shown in Fig. 2(c). Therefore, this evolution results in a geometric phase.

In the following, we will describe the measurement protocol for retrieving the Wilson loop. From the choice of the temporal evolution of the parameters S and P, we have, at the input facet z_i and the output facet z_f, the relations $P(z_i)/S(z_i) \simeq 0 \simeq S(z_f)/P(z_f)$. Hence, the dark states at both facets simply become

$$\begin{matrix} |\mathcal{D}_1(z_i)\rangle\rangle = -|w_R\rangle & & |\mathcal{D}_1(z_f)\rangle\rangle = |w_L\rangle, \\ & \rightarrow & \\ |\mathcal{D}_2(z_i)\rangle\rangle = |w_L\rangle & & |\mathcal{D}_2(z_f)\rangle\rangle = |w_R\rangle. \end{matrix}$$

As a consequence, launching light into the waveguides L and R excites only the dark states of the system. Also, measuring the light intensity emanating from the waveguides L and R at the output facet provides the information about the population transfer between the dark states. An initial superposition of the dark states evolves according to a unitary evolution $\mathcal{U}$. As we show in Appendix C, the elements of this unitary matrix can be expressed in terms of the amplitudes of the dark states at the input and output facet. Moreover, the value of the Wilson loop is given by $W_\mathcal{C} = \mathrm{Tr}[\mathcal{U}]$. Measuring the field intensities yields the absolute values of the matrix elements $|\mathcal{U}_{ki}|$, and, hence, the absolute value $|W_\mathcal{C}|$.

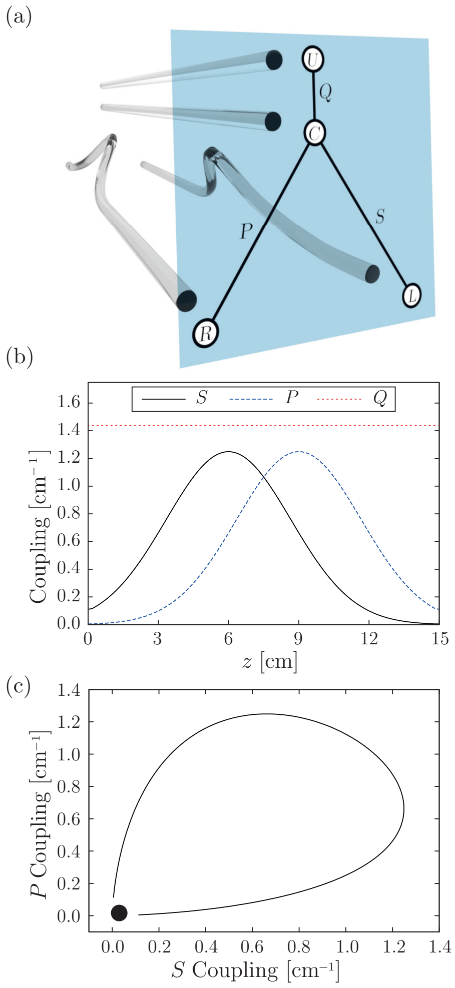

FIG. 2. (a) Three-dimensional rendering of the waveguides for one realization. (b) Coupling variation along propagating distance z. (c) Curve in the parameter manifold $\{S, P, Q\}$ (Q = const).

For the fabrication of our samples, we use the femtosecond laser writing technique [22]. Details of the fabrication are given. We realize several structures with varying temporal profiles of the coupling parameters S and P, resulting in different values of the Wilson loop. An example of the evolution along the waveguides recorded by fluorescence microscopy is shown in Fig. 3(a). Launching light into waveguide L excites only the dark state $|\mathcal{D}_2(z_i)\rangle\rangle$. During the evolution, the light is coupled to the waveguides R and U without ever populating C [see Fig. 3(b)]. Hence, the evolution indeed remains in the dark subspace for all times as required for adiabaticity.

For retrieving the elements of $\mathcal{U}$, we measure the intensities at the output facet. A representative example is shown in Fig. 4(a). In our experiments, we realized Wilson loops by implementing three different sets of parameters. The results

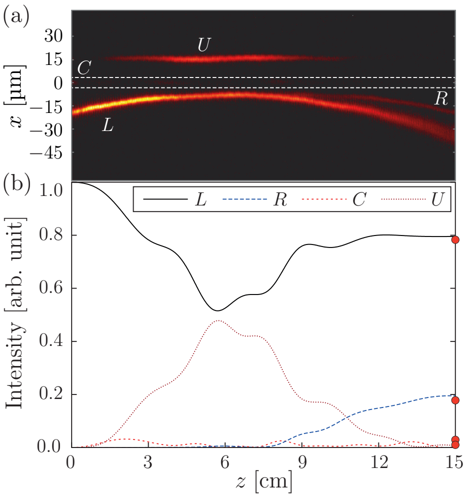

FIG. 3. (a) Experimentally measured fluorescence signal which is proportional to the intensity in the waveguides. The waveguide L was excited, thus, the second dark state. The central waveguide C is located between the dashed lines, highlighting the almost vanishing intensity. (b) Theoretically predicted intensity from the coupled-mode theory using Eq. (2). The red dots at the end facet are the experimentally measured intensities (compare Fig. 4).

are summarized in Table I where the theoretical predictions and the experimental results are shown to agree well. In all three cases, the (absolute) value of the Wilson loop is well above 0, thus, proving the non-Abelian character of the underlying contour.

In order to prove that waveguide C is part of the full eigenspace, we specifically launched light into C and excited states in the bright subspace that extend over all waveguides [see Fig. 4(b)]. From our measurements, we find that, at the output facet, all waveguides are bright such that one can conclude that, indeed, waveguide C has to reside within the bright subspace.

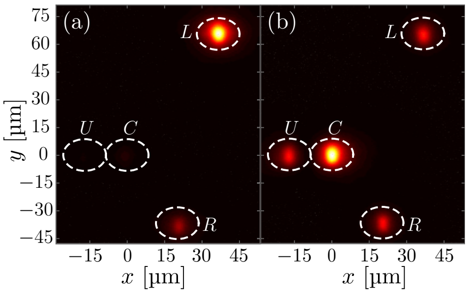

FIG. 4. (a) Measured intensity distribution for dark-state excitation. This is for the same set of parameters as seen in Fig. 3. The result is clearly restricted to the dark subspace. (b) Measured intensity distribution for bright-state distribution. The waveguides C and U and with that the bright states are dominantly excited.

TABLE I. Experimental results and corresponding theoretical Wilson loops for three different coupling variations. For a detailed description of the used parameters and pulse shapes see Appendix E.

$\lvert W_C^{\mathrm{theo}}\rvert$	$\lvert W_C^{\mathrm{exp}}\rvert$
0.88	0.87
0.97	1.00
1.07	1.13

IV. CONCLUSION

We employed evanescently coupled photonic waveguides to simulate the action of a non-Abelian gauge field on the dark subspace of the associated Hamiltonian. The non-Abelian nature of the process was verified by measurement of the gauge invariant Wilson loop. As the present implementation of the Wilson loop requires an adiabatic evolution within the dark subspace, the quantum metric is the appropriate tool to quantify the diabatic error.

Our results lay the foundations for the simulation of non-Abelian gauge fields using Abelian systems, such as sound waves, matter waves or, in our case, light. In particular, within this construction principle, the implementation of non-Abelian gauge fields that transform under SU(N) could be realized with $N+2$ coupled sites containing a N-dimensional dark subspace. Moreover, the use of geodesics of the quantum metric to quantify adiabaticity sheds new light on the optimization of all STIRAP-type processes.

The implementation of non-Abelian Abelian gauge fields prompts various important questions. One of them concerns the simulation of lattice gauge field theories, such as Yang-Mills theories where Wilson loops are the observable quantities. In another context, using nonclassical light, our proposed setting is conducive to realize holonomic quantum operations as quantum logical gates can be defined as the action of non-Abelian geometric phases on the space of degenerate states, i.e., the dark subspace [5]. Finally, the definition of a quantum metric induced by parametric changes of the waveguide couplings allows to study the evolution of a quantum system on curved manifolds.

ACKNOWLEDGMENTS

The authors would like to thank C. Otto for preparing the high-quality fused silica samples used in all our experiments. The authors acknowledge funding from the Deutsche Forschungsgemeinschaft (Grants No. SCHE 612/6-1, No. SZ 276/20-1, No. SZ 276/15-1, No. BL 574/13-1, and No. SZ 276/9-2) and the Krupp von Bohlen and Halbach Foundations.

APPENDIX A: MATERIALS AND METHODS

The waveguides were fabricated in 15-cm fused silica glass (Corning 7980) samples by the femtosecond laser writing method 20. We used pulses created by a Coherent RegA seeded with a Mira 900 with an energy of 310 nJ at 800 nm and 100 kHz. An Aerotech ALS 130 together with a microscope objective (0.35 numerical aperture) was used to focus the beam into the moving sample. Moving it with a speed of about 100 mm min^{-1} lead to a change in the refractive index at the focal point of around 7×10^{-4}. The created waveguides have a mode field diameter of about $10.4\times8\ \mu\text{m}^2$ at 632.8 nm. Propagation losses and birefringence were estimated at 0.2 dB cm^{-1} and 10^{-7}, respectively. The minimal and maximal waveguide distances are 15.5 and 71.1 μm, respectively. For the direct monitoring of the light propagation in our samples, the fluorescence microscopy technique [22] was used. During the writing process, a formation of nonbridging oxygen hole color centers occurs, resulting in a homogeneous distribution of these color centers along the fabricated waveguides. With the light of a helium neon laser at $\lambda = 633$ nm, the nonbridging oxygen hole color centers are excited, and the resulting fluorescence ($\lambda = 650$ nm) can be observed using a CCD camera combined with an appropriate narrow linewidth filter. The light intensity distribution at the output facet of the array is imaged onto a CCD camera by using a $10\times$ objective.

APPENDIX B: DERIVATION OF GAUGE FIELD

A quantum state $|\psi\rangle$ initially prepared at $z = z_\text{i}$ in the $N_\mathcal{D}$-dimensional dark subspace, i.e.,

$$|\psi(z_\text{i})\rangle = \sum_{j=1}^{N_\mathcal{D}} c_j |\mathcal{D}_j(z_\text{i})\rangle \tag{B1}$$

stays in this subspace if the evolution is perfectly adiabatic. At a later point $z > z_\text{i}$, the state is, thus, given by applying to the initial state a unitary matrix $\mathcal{U} \in U(N_\mathcal{D})$,

$$|\psi(z)\rangle = \mathcal{U}(z, z_\text{i})|\psi(z_\text{i})\rangle = \sum_{i,j=1}^{N_\mathcal{D}} \mathcal{U}_{ij} c_j |\mathcal{D}_i(z)\rangle \tag{B2}$$

given by

$$\mathcal{U}(z, z_\text{i}) = \sum_{i,j=1}^{N_\mathcal{D}} \mathcal{U}_{ij} |\mathcal{D}_i(z)\rangle\langle\mathcal{D}_j(z_\text{i})|. \tag{B3}$$

Hence, for initial states with $c_j = \delta_{jn}$, i.e., initially exciting $|\mathcal{D}_n(z_\text{i})\rangle$ and measuring $|\mathcal{D}_m(z_\text{f})\rangle$ yields the element $\mathcal{U}_{mn}$.

Inserting Eq. (B2) into the Schrödinger or paraxial wave equation and acknowledging the fact that the state stays in the dark subspace with zero eigenvalue leads to

$$\partial_z|\psi(z)\rangle = \sum_{i,j=1}^{N_\mathcal{D}} c_j[\partial_z\mathcal{U}_{ij}|\mathcal{D}_i(z)\rangle + \mathcal{U}_{ij}\partial_z|\mathcal{D}_i(z)\rangle] = 0. \tag{B4}$$

The second term on the rightmost side is due to the apparent change in the dark states, i.e., the basis vectors of the dark subspace. When a state is, thus, infinitesimally transported along a curve, it is not only the state that changes in its original basis, but also the basis itself. This is directly analogous to the transport of a vector in curved space where the additional derivative of the basis vectors gives the information of how to *connect* vectors along infinitesimal steps of the curve. In differential geometry, this connection is described by the well-known Christoffel symbols, whereas in case of the dark-state dynamics, this information is encoded in the gauge field. Thus, Eq. (B4) not only describes the adiabatic transport of state $|\psi(z)\rangle$ in the dark subspace, but also can be interpreted geometrically as a parallel transport where the total change is zero.

The emergence of a gauge field from the change in basis occurring in Eq. (B4) can be understood as follows. Since Eq. (B4) has to hold for arbitrary input states, i.e., $\forall\, c_j$, we have

$$\sum_{i=1}^{N_\mathcal{D}} \partial_z\mathcal{U}_{ij}|\mathcal{D}_i(z)\rangle = -\sum_{i=1}^{N_\mathcal{D}} \mathcal{U}_{ij}\partial_z|\mathcal{D}_i(z)\rangle. \tag{B5}$$

Applying $\langle\mathcal{D}_k(z)|$ from the left results in

$$\partial_z\mathcal{U}_{kj} = -\sum_{i=1}^{N_\mathcal{D}} A_{ki}\mathcal{U}_{ij}, \tag{B6}$$

where

$$A_{ki} = \langle\mathcal{D}_k(z)|\partial_z|\mathcal{D}_i(z)\rangle. \tag{B7}$$

As a non-Abelian gauge field, the $(N_\mathcal{D}\times N_\mathcal{D})$-matrix $\mathbf{A}$ has to fulfill the proper transformation behavior under change in basis,

$$|\tilde{\mathcal{D}}_i\rangle = \sum_j U_{ij}|\mathcal{D}_j\rangle, \tag{B8}$$

with a unitary matrix $\mathbf{U}$. The new gauge field is then,

$$\tilde{A}_{ki} = \sum_{mj} A_{mj}U^*_{km}U_{ij} + \sum_m U^*_{km}\partial_z U_{im}, \tag{B9}$$

$$\tilde{\mathbf{A}} = \mathbf{U}\mathbf{A}\mathbf{U}^{-1} + (\partial_z\mathbf{U})\mathbf{U}^{-1}, \tag{B10}$$

which is a properly transformed gauge field [3].

A general solution to Eq. (B6) up to $z = z_\text{f}$ is the path-ordered integral,

$$\mathcal{U}(z_\text{f}) = \mathcal{P}\exp\left(-\int_{z_\text{i}}^{z_\text{f}} \mathbf{A}\, dz\right). \tag{B11}$$

Since the system parameters depend on the propagation distance z, we have a curve $\mathcal{C}\colon (z_\text{i}, z_\text{f}) \rightarrow \mathcal{M}$ in the parameter manifold $\mathcal{M}$ with coordinates $\{x^\nu\}$. By using the total derivative, we find

$$(\mathbf{A}_\nu)_{ki} = \langle\mathcal{D}_k|\frac{\partial}{\partial x^\nu}|\mathcal{D}_i\rangle, \tag{B12}$$

where $\mathbf{A}_\nu$'s are the matrix-valued components of the gauge field expressed in the parameters of $\mathcal{M}$. Subsequently, for a closed curve $\mathcal{C}$ we get

$$\mathcal{U} = \mathcal{P}\exp\left(-\oint_\mathcal{C} \mathbf{A}_\nu dx^\nu\right). \tag{B13}$$

This can be characterized by the related gauge-invariant quantity, the so-called Wilson loop [13],

$$W_\mathcal{C} = \text{Tr}\,\mathcal{U}. \tag{B14}$$

APPENDIX C: GAUGE FIELD OF TRIPOD STIRAP

Choosing the coordinates $\{x^\nu\} = \{S, P, Q\}$ that parametrize the tripod STIRAP system, cf. Fig. 1(a), the dark states take the form

$$|\mathcal{D}_1\rangle = P/(\sqrt{S^2+P^2})|w_\mathrm{L}\rangle - S/(\sqrt{S^2+P^2})|w_\mathrm{R}\rangle, \tag{C1}$$

$$\begin{aligned}|\mathcal{D}_2\rangle = {} & SQ/(\sqrt{S^2+P^2+Q^2}\sqrt{S^2+P^2})|w_\mathrm{L}\rangle \\ & + PQ/(\sqrt{S^2+P^2+Q^2}\sqrt{S^2+P^2})|w_\mathrm{R}\rangle \\ & - \sqrt{S^2+P^2}/(\sqrt{S^2+P^2+Q^2})|w_\mathrm{U}\rangle.\end{aligned} \tag{C2}$$

Calculating the $\mathbf{A}_\nu$ from Eq. (B12) yields

$$\mathbf{A}_S = iPQ/[(S^2+P^2)\sqrt{S^2+P^2+Q^2}]\sigma_y, \tag{C3}$$

$$\mathbf{A}_P = -iSQ/[(S^2+P^2)\sqrt{S^2+P^2+Q^2}]\sigma_y. \tag{C4}$$

Since the gauge field is only proportional to the Pauli matrix σ_y, we solve the path-ordered Eq. (B13) and give directly the result as [10]

$$\mathcal{U} = \begin{pmatrix} \cos\gamma & \sin\gamma \\ -\sin\gamma & \cos\gamma \end{pmatrix}, \tag{C5}$$

with

$$\gamma = \int_{z_\mathrm{i}}^{z_\mathrm{f}} [Q(S\,\partial_z P - P\,\partial_z S)]/[(S^2+P^2)\sqrt{S^2+P^2+Q^2}]dz, \tag{C6}$$

and

$$W_\mathcal{C} = 2\cos\gamma. \tag{C7}$$

Three remarks are important at this point. First, in order to check the nontrivial nature of the implemented gauge field, we could test if $|W_\mathcal{C}| < 2$, meaning the system cannot be described as a collection of Abelian subsystems. However, even though a process with $|W_\mathcal{C}| < 2$ is often referred to as non-Abelian [14], this criterion is only necessary but not sufficient for a "truly" non-Abelian gauge field [15]. Nevertheless, it can be regarded as non-Abelian geometric phase since it is a nontrivial collection of interacting Abelian subsystems. Therefore, we use the above criterion to characterize our implemented gauge fields.

Second, in the special case occurring in the experiments, the dark-state designation to the waveguides L and R flip from z_i to z_f, i.e., $|\mathcal{D}_1(z_\mathrm{i})\rangle = -|w_\mathrm{R}\rangle$, $|\mathcal{D}_2(z_\mathrm{i})\rangle = |w_\mathrm{L}\rangle$ and $|\mathcal{D}_1(z_\mathrm{f})\rangle = |w_\mathrm{L}\rangle$, $|\mathcal{D}_2(z_\mathrm{f})\rangle = |w_\mathrm{R}\rangle$. This results in a change in the above criterion to $|W_\mathcal{C}| > 0$. However, this is only due to the flip in designation and could also be remedied by an additional index flip in the definition of $\mathcal{U}_{ij}$ from which we abstained. This has no repercussions on the applicability of the criterion or its statement.

Third, we mention that we measured the intensity at the end facets of the waveguide system and, therefore, we can only retrieve the absolute values $|\mathcal{U}_{ij}|$. However, since we deal only with real couplings S, P, and Q, no relative phases occur meaning the elements of $\mathcal{U}$ are also real, and we can retrieve, at least, $|W_\mathcal{C}|$. An extension would be the inclusion of phase measurements by interference which can be performed in the waveguide system with a few extra waveguides.

APPENDIX D: QUANTUM METRIC

Interpretation of the generalized STIRAP process as a dynamic under the influence of a gauge field is not the only way to look at it. In a completely equivalent way, we interpret the evolution of a state as propagating in a curved (metric) space, i.e., our parameter manifold defined by the couplings $\{x^\nu\} = \{S, P, Q\}$. Traversing the curve $\mathcal{C}$ in this manifold is, thus, governed by a nontrivial metric tensor providing us with a measure of length along $\mathcal{C}$. A sensible definition [18,19] of such a metric tensor is given by the infinitesimal change in the dark subspace projector $P(z) = \sum_i |\mathcal{D}_i(z)\rangle\langle\mathcal{D}_i(z)|$,

$$\|dP\|^2 = \mathrm{Tr}(dP\,dP) = \mathrm{Tr}(\partial_\mu P\,\partial_\nu P)dx^\mu dx^\nu = g_{\mu\nu}dx^\mu dx^\nu, \tag{D1}$$

with the metric tensor being $g_{\mu\nu} = \mathrm{Tr}(\partial_\mu P\,\partial_\nu P)$. This metric tensor is the real part of the *quantum geometric tensor* from the literature [17–20].

Any process initiated by a parameter variation can be assigned a path length or action along curve $\mathcal{C}$ in the parameter manifold which is defined via the metric tensor, i.e.,

$$L = \int_{z_\mathrm{i}}^{z_\mathrm{f}} \sqrt{g_{\mu\nu}\partial_z x^\mu \partial_z x^\nu}dz. \tag{D2}$$

Minimization with the variational principle leads to geodesics that define processes with the least diabatic error for a given total length along z [18]. If we have an actual experimental implementation with certain boundary conditions on curves that can be realized, we might not be able to obtain perfect geodesics. Nevertheless, L is a possible measure for the quality of a certain curve/parameter variation and may be used for optimization, i.e., helps to find the curve with the least diabatic error/path length for given constraints (such as pulse shape, etc.). This idea was used to obtain optimized coupling variations when designing the waveguide system for different gauge fields or Wilson loops with details on the couplings discussed in the next Appendix.

A few comments are in order at this point. The introduced gauge field connection and metric tensor are similar in that both are ultimately linked to the nonvanishing derivative of the dark states. The first by the projection of the derivative on the dark subspace, cf. Eq. (B12), and the latter by the derivative of the dark subspace projector itself, cf. Eq. (D1). However, the metric tensor $\mathbf{g}$ has its own connection or Christoffel symbol and is not linked to the gauge field in the sense of a metric connection in differential geometry. This is rooted in the fact that the gauge field is not completely analogous to the Christoffel symbol since the former connects dark states and the latter tangential vectors along a curve $\mathcal{C}$. Hence, the elements $(\mathbf{A}_\nu)_{ki}$ incorporate the parameter manifold index ν and dark subspace indices k, i. As a result, $(\mathbf{A}_\nu)_{ki}$ cannot be expressed in terms of derivatives of a metric, such as the Christoffel symbols can. Indeed, as a metric connection the gauge field is only associated with the trivial metric δ_{ij} of the dark subspace. For further discussion of the metric tensor and its intricate relation to the gauge field connection see Refs. [19,23].

For completeness, we also give the metric tensor that describes the tripod STIRAP process with the three real

TABLE II. Coupling parameters and results. Pulse parameters for the experimental realization of different pulse shapes/Wilson loop values.

Ω_Q (cm^{-1})	Ω (cm^{-1})	T (cm^{-1})	τ (cm^{-1})	$\lvert W_C^{\text{theo}}\rvert$	$\lvert W_C^{\text{exp}}\rvert$
1.42	1.23	3	1.5	0.88	0.87
1.53	1.46	3	1.5	0.97	1.00
1.60	1.8	3	1.5	1.07	1.13

couplings S, P, and Q. In this case, we find

$$\mathbf{g} = 2\,\text{diag}[1, \cos^2(\phi)]. \tag{D3}$$

Note that the metric is two dimensional since the mixing angles θ and ϕ are the relevant parameters here. This is because the normalization of the dark states makes one parameter degree of S, P, and Q obsolete.

APPENDIX E: DETAILS ON COUPLINGS

For an experimental measurement of the process described by the holonomy $\mathcal{U}$, we have to fix a curve $\mathcal{C}$ in parameter space. However, in the theory outlined above, we saw that in order for the evolution being restricted to the dark subspace, and, thus, $\mathcal{U}$ being valid, we require adiabaticity. This requirement is now opposed by experimental boundary conditions which might limit the number of possible curves and by that the number of unitaries $\mathcal{U}$ that can be realized. For example, a *hard* boundary condition is the physical length of the glass chips in which the photonic waveguides are laser written. We used 15-cm glass chips which, therefore, set the maximal total propagation length and with that the slowest possible process. Using the quantum metric, or the path-length L defined by it, we can find those coupling variations that comply with the experimental constraints and result in the most adiabatic processes ensuring the validity of $\mathcal{U}$.

For the temporal variation of the couplings we choose consecutive Gaussian pulses for S and P (counterintuitive pulse sequence) and hold $Q = \Omega_Q$ constant. The Gaussian pulse sequences are parametrized by

$$S(z) = \Omega\,\exp[-(z - \bar{z} + \tau)^2/T^2], \tag{E1}$$

$$P(z) = \Omega\,\exp[-(z - \bar{z} - \tau)^2/T^2], \tag{E2}$$

where $\bar{z}$ is half the total propagation length, Ω is the amplitude, T is the width parameter, and τ is the separation of the two Gaussian pulses from the center at $\bar{z}$ (given by length of the glass chip). This parametrization allows for simple fabrication of the waveguides and limits the number of parameters in the optimization. In addition, if we restrict the

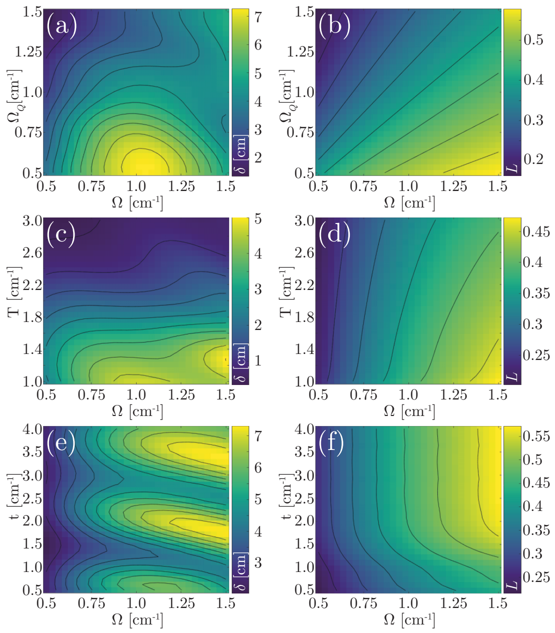

FIG. 5. Comparison of the deviation δ [Eq. (F1)] from an adiabatic evolution [(a), (c), and (e)] with the path-length L, based on Eq. (D2) with the metric defined in Eq. (D3) [(b), (d), and (f)]. The remaining two system parameters are fixed at $t = 1$ and $T = 1$ cm^{-1} for (a) and (b), at $t = 1$ and $\Omega_Q = 1$ cm^{-1} for (c) and (d), and at $T = 1$ and $\Omega_Q = 1$ cm^{-1} for (e) and (f).

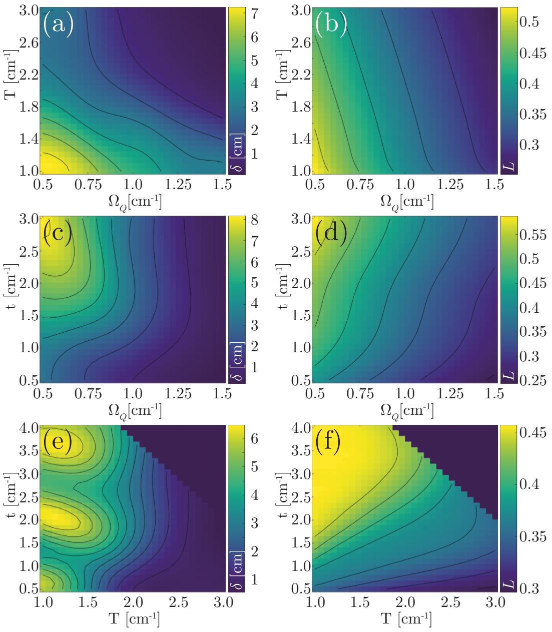

FIG. 6. Comparison of the deviation δ [Eq. (F1)] from an adiabatic evolution [(a), (c), and (e)] with the path-length L, based on Eq. (D2) with the metric defined in Eq. (D3) [(b), (d), and (f)]. The remaining two system parameters are fixed at $t = 1$ and $\Omega = 1$ cm^{-1} for (a) and (b), at $T = 2$ and $\Omega = 1$ cm^{-1} for (c) and (d), and at $\Omega = 1$ and $\Omega_Q = 1$ cm^{-1} for (e) and (f). Note that in order to assure a closed loop in parameter space, the initial and final strengths of the Gaussian pulses are constrained to be equal to or less than 5% of its amplitude Ω_Q. This constraint excludes certain parameters in (e) and (f).

parameters Ω, τ, and T so that we achieve $P(z_\mathrm{i})/S(z_\mathrm{i}) \approx 0$ and $S(z_\mathrm{f})/P(z_\mathrm{f}) \approx 0$ the dark states at these points become simply

$$|\mathcal{D}_1(z_\mathrm{i})\rangle = -|w_\mathrm{R}\rangle, \quad |\mathcal{D}_1(z_\mathrm{i})\rangle = |w_\mathrm{L}\rangle, \tag{E3}$$

$$|\mathcal{D}_2(z_\mathrm{i})\rangle = |w_\mathrm{L}\rangle, \quad |\mathcal{D}_2(z_\mathrm{f})\rangle = |w_\mathrm{R}\rangle. \tag{E4}$$

Additionally, we restrict the coupling amplitudes Ω_Q and Ω to be smaller than 2 cm^{-1} to ensure that the tight-binding approximation is still valid.

The optimization procedure is then the following. For sets of the four parameters Ω_Q, Ω, T, and τ that comply with the above conditions the path-length L is calculated. Each set also resulted in a different theoretical value for the Wilson loop. Therefore, we binned all sets according to their Wilson loops and chose those that minimize L for a given loop. Since for increasing values of the Wilson loop (mind the flip as discussed in Appendix C) the maximal coupling strength also sharply increases to ensure adiabaticity, which is why we could only collect sets up to a Wilson loop of ≈1.2. However, for loops below that, we could collect parameter sets that minimize L and result in different theoretical Wilson loop values.

In the experiments, we implemented three of those sets with the optimized parameters seen in Table II. Also listed are the theoretical and experimental values of the Wilson loops.

APPENDIX F: PATH LENGTH—ERROR COMPARISON

In order to highlight that the path-length optimization is leading to a minimal excitation of the bright state, we performed extended simulations, which are shown in Figs. 5 and 6. We quantify the deviation δ from the adiabatic evolution by the integrated intensity of the central site C along the propagation for the two possible dark-state excitations,

$$\delta = \int_{z_\mathrm{i}}^{z_\mathrm{f}} \left|a_\mathrm{C}^{(1)}\right|^2 dz + \int_{z_\mathrm{i}}^{z_\mathrm{f}} \left|a_\mathrm{C}^{(2)}\right|^2 dz, \tag{F1}$$

where z_i and z_f define the initial and final distances. The quantity $|a_\mathrm{C}^{(1)}|^2$ denotes the intensity in the central site C for the initial excitation of site L, and $|a_\mathrm{C}^{(2)}|^2$ denotes the intensity in the central site C for the initial excitation of site R, corresponding to an excitation of the first or second dark state, respectively. The path-length L, on the other hand, is defined in Eq. (D2) with the metric defined in Eq. (D3). In order to ensure a closed loop in parameter space, the initial and final strengths of the Gaussian pulses are constrained to be equal to or less than 5% of its peak amplitude Ω_Q.

The comparison shows that both methods follow, in general, a similar trend, especially with respect to the position of the minimal deviation/minimal path length. The differences in both schemes may originate from interference of the two bright states, which can lead to less intensity in the central site C.

Moreover, the path-length L is as a function of the system parameters much smoother than the deviation δ, which is beneficial for the calculation of the optimal parameters. Another advantage of the path-length optimization is the reduced computational effort as one only has to solve a one-dimensional integral [Eq. (D2)], whereas for the extraction of the deviation δ, one needs to simulate the entire propagation dynamics for every set of parameters. This might especially be challenging for larger system sizes or networks.

---

[1] M. V. Berry, Proc. R. Soc. London, Ser. A **392**, 45 (1984).

[2] Y. Aharonov and D. Bohm, Phys. Rev. **115**, 485 (1959).

[3] F. Wilczek and A. Zee, Phys. Rev. Lett. **52**, 2111 (1984).

[4] P. Zanardi and M. Rasetti, Phys. Lett. A **264**, 94 (1999).

[5] J. K. Pachos, *Introduction to Topological Quantum Computation* (Cambridge University Press, Cambridge, UK, 2012).

[6] C. Nayak, S. H. Simon, A. Stern, M. Freedman, and S. Das Sarma, Rev. Mod. Phys. **80**, 1083 (2008).

[7] J. Dalibard, F. Gerbier, G. Juzeliūnas, and P. Öhberg, Rev. Mod. Phys. **83**, 1523 (2011).

[8] A. A. Abdumalikov, Jr., J. M. Fink, K. Juliusson, M. Pechal, S. Berger, A. Wallraff, and S. Filipp, Nature (London) **496**, 482 (2013).

[9] L. B. Ma, S. L. Li, V. M. Fomin, M. Hentschel, J. B. Götte, Y. Yin, M. R. Jorgensen, and O. G. Schmidt, Nat. Commun. **7**, 10983 (2016).

[10] R. G. Unanyan, B. W. Shore, and K. Bergmann, Phys. Rev. A **59**, 2910 (1999).

[11] T.-P. Cheng and L.-F. Li, *Gauge Theory of Elementary Particle Physics* (Oxford University Press, Oxford, 1984).

[12] S. Pancharatnam, Proc.-Indian Acad. Sci. Sect. A. **44**, 247 (1956).

[13] K. G. Wilson, Phys. Rev. D **10**, 2445 (1974).

[14] N. Goldman, A. Kubasiak, P. Gaspard, and M. Lewenstein, Phys. Rev. A **79**, 023624 (2009).

[15] N. Goldman, G. Juzeliunas, P. Öhberg, and I. B. Spielman, Rep. Prog. Phys. **77**, 126401 (2014).

[16] K. Bergmann, H. Theuer, and B. W. Shore, Rev. Mod. Phys. **70**, 1003 (1998).

[17] Y.-Q. Ma, S. Chen, H. Fan, and W.-M. Liu, Phys. Rev. B **81**, 245129 (2010).

[18] A. T. Rezakhani, D. F. Abasto, D. A. Lidar, and P. Zanardi, Phys. Rev. A **82**, 012321 (2010).

[19] S. Tanimura, M. Nakahara, and D. Hayashi, J. Math. Phys. **46**, 022101 (2005).

[20] J. P. Provost and G. Vallee, Commun. Math. Phys. **76**, 289 (1980).

[21] S. Longhi, Laser Photon. Rev. **3**, 243 (2009).

[22] A. Szameit and S. Nolte, J. Phys. B: At. Mol. Opt. Phys. **43**, 163001 (2010).

[23] J. Dell, J. L. deLyra, and L. Smolin, Phys. Rev. D **34**, 3012 (1986).

List of all publications

Journal articles

[M1] S. Weimann, M. Kremer, Y. Plotnik, Y. Lumer, S. Nolte, K. G. Makris, M. Segev, M. C. Rechtsman, and A. Szameit *Topologically protected bound states in photonic parity–time-symmetric crystals*, Nature Materials **16**, 433 (2017).

[M2] M. Kremer, R. Sachdeva, A. Benseny, and T. Busch *Interaction-induced effects on Bose-Hubbard parameters*, Phys. Rev. A **96**, 063611 (2017)

[M3] M. Kremer, T. Biesenthal, L. J. Maczewsky, Matthias Heinrich, Ronny Thomale, and Alexander Szameit *Demonstration of a two-dimensional* $\mathcal{PT}$*-symmetric crystal*, Nature Communications **10**, 435 (2019).

[M4] T. Biesenthal, M. Kremer, M. Heinrich, and A. Szameit *Experimental realization of* $\mathcal{PT}$*-symmetric flat bands*, Physical Review Letters **123**, 183601 (2019).

[M5] M. Kremer, L. Teuber, A. Szameit, and S. Scheel *Optimal design strategy for non-Abelian geometric phases using Abelian gauge fields based on quantum metric*, Physical Review Research **1**, 033117 (2019).

[M6] M. Kremer, I. Petrides, E. Meyer, M. Heinrich, O. Zilberberg, and A. Szameit *A square-root topological insulator with non-quantized indices realized with photonic Aharonov-Bohm cages*, Nature Communications **11**, 907 (2020).

[M7] G. Queraltó, M. Kremer, L. J. Maczewsky, M. Heinrich, J. Mompart, V. Ahufinger, and A. Szameit *Topological state engineering via supersymmetric transformations*, Communications Physics **3**, 49 (2020).

[M8] L. J. Maczewsky, B. Höckendorf, M. Kremer, T. Biesenthal, M. Heinrich, A. Alvermann, H. Fehske, and A. Szameit *Fermionic time-reversal symmetry in a photonic topological insulator*, Nature Materials **19**, 855 (2020).

[M9] S. Weidemann, M. Kremer, T. Helbig, T. Hofmann, A. Stegmaier, M. Greiter, R. Thomale, and A. Szameit *Topological funneling of light*, Science **368**, 311 (2020).

[M10] C. Jörg, G. Queraltó, M. Kremer, G. Pelegrí, J. Schulz, A. Szameit, G. von Freymann, J. Mompart, and V. Ahufinger *Artificial gauge field switching using orbital angular momentum modes in optical waveguides*, Light: Science & Applications **9**, 150 (2020).

[M11] L. J. Maczewsky, M. Heinrich, M. Kremer, S. K. Ivanov, M. Ehrhardt, F. Martinez, Y. V. Kartashov, V. V. Konotop, L. Torner, D. Bauer, and A. Szameit *Nonlinearity-induced photonic topological insulator*, Science *accepted.*

Book chapters

1. T. Eichelkraut, S. Weimann, M. Kremer, M. Ornigotti, and A. Szameit *Passive PT-symmetry in laser-written optical waveguide structures*, in: D. Christodoulides, and J. Yang (eds) *Parity-time symmetry and its applications*, Springer Tracts in Modern Physics, **vol 280**, Springer, Singapore (2018).

Bibliography

[1] P. G. Fré, *A conceptual history of space and symmetry: From plato to the superworld* (Springer Nature Switzerland AG, Cham, 2018).

[2] T. L. Heath, *A history of greek mathematics* (Cambridge University Press, Cambridge, 2013).

[3] K. Brading and E. Castellani, eds., *Symmetries in physics* (Cambridge University Press, Cambridge, 2003).

[4] J. F. Cornwell, *Group theory in physics: an introduction* (Academic Press, San Diego, 1997).

[5] A. Einstein, Ann. Phys. **322**, 891 (1905).

[6] H. A. Lorentz, Proc. R. Acad. Amsterdam **6**, 809 (1904).

[7] H. Poincaré, Proc. Acad. Sci **140**, 1504 (1905).

[8] E. Noether, Nachrichten von der Gesellschaft der Wissenschaften zu Göttingen, Math. Klasse , 235 (1918).

[9] E. Bessel-Hagen, Math. Ann. **84**, 258 (1921).

[10] H. Weyl, *Gruppentheorie und quantenmechanik* (S. Hirzel, Leipzig, 1928).

[11] S. Weinberg, *The quantum theory of fields (volume 2: modern applications)* (Cambridge University Press, Cambridge, 1996).

[12] H. Stephani, D. Kramer, M. MacCallum, C. Hoenselaers, and E. Herlt, *Exact solutions of Einstein's field equations* (Cambridge University Press, Cambridge, 2003).

[13] J. K. Asbóth, L. Oroszlány, and A. Pályi, *A short course on topological insulators: band-structure topology and edge states in one and two dimensions* (Springer International Publishing, Cham, 2015).

[14] M. Nakahara, *Geometry, topology and physics* (IOP Publishing, London, 2003).

[15] D. J. Thouless, M. Kohmoto, M. P. Nightingale, and M. den Nijs, Phys. Rev. Lett. **49**, 405 (1982).

[16] F. D. M. Haldane, Phys. Rev. Lett. **61**, 2015 (1988).

[17] K. v. Klitzing, G. Dorda, and M. Pepper, Phys. Rev. Lett. **45**, 494 (1980).

[18] Y. E. Kraus, Y. Lahini, Z. Ringel, M. Verbin, and O. Zilberberg, Phys. Rev. Lett. **109**, 106402 (2012).

[19] M. C. Rechtsman, J. M. Zeuner, Y. Plotnik, Y. Lumer, D. Podolsky, F. Dreisow, S. Nolte, M. Segev, and A. Szameit, Nature **496**, 196 (2013).

[20] T. Ozawa, H. M. Price, A. Amo, N. Goldman, M. Hafezi, L. Lu, M. C. Rechtsman, D. Schuster, J. Simon, O. Zilberberg, and I. Carusotto, Rev. Mod. Phys. **91**, 015006 (2019).

[21] R. Süsstrunk and S. D. Huber, Science **349**, 47 (2015).

[22] A. P. Schnyder, S. Ryu, A. Furusaki, and A. W. W. Ludwig, Phys. Rev. B **78**, 195125 (2008).

[23] S. Weinberg, *The quantum theory of fields (volume 3: supersymmetry)* (Cambridge University Press, Cambridge, 2000).

[24] A. Szameit and S. Nolte, J. Phys. B At. Mol. Opt. Phys. **43**, 163001 (2010).

[25] T. Eichelkraut, R. Heilmann, S. Weimann, S. Stützer, F. Dreisow, D. N. Christodoulides, S. Nolte, and A. Szameit, Nat. Commun. **4**, 2533 (2013).

[26] M. Heinrich, M.-A. Miri, S. Stützer, R. El-Ganainy, S. Nolte, A. Szameit, and D. N. Christodoulides, Nat. Commun. **5**, 3698 (2014).

[27] J. R. Pierce, J. Appl. Phys. **25**, 179 (1954).

[28] E. A. Marcatili, Bell Syst. Tech. J. **48**, 2071 (1969).

[29] A. W. Snyder, J. Opt. Soc. Am. **62**, 1267 (1972).

[30] A. Yariv, IEEE J. Quantum Electron. **9**, 919 (1973).

[31] D. Marcuse, Bell Syst. Tech. J. **52**, 817 (1973).

[32] A. Hardy and W. Streifer, J. Light. Technol. **4**, 90 (1986).

[33] P. S. J. Russell, Appl. Phys. B Photophysics Laser Chem. **39**, 231 (1986).

[34] R. Heilmann, M. Gräfe, S. Nolte, and A. Szameit, Sci. Rep. **4**, 4118 (2014).

[35] A. Yariv, *Optical electronics* (Saunders College Publishing, Philadelphia, 1991).

[36] S. Longhi, Laser Photonics Rev. **3**, 243 (2009).

[37] J. J. Sakurai and J. Napolitano, *Modern quantum mechanics* (Addison-Wesley, Boston, 2011).

[38] R. B. Laughlin, Phys. Rev. Lett. **50**, 1395 (1983).

[39] M. Z. Hasan and C. L. Kane, Rev. Mod. Phys. **82**, 3045 (2010).

[40] M. V. Berry, Proc. R. Soc. London. A. Math. Phys. Sci. **392**, 45 (1984).

[41] J. Zak, Phys. Rev. Lett. **62**, 2747 (1989).

[42] C. L. Kane and E. J. Mele, Phys. Rev. Lett. **95**, 146802 (2005).

[43] L. Fu and C. L. Kane, Phys. Rev. B **74**, 195312 (2006).

[44] K. Esaki, M. Sato, K. Hasebe, and M. Kohmoto, Phys. Rev. B **84**, 205128 (2011).

[45] R. Resta, J. Phys. Condens. Matter **12**, R107 (2000).

[46] F. De Juan, A. Rüegg, and D. H. Lee, Phys. Rev. B **89**, 161117 (2014).

[47] W. P. Su, J. R. Schrieffer, and A. J. Heeger, Phys. Rev. Lett. **42**, 1698 (1979).

[48] C.-K. Chiu, J. C. Teo, A. P. Schnyder, and S. Ryu, Rev. Mod. Phys. **88**, 035005 (2016).

[49] F. Wilczek and A. Zee, Phys. Rev. Lett. **52**, 2111 (1984).

[50] R. Shindou and K.-I. Imura, Nucl. Phys. B **720**, 399 (2005).

[51] J. W. Chan, T. Huser, S. Risbud, and D. M. Krol, Opt. Lett. **26**, 1726 (2001).

[52] S. Vukelic, B. Gao, S. Ryu, and Y. L. Yao, ASME 2008 Int. Manuf. Sci. Eng. Conf. **1**, 227 (2008).

[53] A. F. Holleman, N. Wiberg, and E. Wiberg, *Lehrbuch der anorganischen Chemie* (Walter de Gruyter, Berlin, 2007).

[54] R. R. Gattass and E. Mazur, Nat. Photonics **2**, 219 (2008).

[55] R. Keil, B. Pressl, R. Heilmann, M. Gräfe, G. Weihs, and A. Szameit, Appl. Phys. Lett. **107**, 241104 (2015).

[56] L. J. Maczewsky, S. Weimann, M. Kremer, M. Heinrich, and A. Szameit, Conf. Lasers Electro-Optics , FM1C.6 (2019).

[57] T. D. Lee and C. N. Yang, Phys. Rev. **104**, 254 (1956).

[58] C. S. Wu, E. Ambler, R. W. Hayward, D. D. Hoppes, and R. P. Hudson, Phys. Rev. **105**, 1413 (1957).

[59] C. M. Bender and S. Boettcher, Phys. Rev. Lett. **80**, 5243 (1998).

[60] A. Mostafazadeh, J. Math. Phys. **43**, 205 (2002).

[61] P. D. Mannheim, Philos. Trans. R. Soc. A Math. Phys. Eng. Sci. **371**, 20120060 (2013).

[62] A. Ruschhaupt, F. Delgado, and J. G. Muga, J. Phys. A. Math. Gen. **38**, L171 (2005).

[63] R. El-Ganainy, K. G. Makris, D. N. Christodoulides, and Z. H. Musslimani, Opt. Lett. **32**, 2632 (2007).

[64] K. G. Makris, R. El-Ganainy, D. N. Christodoulides, and Z. H. Musslimani, Phys. Rev. Lett. **100**, 103904 (2008).

[65] A. Guo, G. J. Salamo, D. Duchesne, R. Morandotti, M. Volatier-Ravat, V. Aimez, G. A. Siviloglou, and D. N. Christodoulides, Phys. Rev. Lett. **103**, 093902 (2009).

[66] C. E. Rüter, K. G. Makris, R. El-Ganainy, D. N. Christodoulides, M. Segev, and D. Kip, Nat. Phys. **6**, 192 (2010).

[67] T. Eichelkraut, S. Weimann, S. Stützer, S. Nolte, and A. Szameit, Opt. Lett. **39**, 6831 (2014).

[68] J. M. Zeuner, M. C. Rechtsman, Y. Plotnik, Y. Lumer, S. Nolte, M. S. Rudner, M. Segev, and A. Szameit, Phys. Rev. Lett. **115**, 040402 (2015).

[69] H. Hodaei, M.-A. Miri, M. Heinrich, D. N. Christodoulides, and M. Khajavikhan, Science **346**, 975 (2014).

[70] W. Liu, M. Li, R. S. Guzzon, E. J. Norberg, J. S. Parker, M. Lu, L. A. Coldren, and J. Yao, Nat. Commun. **8**, 15389 (2017).

[71] B. Peng, S. K. Özdemir, F. Lei, F. Monifi, M. Gianfreda, G. L. Long, S. Fan, F. Nori, C. M. Bender, and L. Yang, Nat. Phys. **10**, 394 (2014).

[72] L. Chang, X. Jiang, S. Hua, C. Yang, J. Wen, L. Jiang, G. Li, G. Wang, and M. Xiao, Nat. Photonics **8**, 524 (2014).

[73] B. Zhen, C. W. Hsu, Y. Igarashi, L. Lu, I. Kaminer, A. Pick, S.-L. Chua, J. D. Joannopoulos, and M. Soljačić, Nature **525**, 354 (2015).

[74] A. Regensburger, C. Bersch, M.-A. Miri, G. Onishchukov, D. N. Christodoulides, and U. Peschel, Nature **488**, 167 (2012).

[75] M. Wimmer, M.-A. Miri, D. Christodoulides, and U. Peschel, Sci. Rep. **5**, 17760 (2015).

[76] L. Feng, R. El-Ganainy, and L. Ge, Nat. Photonics **11**, 752 (2017).

[77] R. El-Ganainy, K. G. Makris, M. Khajavikhan, Z. H. Musslimani, S. Rotter, and D. N. Christodoulides, Nat. Phys. **14**, 11 (2018).

[78] H. Hodaei, A. U. Hassan, S. Wittek, H. Garcia-Gracia, R. El-Ganainy, D. N. Christodoulides, and M. Khajavikhan, Nature **548**, 187 (2017).

[79] L. Feng, Z. J. Wong, R.-M. Ma, Y. Wang, and X. Zhang, Science **346**, 972 (2014).

[80] M. Ornigotti and A. Szameit, J. Opt. **16**, 065501 (2014).

[81] M. Lawrence, N. Xu, X. Zhang, L. Cong, J. Han, W. Zhang, and S. Zhang, Phys. Rev. Lett. **113**, 093901 (2014).

[82] M. C. Rechtsman, Y. Plotnik, J. M. Zeuner, D. Song, Z. Chen, A. Szameit, and M. Segev, Phys. Rev. Lett. **111**, 103901 (2013).

[83] Y. Plotnik, M. C. Rechtsman, D. Song, M. Heinrich, J. M. Zeuner, S. Nolte, Y. Lumer, N. Malkova, J. Xu, A. Szameit, Z. Chen, and M. Segev, Nat. Mater. **13**, 57 (2014).

[84] A. Szameit, M. C. Rechtsman, O. Bahat-Treidel, and M. Segev, Phys. Rev. A **84**, 021806 (2011).

[85] M. Fujita, K. Wakabayashi, K. Nakada, and K. Kusakabe, J. Phys. Soc. Japan **65**, 1920 (1996).

[86] M. Kohmoto and Y. Hasegawa, Phys. Rev. B **76**, 205402 (2007).

[87] A. L. Muniz, M. Wimmer, A. Bisianov, U. Peschel, R. Morandotti, P. S. Jung, and D. N. Christodoulides, Phys. Rev. Lett. **123**, 253903 (2019).

[88] A. Cerjan, S. Huang, M. Wang, K. P. Chen, Y. Chong, and M. C. Rechtsman, Nat. Photonics **13**, 623 (2019).

[89] E. Witten, Nucl. Physics, Sect. B **188**, 513 (1981).

[90] F. Cooper, A. Khare, and U. Sukhatme, *Supersymmetry in quantum mechanics* (World Scientific Publishing Co., Singapore, 2001).

[91] B. Mielnik, J. Math. Phys. **25**, 3387 (1984).

[92] M. M. Nieto, Phys. Lett. B **145**, 208 (1984).

[93] S. M. Chumakov and K. B. Wolf, Phys. Lett. A **193**, 51 (1994).

[94] M.-A. Miri, M. Heinrich, R. El-Ganainy, and D. N. Christodoulides, Phys. Rev. Lett. **110**, 233902 (2013).

[95] G. Queraltó, V. Ahufinger, and J. Mompart, Opt. Express **25**, 27396 (2017).

[96] A. Macho, R. Llorente, and C. García-Meca, Phys. Rev. Appl. **9**, 014024 (2018).

[97] G. Queraltó, V. Ahufinger, and J. Mompart, Opt. Express **26**, 33797 (2018).

[98] W. Walasik, B. Midya, L. Feng, and N. M. Litchinitser, Opt. Lett. **43**, 3758 (2018).

[99] A. Contreras-Astorga and V. Jakubský, Phys. Rev. A **99**, 053812 (2019).

[100] M. Heinrich, M.-A. Miri, S. Stützer, S. Nolte, D. N. Christodoulides, and A. Szameit, Opt. Lett. **39**, 6130 (2014).

[101] S. Longhi, Opt. Lett. **40**, 463 (2015).

[102] C. García-Meca, A. M. Ortiz, and R. L. Sáez, Nat. Commun. **11**, 813 (2020).

[103] R. El-Ganainy, L. Ge, M. Khajavikhan, and D. N. Christodoulides, Phys. Rev. A **92**, 033818 (2015).

[104] M. P. Hokmabadi, N. S. Nye, R. El-Ganainy, D. N. Christodoulides, and M. Khajavikhan, Science **363**, 623 (2019).

[105] B. Midya, H. Zhao, X. Qiao, P. Miao, W. Walasik, Z. Zhang, N. M. Litchinitser, and L. Feng, Photonics Res. **7**, 363 (2019).

[106] M.-A. Miri, M. Heinrich, and D. N. Christodoulides, Phys. Rev. A **87**, 043819 (2013).

[107] B. Midya, Phys. Rev. A **89**, 032116 (2014).

[108] S. Yu, X. Piao, J. Hong, and N. Park, Nat. Commun. **6**, 8269 (2015).

[109] B. Midya, W. Walasik, N. M. Litchinitser, and L. Feng, Opt. Lett. **43**, 4927 (2018).

[110] L. Hogben, *Handbook of linear algebra* (Chapman and Hall/CRC, London, 2006).

[111] P. A. M. Dirac, Proc. R. Soc. London A **117**, 610 (1928).

[112] L. Alvarez-Gaume, J. Phys. A. Math. Gen. **16**, 4177 (1983).

[113] F. Cooper, A. Khare, and U. Sukhatme, Phys. Rep. **251**, 267 (1995).

[114] C. L. Kane and T. C. Lubensky, Nat. Phys. **10**, 39 (2014).

[115] J. Arkinstall, M. H. Teimourpour, L. Feng, R. El-Ganainy, and H. Schomerus, Phys. Rev. B **95**, 165109 (2017).

[116] Z. Zhang, M. H. Teimourpour, J. Arkinstall, M. Pan, P. Miao, H. Schomerus, R. El-Ganainy, and L. Feng, Laser Photon. Rev. **13**, 1800202 (2019).

[117] H. L. Stormer, D. C. Tsui, and A. C. Gossard, Rev. Mod. Phys. **71**, S298 (1999).

[118] A. M. Marques and R. G. Dias, Phys. Rev. B **100**, 41104 (2019).

[119] D. R. Hofstadter, Phys. Rev. B **14**, 2239 (1976).

[120] S. Aubry and G. André, Ann. Isr. Phys. Soc **3**, 18 (1980).

[121] F. Mei, S.-L. Zhu, Z.-M. Zhang, C. H. Oh, and N. Goldman, Phys. Rev. A **85**, 13638 (2012).

[122] L.-J. Lang, X. Cai, and S. Chen, Phys. Rev. Lett. **108**, 220401 (2012).

[123] V. M. Martinez Alvarez and M. D. Coutinho-Filho, Phys. Rev. A **99**, 013833 (2019).

[124] Y. X. Xiao, G. Ma, Z. Q. Zhang, and C. T. Chan, Phys. Rev. Lett. **118**, 166803 (2017).

[125] Y. Aharonov and D. Bohm, Phys. Rev. **115**, 485 (1959).

[126] J. Vidal, R. Mosseri, and B. Douçot, Phys. Rev. Lett. **81**, 5888 (1998).

[127] R. Keil, C. Poli, M. Heinrich, J. Arkinstall, G. Weihs, H. Schomerus, and A. Szameit, Phys. Rev. Lett. **116**, 213901 (2016).

[128] S. Longhi, Opt. Lett. **39**, 5892 (2014).

[129] S. Mukherjee, M. Di Liberto, P. Öhberg, R. R. Thomson, and N. Goldman, Phys. Rev. Lett. **121**, 075502 (2018).

[130] G. Pelegrí, A. M. Marques, R. G. Dias, A. J. Daley, V. Ahufinger, and J. Mompart, Phys. Rev. A **99**, 023612 (2019).

[131] G. Pelegrí, A. M. Marques, R. G. Dias, A. J. Daley, J. Mompart, and V. Ahufinger, Phys. Rev. A **99**, 023613 (2019).

[132] M. Ammon and J. Erdmenger, *Gauge/Gravity duality* (Cambridge University Press, Cambridge, 2015).

[133] R. Giles, Phys. Rev. D **24**, 2160 (1981).

[134] J. H. Van Vleck, Phys. Rev. **33**, 467 (1929).

[135] J. W. Zwanziger, M. Koenig, and A. Pines, Phys. Rev. A **42**, 3107 (1990).

[136] S. Tanimura, M. Nakahara, and D. Hayashi, J. Math. Phys. **46**, 022101 (2005).

[137] Y.-Q. Ma, S. Chen, H. Fan, and W.-M. Liu, Phys. Rev. B **81**, 245129 (2010).

[138] A. T. Rezakhani, D. F. Abasto, D. A. Lidar, and P. Zanardi, Phys. Rev. A **82**, 012321 (2010).

[139] J. P. Provost and G. Vallee, Commun. Math. Phys. **76**, 289 (1980).

[140] R. G. Unanyan, B. W. Shore, and K. Bergmann, Phys. Rev. A **59**, 2910 (1999).

[141] K. Bergmann, H. Theuer, and B. W. Shore, Rev. Mod. Phys. **70**, 1003 (1998).

[142] P. Zanardi and M. Rasetti, Phys. Lett. A **264**, 94 (1999).

[143] J. K. Pachos, *Introduction to topological quantum computation* (Cambridge University Press, Cambridge, 2012).

[144] J. Pinske, L. Teuber, and S. Scheel, Phys. Rev. A **101**, 062314 (2020).

[145] J. Alicea, Y. Oreg, G. Refael, F. von Oppen, and M. P. A. Fisher, Nat. Phys. **7**, 412 (2011).

[146] A. A. Abdumalikov, J. M. Fink, K. Juliusson, M. Pechal, S. Berger, A. Wallraff, and S. Filipp, Nature **496**, 482 (2013).

[147] L. Huang, Z. Meng, P. Wang, P. Peng, S.-L. Zhang, L. Chen, D. Li, Q. Zhou, and J. Zhang, Nat. Phys. **12**, 540 (2016).

[148] Z. Wu, L. Zhang, W. Sun, X.-T. Xu, B.-Z. Wang, S.-C. Ji, Y. Deng, S. Chen, X.-J. Liu, and J.-W. Pan, Science **354**, 83 (2016).

[149] L. B. Ma, S. L. Li, V. M. Fomin, M. Hentschel, J. B. Götte, Y. Yin, M. R. Jorgensen, and O. G. Schmidt, Nat. Commun. **7**, 10983 (2016).

[150] S. Sugawa, F. Salces-Carcoba, A. R. Perry, Y. Yue, and I. B. Spielman, Science **360**, 1429 (2018).

[151] Y. Yang, C. Peng, D. Zhu, H. Buljan, J. D. Joannopoulos, B. Zhen, and M. Soljačić, Science **365**, 1021 (2019).

[152] X. Chen, A. Ruschhaupt, S. Schmidt, A. Del Campo, D. Guéry-Odelin, and J. G. Muga, Phys. Rev. Lett. **104**, 063002 (2010).

Conference contributions

Talks

- **Non-Abelian gauge fields in integrated photonic waveguide structures**
  Deutsche Physikalische Gesellschaft – spring meeting
  Erlangen, Germany 03/2018
- **Realization of a non-quantized topological insulator using photonic Aharonov-Bohm cages**
  Deutsche Physikalische Gesellschaft – spring meeting
  Rostock, Germany 03/2019
- **Realization of a non-quantized square-root topological insulator based on photonic Aharonov-Bohm cages**
  Non-Abelian geometric phases in photonics and their optimal design strategy based on quantum metric
  Conference on Lasers and Electro-Optics (CLEO)
  San Jose, USA 05/2019
- **Optimal design strategy for non-Abelian geometric phases in photonics based on quantum metric**
  From topology to photonics and beyond
  Greifswald, Germany 06/2019
- **Optimal design strategy of non-Abelian geometric phases based on quantum metric**
  Conference on Lasers and Electro-Optics Europe (CLEO EU)
  Munich, Germany 06/2019

Posters

- **Optical implementation of the Hofstadter butterfly**
  Discrete, nonlinear and disordered optics
  Dresden, Germany 05/2017
- **Demonstartion of a non-quantized square-root topological insulator using photonic Aharonov-Bohm cages**
  Quantum simulations with atoms and light
  Aarhus, Denmark 08/2018
- **Experimental realization of two-dimensional PT-symmetric graphene: bulk properties and edge states**
  Experimental demonstration of a non-quantized square root topological insulator using photonic Aharonov-Bohm cages
  Conference on Lasers and Electro-Optics Europe (CLEO EU)
  Munich, Germany 06/2019

Acknowledgements

First of all I want to thank Prof. Dr. Alexander Szameit, who provided the framework to pursuit my academic goals and ideas. This thesis would not exist if it were not for him. Furthermore, he shared his insights and knowledge in numerous fruitful discussions and always created a welcoming working atmosphere, which helped over every failure.

I also want to express my gratefulness to the whole group of Prof. Szameit. Especially the time I spent with Lukas Maczewsky, Steffen Weimann, and Sebastian Weidemann was not only academically enriching but also joyful and inspiring. I also want to thank Calum Maitland and Marco Ornigotti who supported me along my journey, by sharing their knowledge and perspectives with me.

I also want to express my thanks to Martin Wimmer, who inspired me in my academic work ever since he supervised me during my master thesis. Despite being separated by a few hundred kilometres, the fruitful discussions with my former flatmate and close friend Sebastian Ulbricht never stopped, for which I am really thankful.

Finally I want to express my thankfulness to my family and my partner, who always supported me during my intensive and time consuming studies.